


8-1-1979

Atmospheric Forcing of the Bight of Abaco

Peter M. Smith
Nova Southeastern University

Follow this and additional works at: https://nsuworks.nova.edu/occ_stuetd

 Part of the [Marine Biology Commons](#), and the [Oceanography and Atmospheric Sciences and Meteorology Commons](#)

Share Feedback About This Item

NSUWorks Citation

Peter M. Smith. 1979. *Atmospheric Forcing of the Bight of Abaco*. Doctoral dissertation. Nova Southeastern University. Retrieved from NSUWorks, . (72)
https://nsuworks.nova.edu/occ_stuetd/72.

This Dissertation is brought to you by the HCNSO Student Work at NSUWorks. It has been accepted for inclusion in HCNSO Student Theses and Dissertations by an authorized administrator of NSUWorks. For more information, please contact nsuworks@nova.edu.

NOVA UNIVERSITY

ATMOSPHERIC FORCING
OF THE
BIGHT OF ABACO

by

Peter M. Smith

A DISSERTATION

Submitted to the Faculty of Nova University in
partial fulfillment of the requirements for the
degree of Doctor of Philosophy

Fort Lauderdale, Florida

August 1979

NOVA UNIVERSITY

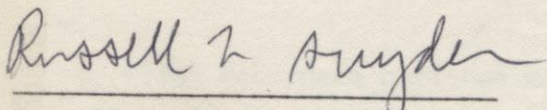
A dissertation submitted in partial fulfillment of
the requirements for the degree of
Doctor of Philosophy

Atmospheric Forcing of the Bight of
Abaco

by

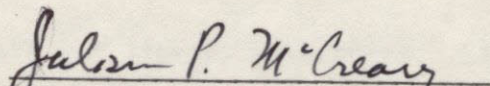
Peter M. Smith

Approved:

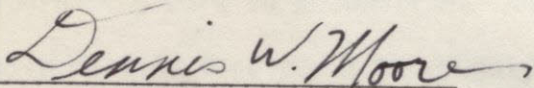


Russell L. Snyder PhD

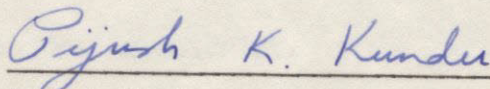
Committee Chairman



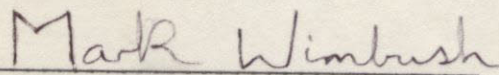
Julian P. McCreary PhD



Dennis W. Moore PhD



Pijush Kundu PhD



Mark Wimbush PhD

ACKNOWLEDGMENTS

This thesis is dedicated to Sandra, Becky, and Holly who supported and encouraged Daddy through several false starts, and passed up a few vacations so that he could complete this work.

The influence of Dr. Russell M. Snyder is in evidence throughout this thesis. Much of the analysis is due to Russ, especially the extension of Professor Platzman's formalism to include the Green's function. Russ was extremely unselfish with his time, often dropping his own work to discuss a problem area. Professor Platzman, through several phone conversations, pointed me toward the proper references and otherwise gave his encouragement.

Ellen McCormack obtained many hard-to-get library references. Linda Smith put up with an endless stream of questions when she had her own programming work to accomplish. And Marilyn Baker prodded me for corrections while putting together a thoroughly professional manuscript.

I thank you all.

TABLE OF CONTENTS

	<u>PAGE</u>
Acknowledgments	
List of Illustrations	-i-
List of Tables	-iii-

SECTION

1	<u>INTRODUCTION</u>	1-1
2	<u>THE EQUATIONS</u>	2-1
3	<u>THE GREEN'S FORMALISM</u>	3-1
	The Frictionless Case	3-1
	A Green's Theorem for \mathcal{L}	3-4
	The Frictional, Non-self-adjoint Case	3-6
4	<u>NORMAL MODES FOR THE BIGHT OF ABACO</u>	4-1
	Numerical Method	4-1
	Inverse Iteration (for the Frictionless Case)	4-1
	Discretization	4-2
	The Frictional Case	4-5
	The Normal Modes	4-9
	Resonant Q's	4-10
	The Case of Zero Frequency	4-15
	Semi-Enclosed, Constant Depth, Non-Rotating Basin with Friction	4-15
	Semi-Enclosed, Constant Depth, Rotating Basin with Friction	4-17
	The Circular Basin	4-18
	The Bight of Abaco Model	4-23
	Additional Zero Frequency Modes	4-25

<u>SECTION</u>	<u>PAGE</u>
5 <u>THE IMPULSE RESPONSE FUNCTION AND THE TIME STEPPING APPROACH</u> .	5-1
6 <u>PREDICTED RESPONSES VS. MEASURED RESPONSES</u>	6-1
Wind Forcing	6-1
Predicted Response	6-1
7 <u>COMPARISON OF METHODS</u>	7-1
8 <u>DISCUSSION AND CONCLUSIONS</u>	8-1
APPENDIX A STATIONARITY OF THE RAYLEIGH RATIO FOR NON-SELF-ADJOINT OPERATORS	A-1
APPENDIX B EIGENVALUES OF THE ADJOINT OPERATOR	B-1
APPENDIX C CIRCULAR BASIN OF CONSTANT DEPTH WITH FRICTION	C-1
References	

LIST OF ILLUSTRATIONS

<u>FIGURE NO.</u>		<u>PAGE</u>
1-1	Map of the Bight of Abaco showing instrument locations.	1-2
4-1	Discretized operator \mathcal{L} for a typical basin.	4-3
4-2	Discretized lattice for the Bight.	4-6
4-3	Depth contours for the Bight.	4-8
4-4	λ contours for the Bight.	4-8
4-5	Progression of elevation nodes for four modes.	4-11
4-6	Progression of eigenvalues.	4-12
4-7	Power spectrum for three lowest modes.	4-14
4-8	R' vs. ω_1 for the non-rotating, frictional Helmholtz mode — rectangular basin.	4-19
4-9	R' vs. ω_1 for the rotating, frictional Helmholtz mode — rectangular basin.	4-21
4-10	R' vs. ω_1 for the rotating, frictional Helmholtz mode — open circular basin.	4-22
4-11	ϵ vs. ω for the Bight of Abaco.	4-24
4-12	An expanded version of Figure 4-11.	4-24

LIST OF ILLUSTRATIONS (continued)

<u>FIGURE NO.</u>		<u>PAGE</u>
4-13	Plot of velocities for a quasi-geostrophic mode.	4-26
4-14	Elevation contours for a quasi-geostrophic mode.	4-27
4-15	ω_1 vs. ϵ for zero frequency modes at small ϵ .	4-28
4-16 to 4-27	Elevation eigenmodes and adjoint eigenmodes for $0 \leq n \leq 11$.	4-30 to 4-41
5-1	Surface contours of response to an elevation step.	5-6
5-2	Elevation sampling points.	5-7
5-3	Plot of elevation response to elevation step at 4 locations.	5-8
5-4	Plot of elevation response to west wind step at 4 locations.	5-9
5-5	Plot of elevation response to south wind step at 4 locations.	5-10
5-6	Surface contours of response to a step in the west wind.	5-11
5-7	Surface contours of response to a step in the south wind.	5-12
5-8	Velocity field response to a step in the west wind.	5-13
5-9	Velocity field response to a step in the south wind.	5-14
5-10	Elevation response to an impulse in elevation at the opening.	5-16

LIST OF ILLUSTRATIONS (continued)

<u>FIGURE NO.</u>		<u>PAGE</u>
5-11	Elevation response to an impulse in the west wind.	5-17
5-12	Elevation response to an impulse in the south wind.	5-18
6-1	Power spectrum of wind speed at station 3.	6-2
6-2	Phase and coherence of wind speed between the three weather stations.	6-3
6-3 to 6-12	Measured and predicted elevations at 10 stations.	6-6 to 6-15
6-13 to 6-22	Measured elevation minus predicted elevation due to the opening, predicted elevation due to wind, and best fit response to the wind.	6-17 to 6-27
7-1, 7-3, 7-5	Admittance functions at 10 stations predicted on the basis of the time stepping method.	7-3 , 7-5 7-7 , 7-9 7-11, 7-13
7-2, 7-4, 7-6	Admittance functions at 10 stations predicted on the basis of the Green's theorem.	7-4 , 7-6 7-8 , 7-10 7-12, 7-14

LIST OF TABLES

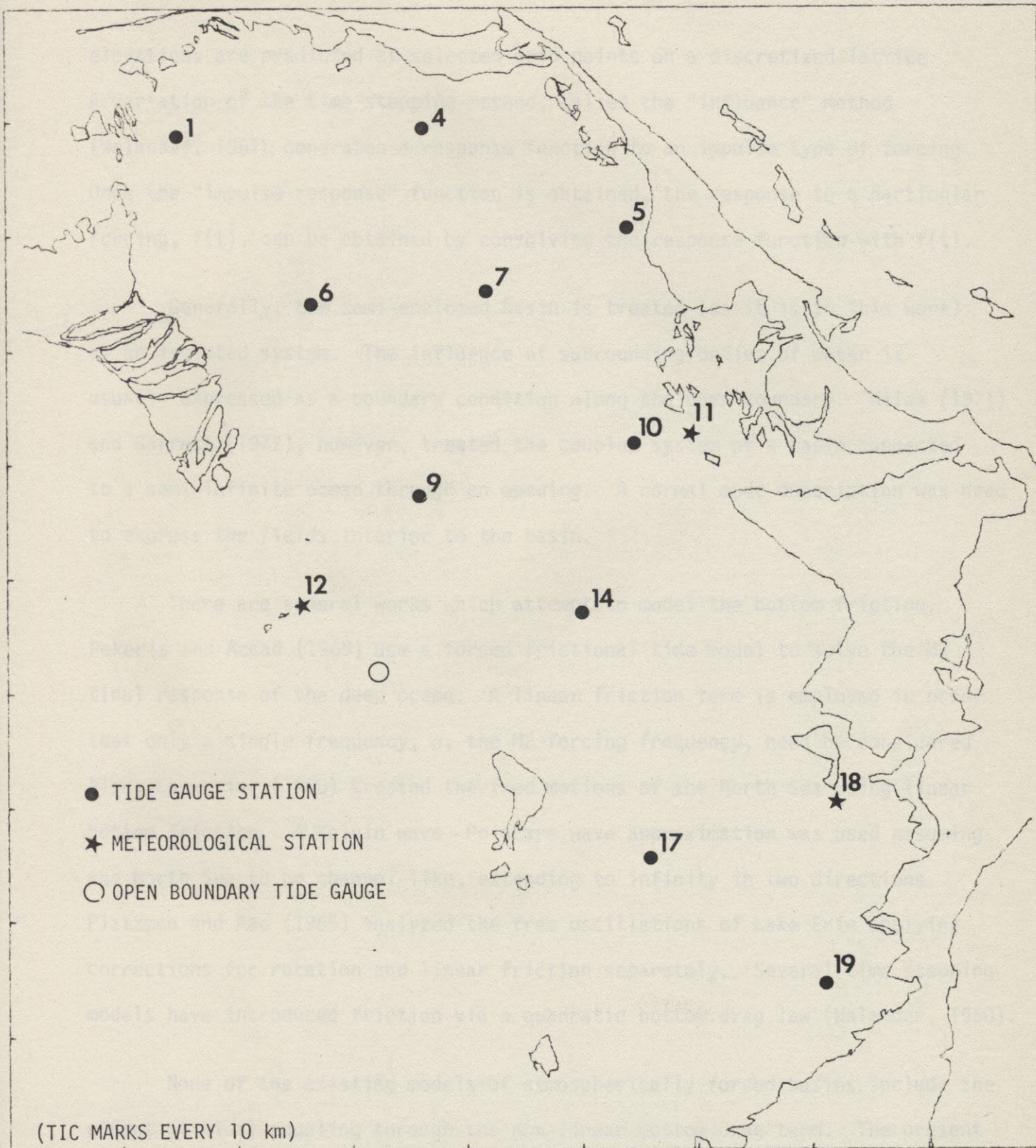
I	Eigenvalues for each of 12 eigenmodes.	4-13
II	Resonant Q's for each of 10 eigenmodes.	4-16
III	Least squares fit parameters for the predicted response due to wind.	6-16

SECTION 1
INTRODUCTION

The response of a large, shallow, semi-enclosed basin to direct wind forcing and boundary forcing through an opening is the subject of this study. The basin treated is the Bight of Abaco, a body of water bounded by Grand Bahama Island and the Abaco Islands, and situated on Little Bahama Bank in the Bahama Islands. The Bight is approximately 90 km long by 50 km wide, with depths ranging from 2 to 8 meters (see Figures 1-1 and 3-3). The entrance to the Bight extends for approximately 60 km and opens onto the 600 meter deep Northwest Providence Channel. The large dimensions of the Bight, together with the relatively shallow depths, suggest that both rotation and friction will play important roles in determining the dynamics of the basin.

Atmospheric forcing of the basin is considered to be primarily due to the surface wind stress in the interior and to the elevation boundary at the opening. The wind stress is deduced by averaging wind speed records from three locations within the Bight, and the boundary elevations are inferred from a single pressure record taken in the vicinity of the opening. The boundary forcing, $\zeta_0(t)$, includes the effects of both waves incident from the ocean and waves reflected from the interior of the Bight.

The traditional approach to a problem of this nature is the time stepping solution of the shallow water wave equations (Hansen, 1956; Leendertse, 1967; Platzman, 1958). Generally, the forcing is prescribed as a time series and the



INSTRUMENT LOCATIONS
 FIGURE 1-1

elevations are predicted at selected grid points on a discretized lattice. A variation of the time stepping method, called the "influence" method (Welander, 1961), generates a response function to an impulse type of forcing. Once the "impulse response" function is obtained, the response to a particular forcing, $f(t)$, can be obtained by convolving the response function with $f(t)$.

Generally, the semi-enclosed basin is treated (as it is in this work) as an isolated system. The influence of surrounding bodies of water is usually expressed as a boundary condition along the open boundary. Miles (1971) and Garrett (1977), however, treated the coupled system of a basin connected to a semi-infinite ocean through an opening. A normal mode description was used to express the fields interior to the basin.

There are several works which attempt to model the bottom friction. Pekeris and Accad (1969) use a forced frictional tide model to solve the M2 tidal response of the deep ocean. A linear friction term is employed in order that only a single frequency, σ , the M2 forcing frequency, need be considered. Also, Lauwerier (1960) treated the free motions of the North Sea using linear bottom friction. A Kelvin wave - Poincare wave approximation was used assuming the North Sea to be channel-like, extending to infinity in two directions. Platzman and Rao (1965) analyzed the free oscillations of Lake Erie applying corrections for rotation and linear friction separately. Several time stepping models have introduced friction via a quadratic bottom drag law (Welander, 1960).

None of the existing models of atmospherically forced basins include the effect of tidal coupling through the non-linear bottom drag term. The present model attempts to include this coupling through the coefficient in the linearized

bottom drag term. This drag coefficient is composed of a space independent term and a term which represents the sum of the r.m.s. tidal velocities. The latter term is necessarily space dependent and is a product of the tidal model developed by Snyder, *et al.* (1979).

Two methods of solution are used here: a linear time stepping method and a Green's function/normal mode approach. Forcing is assumed to be homogeneous, that is $\zeta_0(\vec{x},t) = \zeta_0(t)$; $\tau_x(\vec{x},t) = \tau_x(t)$; and $\tau_y(\vec{x},t) = \tau_y(t)$, where ζ_0 represents the elevation at the opening and τ_x and τ_y are the two components of the surface wind stress.

The time stepping method used is the "influence" method. A response function is obtained for each of the three forcing functions. The response functions are then convoluted with the measured forcings, $\tau_x(t)$, $\tau_y(t)$, and $\zeta_0(t)$, to produce the predicted response. The predicted responses due to wind alone are then compared with the measured elevations less the influence of the opening by performing a least squares fit. The resulting best-fit coefficients provide a measure of the surface drag coefficients at the respective station locations.

A Green's function formalism is developed which allows the inclusion of friction in the normal mode description. The Green's function is synthesized from the normal modes of the Bight. Normal modes to $N=12$ are calculated using the inverse iteration method. The admittance functions for impulse type forcings are derived using a Green's theorem, and the results are compared with the transform of the impulse response functions obtained by time stepping. Since

time stepped solutions aren't subject to truncation errors, this comparison provides a measure of the truncation errors which can be expected from a normal mode expansion technique.

The text is organized as follows. Section 2 describes the partitioning of the tidal and meteorological variables and the derivation of the equations governing the atmospheric response. Section 3 contains the Green's function formalism for both the friction-free and frictional cases and the derivation of the Green's theorem. Section 4 describes the numerical solution for the normal modes and the special problem of interpreting and obtaining the zero frequency modes. Section 5 describes the three time stepped response functions, K_{ζ_0} , K_{τ_x} , and K_{τ_y} . Section 6 presents the predicted response and the comparison with observed data. Section 7 presents a comparison between the admittance function as obtained from the Green's theorem and as obtained by transforming the response function. Section 8 presents a discussion and some conclusions.

SECTION 2

THE EQUATIONS

This study is a continuation of work begun by Snyder, *et al.* (1979) to investigate the self-interaction and cross-interaction of tides and wind set-up in the Bight of Abaco. The shallow water wave equations are used to model the motions. Friction is introduced via a non-linear bottom drag. The basin is driven through a southwest opening (see Figure 1-1) by motions in the Northwest Providence Channel, and driven directly by the wind blowing over the surface of the Bight. The governing equations are taken to be:

$$\begin{aligned} \frac{\partial \vec{U}}{\partial t} + \vec{U} \cdot \nabla \vec{U} + f \hat{k} \times \vec{U} + g \nabla \zeta \\ = - \frac{\nabla p}{\rho} + \frac{1}{h + \zeta} \frac{\tau}{\rho} - \frac{1}{h + \zeta} R(|\vec{U}|) \vec{U} \end{aligned} \quad (2-1)$$

$$\frac{\partial \zeta}{\partial t} + \nabla \cdot (h + \zeta) \vec{U} = 0 \quad (2-2)$$

\vec{U} is the vertically averaged velocity, ζ is the free surface elevation above the mean, h is the depth, p is the atmospheric pressure, τ is the surface wind stress, and $R(|\vec{U}|)$ is a speed dependent friction coefficient. We assume that $h \gg \zeta$, that ∇p effects are small compared to the surface wind stress, and that $\vec{U} \cdot \nabla \vec{U}$ is negligible.

The elevation and velocity are partitioned:

$$\zeta = \zeta_H + \zeta_M + \zeta_R \quad (2-3)$$

and
$$\vec{U} = \vec{U}_H + \vec{U}_M + \vec{U}_R, \quad (2-4)$$

where H refers to "tidal" part, M refers to the "meteorological" part, and R refers to a residual. Equations for ζ_H and \vec{U}_H are obtained by applying the filtering operator,

$$\lim_{T \rightarrow \infty} \sum_n \frac{1}{T} \int_{-T}^T dt' e^{i\omega_n(t-t')},$$

where the ω_n 's are the principal tidal constituents plus overtimes. After Snyder, *et al.* (1979), the velocities and elevations are represented:

$$\vec{U}_H = \frac{1}{2} \sum_n \vec{U}_H H_n$$

$$\zeta_H = \frac{1}{2} \sum_n \zeta_H H_n$$

where

$$H_n = e^{i(\omega_n t + \phi_n)}.$$

Let $\langle\langle \rangle\rangle$ define an ensemble average over an ensemble of realizations of the elevation and velocity fields where we allow the meteorological and tidal forcing to be the same for all realizations, but allow the phases of the tidal forcing to be displaced randomly from one realization to the next. Then,

$$\zeta_M = \langle\langle \zeta \rangle\rangle \quad \text{and} \quad \vec{U}_M = \langle\langle \vec{U} \rangle\rangle$$

$$\langle\langle \zeta_H \rangle\rangle = \langle\langle \zeta_R \rangle\rangle = 0$$

$$\langle\langle \vec{U}_H \rangle\rangle = \langle\langle \vec{U}_R \rangle\rangle = 0.$$

The residual field becomes the difference between a particular realization and the ensemble average.

Applying the $\langle\langle \rangle\rangle$ operator to Eq. (2-1) in order to obtain the equations governing the setup motion, it is necessary to evaluate

$$\langle\langle R(|\vec{U}|)\vec{U} \rangle\rangle = \langle\langle (R_0 + R_1|\vec{U}|)\vec{U} \rangle\rangle .$$

Now,

$$|\vec{U}| = (\vec{U} \cdot \vec{U})^{1/2} = (\vec{U}_H \cdot \vec{U}_H + \vec{U}_M \cdot \vec{U}_M + \vec{U}_R \cdot \vec{U}_R + 2\vec{U}_M \cdot \vec{U}_R + 2\vec{U}_H \cdot \vec{U}_R + 2\vec{U}_M \cdot \vec{U}_R)^{1/2} . \quad (2-5)$$

Assume: $|\vec{U}_H| \gg |\vec{U}_M|$

and $|\vec{U}_H| \gg |\vec{U}_R|$,

giving $|\vec{U}| \cong (\vec{U}_H \cdot \vec{U}_H)^{1/2}$

$$\cong \lambda \left(1 + \frac{1}{8\lambda^2} \sum_{\substack{p,q \\ p \neq -q}} p^U_H q^U_H p^H_p H_q \right) \quad (2-6)$$

where $\lambda \equiv (\vec{U}_H \cdot \vec{U}_H)^{1/2} = \frac{1}{2} \sum_n n^U_H -n^U_H . \quad (2-7)$

(Snyder, *et al.*, 1979)

Thus,

$$\begin{aligned} \langle\langle (R_0 + R_1|\vec{U}|)\vec{U} \rangle\rangle &= \langle\langle (R_0 + R_1|\vec{U}|) (\vec{U}_H + \vec{U}_M + \vec{U}_R) \rangle\rangle \\ &\cong (R_0 + R_1\lambda)\vec{U}_M \\ &\quad + \frac{1}{8\lambda} \sum_{\substack{p,q,r \\ p \neq -q}} \epsilon_{pqr} p^{\vec{U}}_H q^{\vec{U}}_H r^{\vec{U}}_H p^H_p H_q H_r , \end{aligned} \quad (2-8)$$

where $\epsilon_{pqr} = \begin{cases} 1 & \text{if } \omega_p + \omega_q + \omega_r = 0 \\ 0 & \text{otherwise} \end{cases} .$

Finally, applying $\langle\langle \ \ \rangle\rangle$ to Eq.'s (2-1) and (2-2) gives

$$\frac{\partial \vec{U}_M}{\partial t} + f \hat{k} \times \vec{U}_M + g \nabla \zeta_M + \frac{(R_0 + R_1 \lambda)}{h} \vec{U}_M = \frac{\vec{\tau}}{\rho h} \quad (2-9)$$

$$\frac{\partial \zeta_M}{\partial t} + \nabla \cdot h \vec{U}_M = 0 \quad (2-10)$$

The subscript, M, will henceforth be dropped.

SECTION 3

THE GREEN'S FORMALISM

A Green's operator and a Green's theorem are derived for the case of a frictional basin on a rotating constant f plane. The formalism developed by Platzman (1972) for the solution of the primitive tidal equations is merged with the theory of non-self-adjoint operators and adjoint eigenfunctions as explained by Morse and Feshbach (1953) to provide an expression for the forced response in terms of the eigenmodes and adjoint eigenmodes of the basin.

THE FRICTIONLESS CASE

Following the convention established by Platzman (1972), we define the differential operator, \mathcal{L} , by rewriting the friction-free versions of Eq.'s (2-9) and (2-10) as,

$$\frac{\partial \psi}{\partial t} - i\mathcal{L}\psi = \chi \quad (3-1)$$

where

$$\psi = \begin{pmatrix} \vec{u} \\ \zeta \end{pmatrix}, \quad \chi = \begin{pmatrix} \vec{\tau}/\rho h \\ 0 \end{pmatrix},$$

and

$$\mathcal{L} = i \begin{pmatrix} f\hat{k} \times & g\nabla \\ \nabla \cdot (h & 0 \end{pmatrix}. \quad (3-2)$$

If $a = \begin{pmatrix} \vec{u}_a \\ \zeta_a \end{pmatrix}$ and $b = \begin{pmatrix} \vec{u}_b \\ \zeta_b \end{pmatrix}$, then the dot product between a and b , defined on the vector space spanned by the eigenvectors of \mathcal{L} , is given by

$$\langle a, b \rangle = \int_S dS (g \zeta_a^* \zeta_b + h \vec{u}_a^* \cdot \vec{u}_b) \quad (3-3)$$

or, rewritten in matrix form,

$$\langle a, b \rangle = \int_S dS a^\dagger W b \quad (3-4)$$

where

$$W = \begin{pmatrix} h & \vec{0} \\ \vec{0} & g \end{pmatrix} . \quad (3-5)$$

The symbol, \dagger , is used to indicate that the matrix adjoint is to be taken.

\mathcal{L} is self-adjoint, that is, a vector, \vec{P} , exists such that:

$$\langle a, \mathcal{L} b \rangle - \langle \mathcal{L} a, b \rangle = \int_S \nabla_h \cdot \vec{P} dS . \quad (3-6)$$

S represents the surface area of the basin, ∇_h is the horizontal gradient,

and $\vec{P} = gh(\vec{u}_a \zeta_b + \vec{u}_b \zeta_a)$.

If ψ_n satisfies the equation, $\mathcal{L} \psi_n = \omega_n \psi_n$, then ψ_n is an eigenvector of \mathcal{L} with eigenvalue, ω_n . The set of all such eigenvectors form a complete set of basis vectors such that any continuous function, $\phi(x)$, can be expressed:

$$\phi(\vec{x}) = \sum_{n=-\infty}^{n=\infty} A_n \psi_n(\vec{x}) . \quad (3-7)$$

The self-adjointness of \mathcal{L} assures the orthogonality of the set, $\{\psi_n\}$.

Let the Green's function, $G(x, x', \omega)$, be defined by the equation,

$$(\mathcal{L} - \omega) G(x, x', \omega) = W^{-1} \delta(\vec{x} - \vec{x}') . \quad (3-8)$$

We next show that the Green's function, $G(x, x', \omega)$, has the following form:

$$G(x, x', \omega) = \sum_n \frac{\psi_n(\vec{x}) \psi_n^\dagger(x')}{\omega_n - \omega} . \quad (3-9)$$

Since $\psi_n(\vec{x})$ is a column vector and $\psi_n^\dagger(x')$ is a row vector, G represents a matrix operator. Since G is a matrix, we can reduce the left side to a scalar by left and right multiplying the left side of Eq. (3-9) by ψ_j and ψ_k , respectively. A similar operation is performed on the right side. The left side becomes:

$$\begin{aligned}
 & \langle \psi_j, (\mathcal{L} - \omega) G, \psi_k \rangle \\
 &= \langle \psi_j, \sum_n \psi_n(\vec{x}) \psi_n^\dagger(\vec{x}'), \psi_k \rangle \\
 &= \int_S \int_{S'} dS dS' \psi_j^\dagger(\vec{x}) W \sum_n \psi_n(\vec{x}) \psi_n^\dagger(x') W(x') \psi_k \\
 &= \sum_n \delta_{jn} \delta_{nk} = \delta_{jk} .
 \end{aligned} \tag{3-10}$$

The right side becomes:

$$\begin{aligned}
 & \langle \psi_j, W^{-1}(x') \delta(\vec{x} - \vec{x}'), \psi_k \rangle \\
 &= \int_S \int_{S'} dS dS' \psi_j^\dagger(\vec{x}) W(\vec{x}) \delta(\vec{x} - \vec{x}') W^{-1}(x') W(x') \psi_k(\vec{x}') \\
 &= \int_S \int_{S'} dS dS' \psi_j^\dagger(\vec{x}) W(\vec{x}) \delta(\vec{x} - \vec{x}') \psi_k(x') \\
 &= \int_S dS \psi_j^\dagger(\vec{x}) W(\vec{x}) \psi_k(\vec{x}') = \delta_{jk} .
 \end{aligned} \tag{3-11}$$

Since the results of the contractions, (3-10) and (3-11), are identical for all j, k , it follows that (3-8) satisfies (3-9).

A GREEN'S THEOREM FOR \mathfrak{L}

Green's theorem generally applies to the inhomogeneous equation,

$$L\psi = \rho(\vec{x}) \quad , \quad (3-12)$$

where, in particular, $L = \nabla^2$. Green's theorem is used extensively in the solution of electromagnetic field problems (Jackson, 1962). Morse and Feshbach (1953) describe a "generalized Green's theorem" for an arbitrary differential operator, \mathfrak{L} . The Green's theorem for \mathfrak{L} is derived as follows.

Assuming sinusoidal forcing, Eq. (3-1) can be written,

$$(\mathfrak{L} - \omega)\psi = i\chi \quad . \quad (3-13)$$

Rewriting Eq. (3-9),

$$(\mathfrak{L} - \omega)G = W^{-1}\delta(\vec{x} - \vec{x}') \quad .$$

Left dot multiply Eq. (3-13) by G and right multiply Eq. (3-9) by $\psi(x')$, and subtract Eq. (3-13) from Eq. (3-9): (The dot product between a matrix and a vector gives a vector and is defined as follows:

$$\langle \square , \bigcirc \rangle = \int_S dS \square^+ W \bigcirc \quad , \quad (3-14)$$

where \square represents the matrix and \bigcirc represents the vector.)

$$\begin{aligned} \langle W^{-1}\delta(\vec{x} - \vec{x}') , \psi(\vec{x}') \rangle &= -i\langle G, \chi \rangle + \langle (\mathfrak{L} - \omega)G, \psi \rangle \\ &\quad - \langle G, (\mathfrak{L} - \omega)\psi \rangle \quad . \end{aligned}$$

Therefore,

$$\begin{aligned} \psi(\vec{x}) &= -i\langle G, \chi \rangle + \langle (\mathfrak{L} - \omega)G, \psi \rangle \\ &\quad - \langle G, (\mathfrak{L} - \omega)\psi \rangle \quad . \end{aligned} \quad (3-15)$$

Now,

$$\begin{aligned} & \langle G, (\mathcal{L} - \omega)\psi \rangle \\ &= \sum_n \frac{\psi_n(\vec{x})}{\omega_n - \omega} (-i) \int_S dS (hf\hat{k}x\vec{u} - \vec{u}_n + g\nabla\zeta_n, \nabla \cdot h\vec{u}_n) W \left(\begin{matrix} \vec{u} \\ \zeta \end{matrix} \right) \end{aligned}$$

and

$$\begin{aligned} & \langle (\mathcal{L} - \omega)G, \psi \rangle \\ &= \sum_n \frac{\psi_n(\vec{x})}{\omega_n - \omega} (-i) \int_S dS (hf\hat{k}x\vec{u}_n \cdot \vec{u} + gh\nabla\zeta_n \cdot \vec{u} + g\nabla \cdot h\vec{u}_n\zeta_n) \end{aligned}$$

Consequently,

$$\begin{aligned} & \langle G, (\mathcal{L} - \omega)\psi \rangle - \langle (\mathcal{L} - \omega)G, \psi \rangle \\ &= \sum_n \frac{\psi_n(\vec{x})}{\omega_n - \omega} i \int_B gh\hat{n} \cdot (\vec{u}_n\zeta + \vec{u}_{\zeta_n}) dB \end{aligned} \quad (3-16)$$

where \hat{n} is an outward pointing unit vector normal to the boundary. B represents the boundary of the basin and S, the interior. By comparing Eq. (3-16) with Eq. (3-6), it can be seen that there exists a bilinear concomitant, \vec{P} , for the operator, $\mathcal{L} - \omega$, such that

$$\vec{P} = gh(\vec{u}_n\zeta + \vec{u}_{\zeta_n}) \quad (3-17)$$

Along the closed sections of the boundary, both $\hat{n} \cdot \vec{u}_n$ and $\hat{n} \cdot \vec{u}$ are zero so that the only contribution to Eq. (3-16) is from the opening. Here ζ_n is zero so that Eq. (3-16) becomes

$$\langle G, (\mathcal{L} - \omega)\psi \rangle - \langle (\mathcal{L} - \omega)G, \psi \rangle = \sum_n \frac{\psi_n(\vec{x})}{\omega_n - \omega} i \int_B dB \hat{n} \cdot \vec{u}_n\zeta \quad (3-18)$$

Also,

$$i \langle G, \chi \rangle = \sum_n \frac{\psi_n(\vec{x})}{\omega_n - \omega} i \int_S \vec{u}_n(\vec{x}') \cdot \vec{\tau}/\rho dS \quad (3-19)$$

Therefore, the Green's theorem becomes,

$$\psi(\vec{x}) = \sum_n \frac{\psi_n(\vec{x})}{\omega_n - \omega} \left\{ \int_B dB gh \hat{n} \cdot \vec{u}_n \zeta - \int_S dS \vec{u}_n \cdot \vec{\tau} / \rho \right\} . \quad (3-20)$$

THE FRICTIONAL, NON-SELF-ADJOINT CASE

In the frictional case, Eq.'s (2-9) and (2-10) are still of the form (3-1), but the operator, \mathcal{L} , is now

$$\mathcal{L} = i \begin{pmatrix} f\hat{k}x - R' & g\nabla \\ \nabla \cdot (h & 0 \end{pmatrix} \quad (3-21)$$

where $R' = \frac{R_0 + R_1 \lambda}{h}$. Since there does not exist a \vec{P} such that \mathcal{L} satisfies Eq. (3-6), \mathcal{L} is not self-adjoint.

However, an adjoint operator, $\tilde{\mathcal{L}}$, and a corresponding \vec{P} can always be found such that

$$\langle a, (\mathcal{L} - \omega)b \rangle - \langle (\tilde{\mathcal{L}} - \omega)a, b \rangle = \int_S dS \nabla \cdot \vec{P} \quad (3-22)$$

for any vectors, a and b.

Define \tilde{G} :

$$(\tilde{\mathcal{L}} - \omega)\tilde{G} = W^{-1} \delta(\vec{x} - \vec{x}') , \quad (3-23)$$

where,

$$\tilde{\mathcal{L}} = i \begin{pmatrix} f\hat{k}x + R' & g\nabla \\ \nabla \cdot (h & 0 \end{pmatrix} . \quad (3-24)$$

Following a development similar to that used to derive Eq. (3-17), \vec{P} is found to be

$$\vec{P} = gh(\vec{u}_n \zeta + \tilde{\zeta}_n \vec{u}) , \quad (3-25)$$

and Green's theorem takes the form,

$$\psi = -i \langle \tilde{G}, \chi \rangle + \langle \tilde{G}, \mathcal{L} \psi \rangle - \langle \tilde{\mathcal{L}} \tilde{G}, \psi \rangle . \quad (3-26)$$

Hence, $\tilde{\mathcal{L}}$ is the adjoint operator to \mathcal{L} and ψ_n , the adjoint eigenvector. Since \mathcal{L} is no longer self-adjoint, the solutions, ψ_n , to the eigenvalue equation for \mathcal{L} are no longer orthogonal, i.e.,

$$\langle \psi_n, \psi_m \rangle \neq \delta_{nm} . \quad (3-27)$$

However, the two sets, $\{\psi_n\}$ and $\{\tilde{\psi}_n\}$ are bi-orthogonal, that is, $\langle \psi_n, \tilde{\psi}_m \rangle = \delta_{nm}$. The Green's function takes on the form,

$$G(\vec{x}, \vec{x}', \omega) = \sum_n \frac{\psi_n(\vec{x}) \tilde{\psi}_n^\dagger(\vec{x}')}{\omega_n - \omega} . \quad (3-28)$$

Morse and Feshbach (1953)

\tilde{G} will be needed to derive the new Green's theorem. Assume that $\tilde{G} = G^\dagger$, that is,

$$\tilde{G}(\vec{x}, \vec{x}', \omega) = \sum_n \frac{\tilde{\psi}_n(\vec{x}') \psi_n^\dagger(\vec{x})}{\omega_n^* - \omega} , \quad (3-29)$$

and verify that Eq. (2-26) is satisfied. Since

$$(\mathcal{L}(\vec{x}) - \omega) G(\vec{x}, \vec{x}', \omega) = W^{-1} \delta(\vec{x} - \vec{x}')$$

and

$$(\tilde{\mathcal{L}}(\vec{x}') - \omega) \tilde{G}(\vec{x}, \vec{x}', \omega) = W^{-1} \delta(\vec{x} - \vec{x}') ,$$

then

$$(\mathcal{L}(\vec{x}) - \omega) G = (\tilde{\mathcal{L}}(\vec{x}') - \omega) \tilde{G}$$

or

$$\sum_n \psi_n(\vec{x}) \tilde{\psi}_n^\dagger(\vec{x}') = \sum_n \tilde{\psi}_n(\vec{x}') \psi_n^\dagger(\vec{x}) .$$

Expansion of the above sums shows the equality to be true since the off diagonal terms in both sums are zero according to Eq.'s (3-9) and (3-23).

Following a development similar to that used in the derivation of Eq. (3-15), a Green's theorem involving \mathcal{L} , $\tilde{\mathcal{L}}$, and \tilde{G} is obtained:

$$\psi(\vec{x}) = -i \langle \tilde{G}, \chi \rangle + \langle (\tilde{\mathcal{L}} - \omega) \tilde{G}, \psi \rangle - \langle \tilde{G}, (\mathcal{L} - \omega) \psi \rangle . \quad (3-30)$$

Substituting Eq.'s (3-29), (3-24), and (3-21) into Eq. (3-30) yields Eq. (3-31):

$$\psi(\vec{x}, \omega) = \sum_n \frac{\psi_n(\vec{x})}{\omega_n - \omega} i \left\{ \int_B dB gh \hat{n} \cdot \tilde{u}_n \zeta - \int_S dS \tilde{u}_n \cdot \vec{\tau} / \rho \right\} . \quad (3-31)$$

Eq. (3-31) allows the specification of the elevation on the boundary, B, or $\vec{\tau}$ over the surface, S, having once obtained the normal modes (eigenfunctions) of \mathcal{L} and $\tilde{\mathcal{L}}$. The forcing in this case acts through the adjoint eigenfunctions rather than through the eigenfunctions of \mathcal{L} . Hence, the degree to which a particular normal mode, ψ_n , is excited by forcing functions, $\zeta_0(\vec{x}, \omega)$ and $\vec{\tau}(\vec{x}, \omega)$, depends on how well the forcing functions "match" the $\tilde{\psi}_n$'s spatially.

In practice, the summation in Eq. (3-31) must extend over some finite number of terms, N. The convergence properties of the sum will depend on both the frequency dependent term, $1/(\omega_n - \omega)$, and the surface and line integrals enclosed in the brackets, { }. It will be shown that the energetic frequencies in the atmospheric forcing lie in periods longer than 12 hours. Hence, $\omega_n \gg \omega$ (as will be shown in the following section, the lowest mode has a period of about 6 hours) for energetically important ω 's, i.e., $\frac{1}{\omega_n - \omega} \cong \frac{1}{\omega_n}$. For a rectangular basin, $\omega_n \sim \left(\frac{n^2}{a^2} + \frac{m^2}{b^2} \right)^{1/2}$ where a and b are the basin dimensions.

For a linear basin, then, $\frac{1}{\omega_n - \omega} \propto \frac{1}{n}$, a non-convergent sequence.

The introduction of a second dimension does not improve the convergent characteristics of $\frac{1}{\omega_n - \omega}$. The surface and line integrals in Eq. (3-31) represent coupling coefficients between the forcing and the normal modes. For forcing that is weakly dependent on spatial variables (as in the case of the Bight), only the low order modes will contribute significantly. For large n , $\hat{n} \cdot \vec{u}_n$ oscillates rapidly across the opening, and \vec{u}_n oscillates rapidly over the interior, resulting in relatively small contributions from the two integrals. Hence, the nature of the forcing will ensure the convergence of the sum at large n .

For the special case of homogeneous forcing, Eq. (3-31) takes the following form:

$$\psi(x, \omega) = \sum_{n=1}^{\infty} \frac{\psi_n(\vec{x})}{\omega_n - \omega} i \left\{ gh \zeta_0(\omega) \int dB \hat{n} \cdot \vec{u}_n - \frac{\tau_x(\omega)}{\rho} \int dS \tilde{u}_n(\vec{x}') - \frac{\tau_y(\omega)}{\rho} \int dS \tilde{v}_n(\vec{x}') \right\} \quad (3-32)$$

The coupling of the various forcings depends, in the homogeneous case, on integral properties of the normal modes.

SECTION 4

NORMAL MODES FOR THE BIGHT OF ABACO

NUMERICAL METHOD

The Green's theorem (Eq. (3-32)) requires the specification of the ψ_n 's, i.e., the normal modes, which are, in turn, solutions to the homogeneous problem:

$$(\mathcal{L} - \omega_n) \psi_n = 0 \quad (4-1)$$

Homogeneous boundary conditions are: $\zeta_n = 0$ along the opening, and $\hat{n} \cdot \vec{u}_n = 0$ along the closed portions of the boundary. The eigenvalue equation (4-1) is solved using a technique called inverse iteration. The method was used by Steen (1972) to solve for the eigenvectors of a closed rectangular basin of variable depth and Coriolis parameter without friction. The method is, herein, adapted to handle variable geometry and a linear, spatially dependent, friction coefficient.

INVERSE ITERATION (FOR THE FRICTIONLESS CASE)

Following Steen, the equation

$$(\mathcal{L} - \omega') a'' = a' \quad (4-2)$$

is solved for a'' , where a' and ω' are initial guesses for ψ_n and ω_n , respectively.

Then,

$$a'' = (\mathcal{L} - \omega')^{-1} a' \quad (4-3)$$

An improved estimate for ω is obtained by left dot multiplying Eq. (4-2) by a'' , giving,

$$\langle a'', \mathcal{L} a'' \rangle - \omega' \langle a'', a'' \rangle = \langle a'', a' \rangle, \quad (4-4)$$

so that an improved estimate, ω'' , can be defined:

$$\omega'' = \frac{\langle a'', \mathcal{L} a'' \rangle}{\langle a'', a'' \rangle} = \frac{\langle a'', a' \rangle}{\langle a'', a'' \rangle} + \omega'. \quad (4-5)$$

Since ω'' approaches the Rayleigh ratio as a'' approaches ψ_n , and the Rayleigh ratio is stationary near ω_n , successive corrections to ω' will approach zero.

DISCRETIZATION

Equation (3-1) can be written explicitly as

$$i\omega \vec{u} + \hat{k}x\vec{u} + g\nabla\zeta = 0 \quad (4-6)$$

$$i\omega\zeta + \nabla \cdot h\vec{u} = 0. \quad (4-7)$$

Before discretizing, the equations are first scaled by multiplying Eq. (3-6) by $h/\Delta s$ where Δs is the mesh size to be used. The following substitutions are then made:

$$\vec{\bar{u}} = h\vec{u}/\Delta s \quad (4-8)$$

$$\bar{h} = gh/\Delta s^2. \quad (4-9)$$

Equations (3-6) and (3-7) become:

$$i\omega \vec{\bar{u}} + \hat{k}x\vec{\bar{u}} + \bar{h}\nabla\zeta = 0 \quad (4-10)$$

$$i\omega\zeta + \nabla \cdot \vec{\bar{u}} = 0. \quad (4-11)$$

The dot product becomes:

$$\langle a, a' \rangle = \sum_i \zeta_i^* \zeta_i' + \bar{u}_i^* \bar{u}_i' / \bar{h} + \bar{v}_i^* \bar{v}_i' / \bar{h} , \quad (4-12)$$

where i is the lattice point index. The overbar will, hereafter, be dropped.

The basin is discretized using a Richardson lattice. Figure 4-1 below shows a simple basin utilizing this type of lattice.

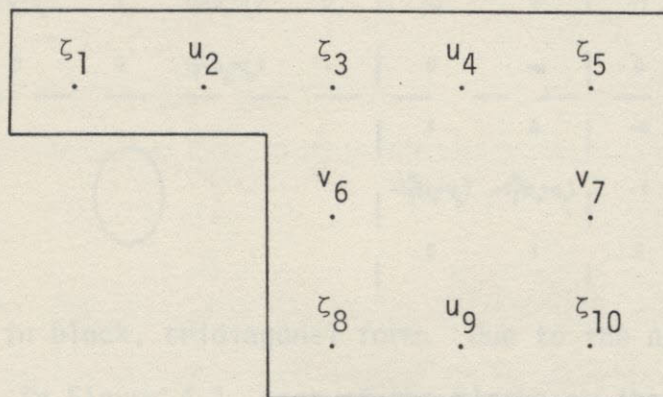


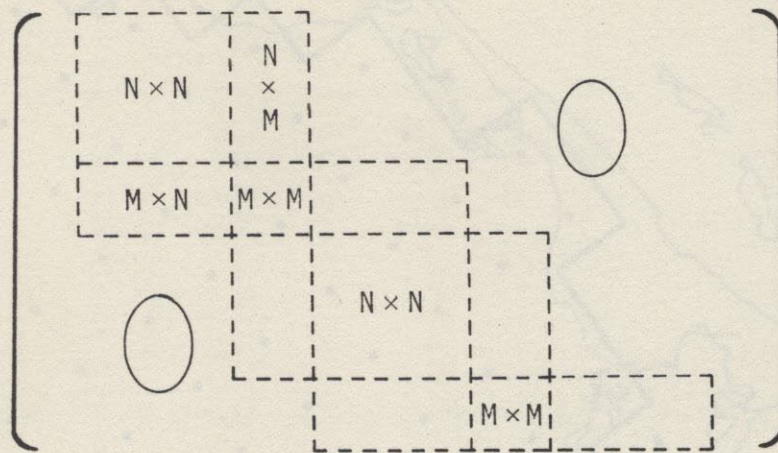
Figure 4-1.

Boundary conditions in the x and y directions are $u = 0$ and $v = 0$, respectively. Since the Coriolis term must be evaluated at each velocity point, and the appropriate velocity component is not available at each velocity point, the velocity is space-averaged over the four nearest neighbors:

$$\square v_i = \frac{1}{4q_i} \sum_{k=1}^4 (q_i + q_k) v_k / 2 , \quad (4-13)$$

where

$$q_i = f / h_i .$$



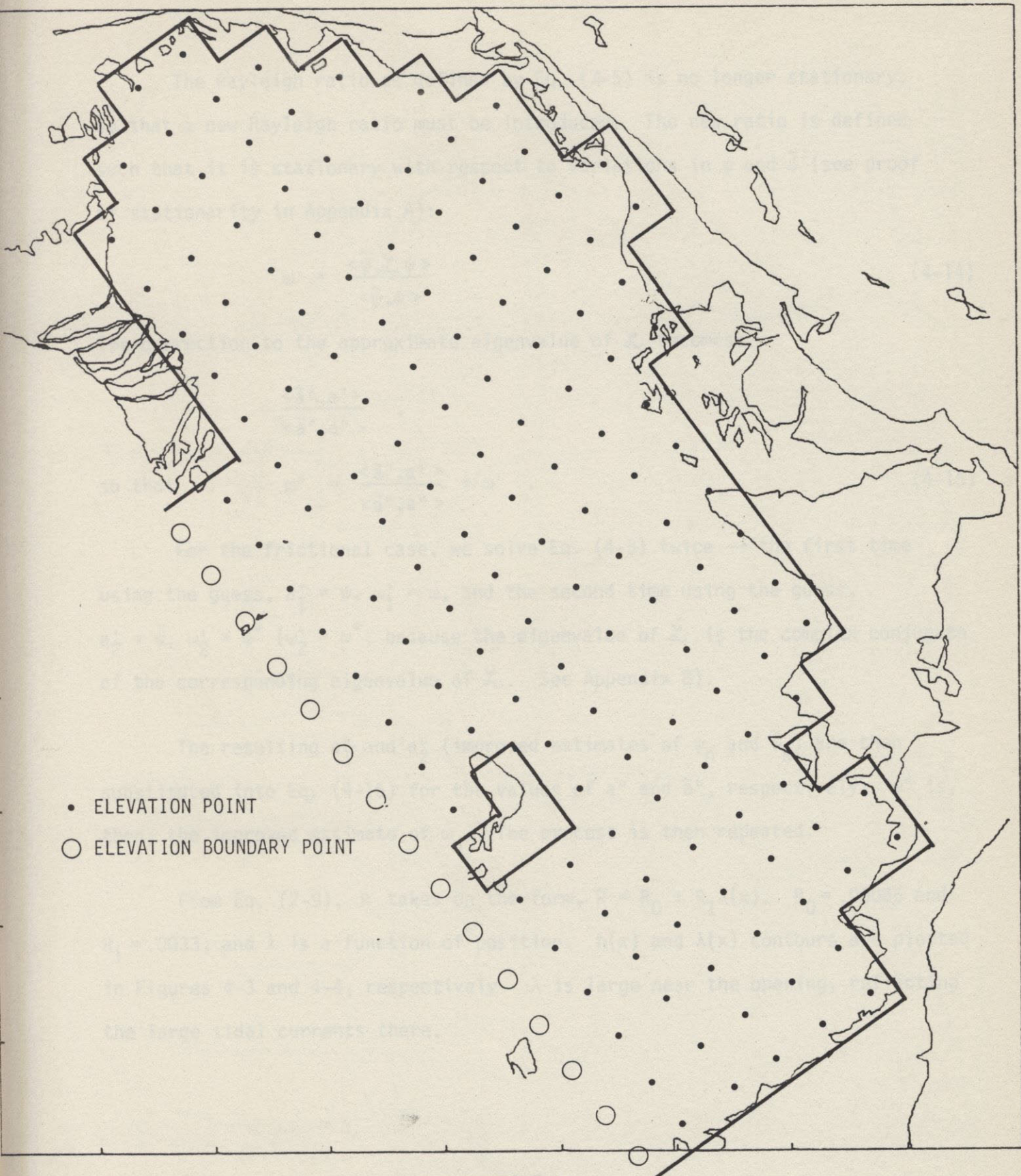
N represents the number of ζ - u elements in each odd-numbered row of lattice points. M represents the number of v elements in each even numbered row of lattice points.

Interior boundaries are introduced by striking the relevant u point or v point depending on whether the boundary is to be east-west or north-south. An exterior open boundary (B.C. $\zeta = 0$) can be obtained by striking out the relevant ζ point. In this way the discretized version of the Bight of Abaco shown in Figure 4-2 is built up.

Each iteration consists of solving Eq. (4-3) and then Eq. (4-5) using as input the value of a'' obtained from Eq. (4-3).

THE FRICTIONAL CASE

The introduction of linear friction requires the calculation of $\tilde{\psi}$ as well as ψ and a rework of the Rayleigh ratio's role in the inverse iteration scheme. The discretized \mathcal{L} operator contains the friction term on the diagonal at all velocity points.



ELEVATION GRID

Figure 4-2

The Rayleigh ratio as defined by Eq. (4-5) is no longer stationary, so that a new Rayleigh ratio must be introduced. The new ratio is defined such that it is stationary with respect to variations in ψ and $\tilde{\psi}$ (see proof of stationarity in Appendix A):

$$\omega = \frac{\langle \tilde{\psi}, \mathcal{L} \psi \rangle}{\langle \tilde{\psi}, \psi \rangle} \quad (4-14)$$

The correction to the approximate eigenvalue of \mathcal{L} becomes:

$$\frac{\langle \tilde{a}'' , a' \rangle}{\langle \tilde{a}'' , a'' \rangle} ,$$

so that
$$\omega'' = \frac{\langle \tilde{a}'' , a' \rangle}{\langle \tilde{a}'' , a'' \rangle} + \omega' \quad (4-15)$$

For the frictional case, we solve Eq. (4-3) twice — the first time using the guess, $a_1' = \psi$, $\omega_1' = \omega$, and the second time using the guess, $a_2' = \tilde{\psi}$, $\omega_2' = \omega^*$ ($\omega_2' = \omega^*$, because the eigenvalue of \mathcal{L} is the complex conjugate of the corresponding eigenvalue of \mathcal{L} . See Appendix B).

The resulting a_1'' and a_2'' (improved estimates of ψ_n and $\tilde{\psi}_n$) are then substituted into Eq. (4-15) for the values of a'' and \tilde{a}'' , respectively. ω'' is, then, the improved estimate of ω_n . The process is then repeated.

From Eq. (2-9), R takes on the form, $R = R_0 + R_1 \lambda(x)$. $R_0 = .00086$ and $R_1 = .0033$, and λ is a function of position. $h(x)$ and $\lambda(x)$ contours are plotted in Figures 4-3 and 4-4, respectively. λ is large near the opening, reflecting the large tidal currents there.

4-8

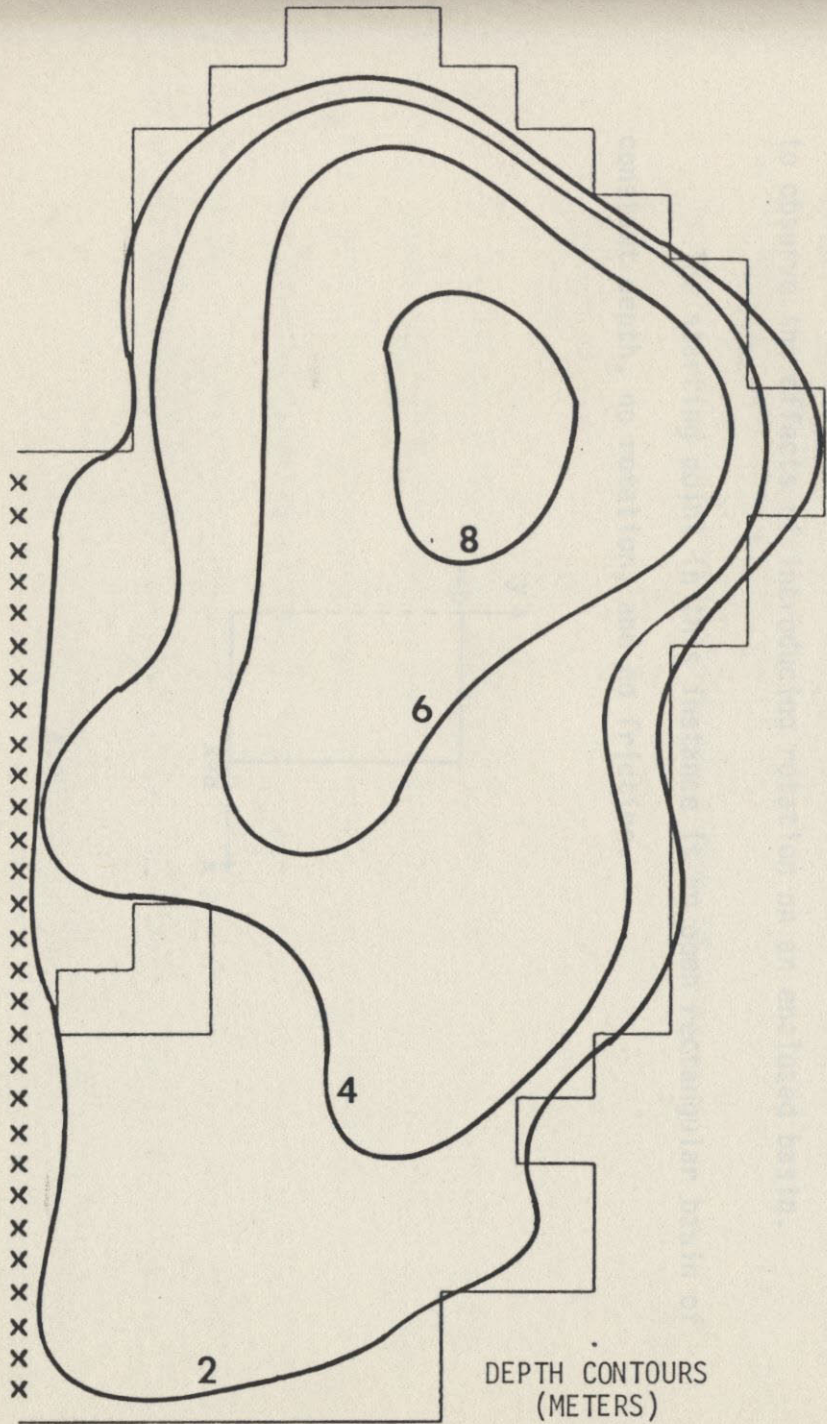


Figure 4-3

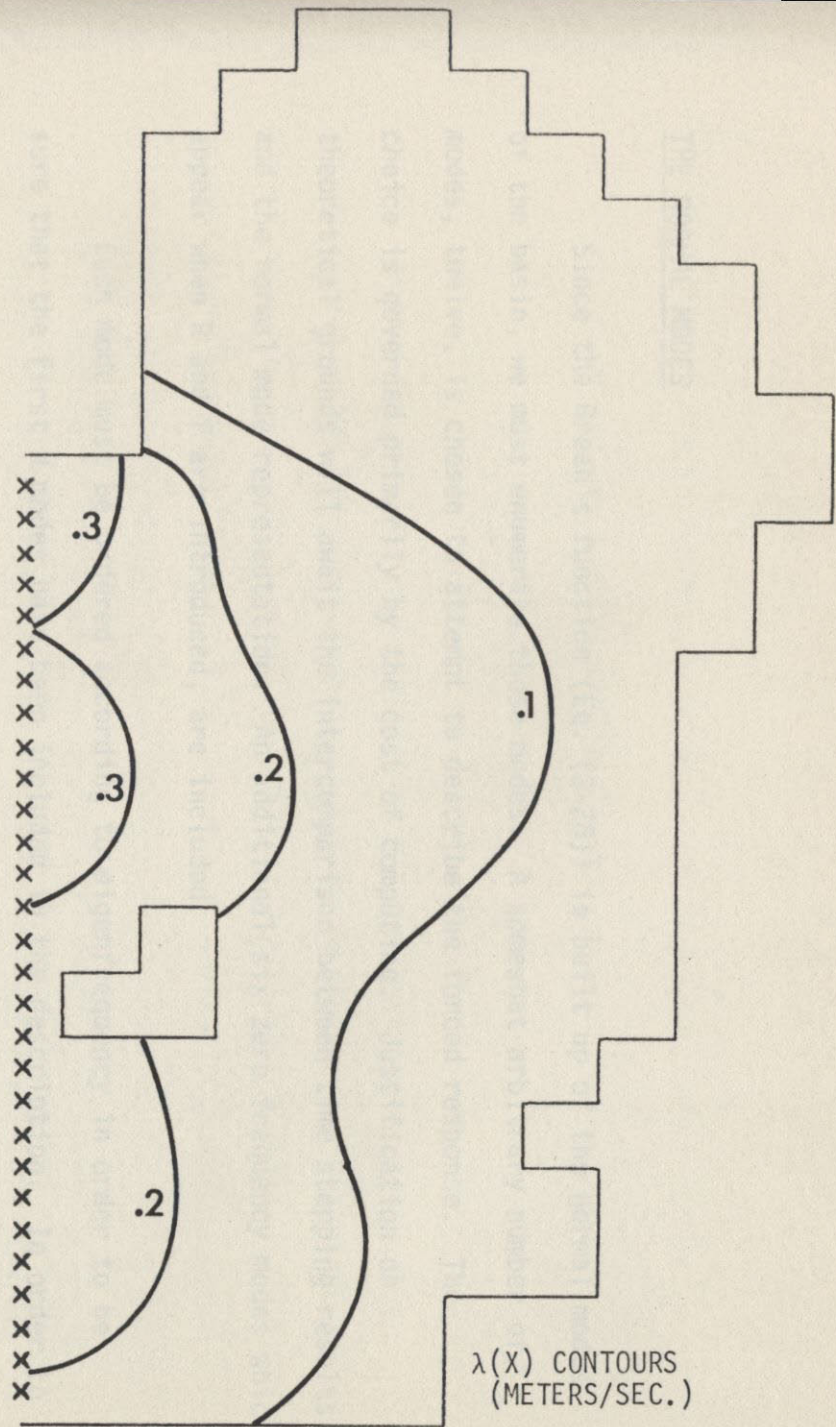


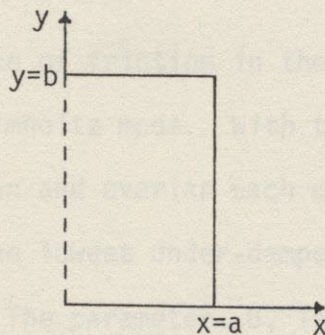
Figure 4-4

THE NORMAL MODES

Since the Green's function (Eq. (3-28)) is built up of the normal modes of the basin, we must enumerate these modes. A somewhat arbitrary number of modes, twelve, is chosen to attempt to describe the forced response. The choice is governed primarily by the cost of computing. Justification on theoretical grounds will await the intercomparison between time stepping results and the normal mode representation. An additional six zero frequency modes which appear when R and f are introduced, are included.

Each mode must be ordered according to eigenfrequency in order to be sure that the first N modes have been included in the description. In order to maintain such an ordering, a simple problem whose solutions are known analytically is used as a starting point, and each mode is tracked as various features such as depth and boundary geometry are changed. This technique was used by Rao (1966) to observe the effects of introducing rotation on an enclosed basin.

The starting point in this instance is an open rectangular basin of constant depth, no rotation, and no friction.



This problem has the well-known solution,

$$\zeta_{m,n}(x,y) = \sum_{m,n} A_{mn} \sin \frac{(2m+1)}{2} \frac{\pi x}{a} \cos n\pi y/b \quad (4-16)$$

$$\omega_{m,n} = \pi \sqrt{gh} \left[\left(\frac{2m+1}{2a} \right)^2 + \frac{n^2}{b^2} \right]^{1/2} \quad \begin{array}{l} m = 0,1,2 \cdot \\ n = 0,1,2 \cdot \end{array} \quad (4-17)$$

The geometry is then complicated by introducing a small lip at the northwest end of the opening. Inverse iteration is used to solve for the new normal modes and frequencies using Eq.'s (4-16) and (4-17) to obtain initial guesses. The northwest section of the opening is gradually closed in steps until about two thirds of the original opening remains open. The solid boundaries are then moved in two steps to a geometrical shape that approximates the boundaries of the Bight of Abaco. An island is introduced near the opening during the second geometry change. Next, the bottom topography is changed to agree with actual depths. Rotation is introduced and, finally, friction is included. The progression of changes is displayed in Figure 4-5. The lines represent the elevation nodes. The evolution of the eigenfrequencies is plotted in Figure 4-6. The eigenfrequencies are listed in Table I.

RESONANT Q's

The strong influence of friction in the shallow Bight is evidenced by the overdamping of the Helmholtz mode. With the friction coefficient so large, the resonant spikes broaden and overlap each other along the frequency axis. The amplitudes of the three lowest under-damped modes are plotted against frequency in Figure 4-7. The parameter, B, is a normalizing constant used to adjust the peak power for each mode to the same level. The resonances are

OPEN
BASIN
CONSTANT
DEPTH

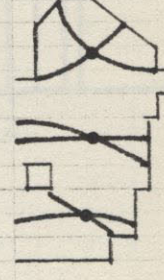
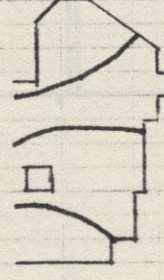
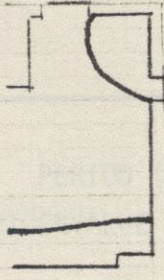
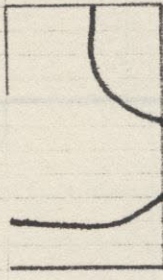
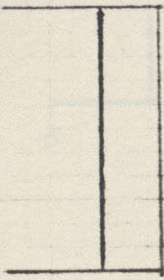
SEVEN
ELEMENT
LIP

GEOMETRY
CHANGE
NO.1

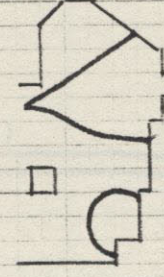
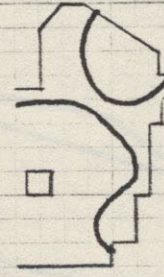
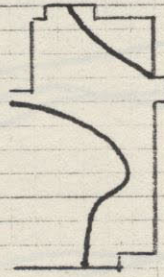
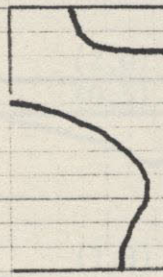
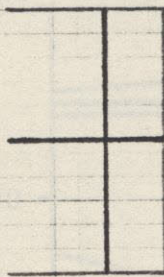
GEOMETRY
CHANGE
NO.2

BOTTOM
TOPO-
GRAPHY

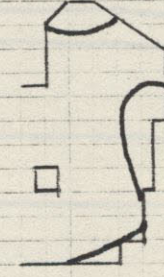
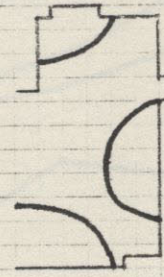
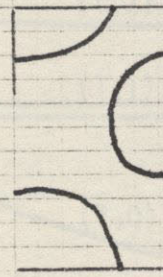
ROTATION



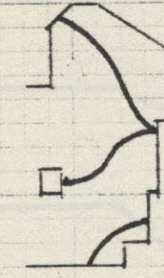
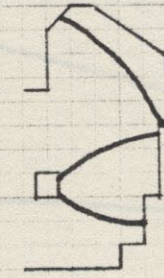
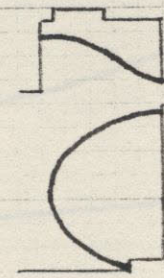
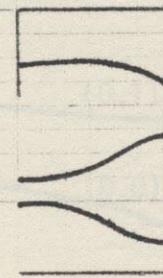
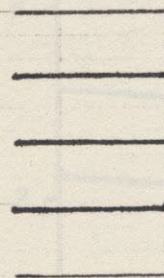
MODE (1,0)



MODE (1,1)



MODE (1,2)



MODE (0,3)

EVOLUTION OF THE ELEVATION NODES
FOR FOUR SELECTED EIGEN MODES

Figure 4-5

NSU LIBRARY

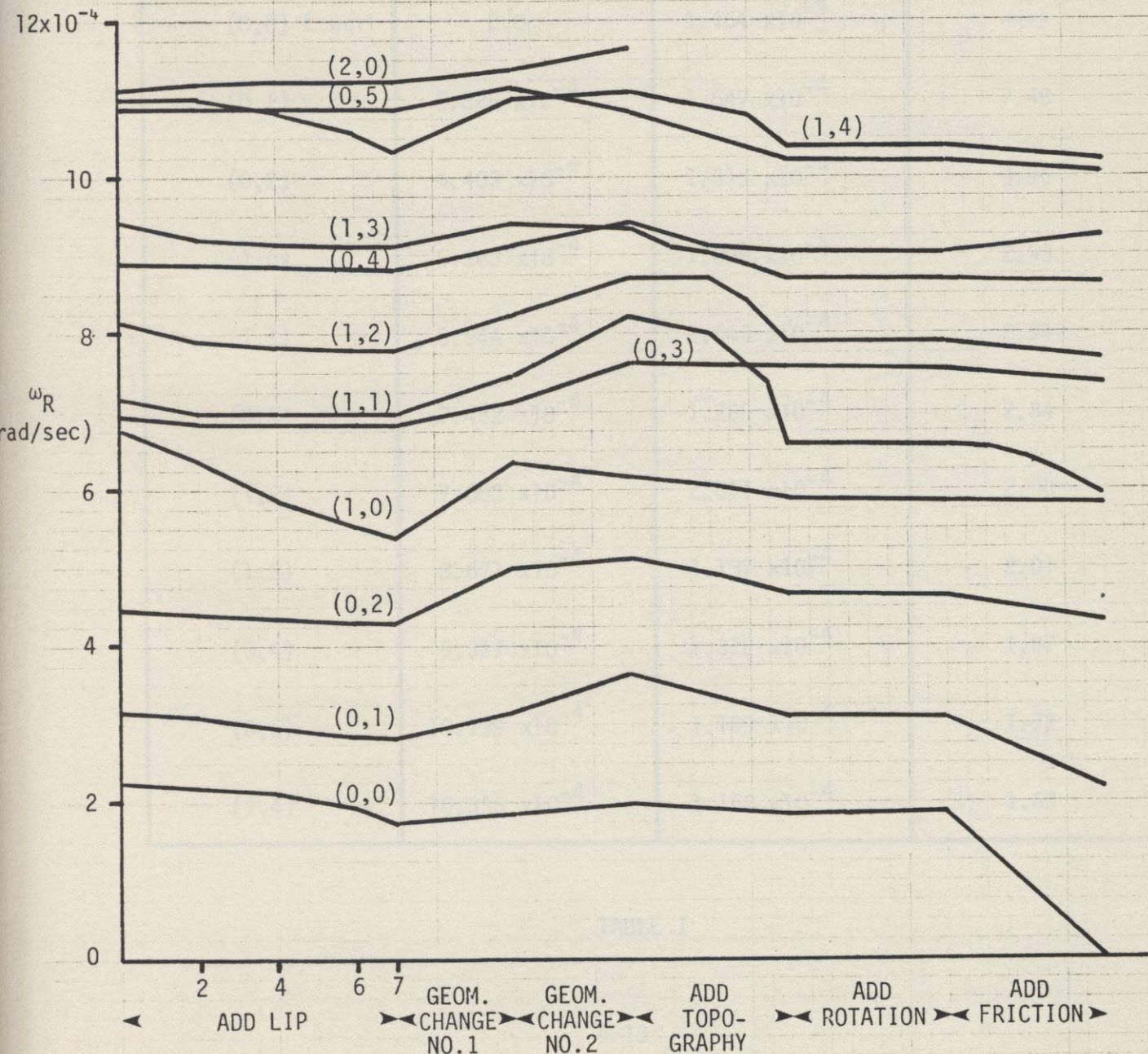
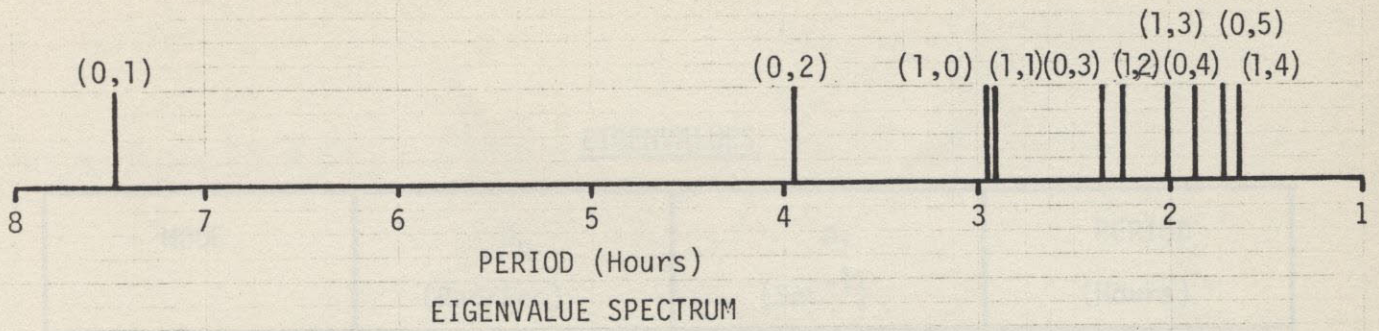


Figure 4-6

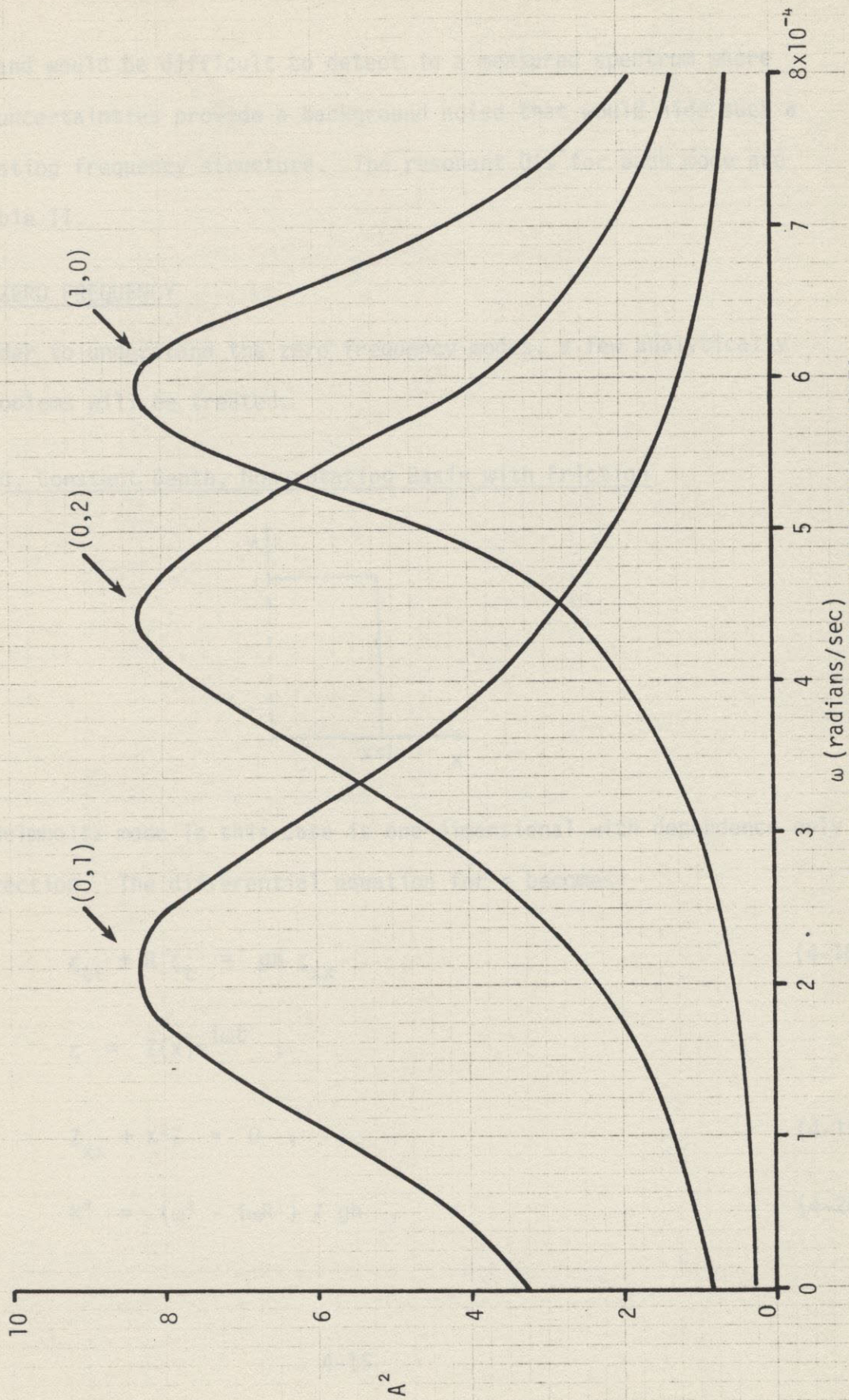
EIGENVALUES

MODE	Ω_R (Rad/Sec)	Ω_I (Sec ⁻¹)	PERIOD (Hours)
(0,0) Upper	0.0	1.510×10^{-4}	----
(0,0) Lower	0.0	1.464×10^{-4}	----
(0,1)	2.325×10^{-4}	1.647×10^{-4}	7.48
(0,2)	4.403×10^{-4}	1.513×10^{-4}	3.96
(1,0)	5.963×10^{-4}	1.096×10^{-4}	2.93
(1,1)	5.944×10^{-4}	2.543×10^{-4}	2.94
(0,3)	7.462×10^{-4}	1.265×10^{-4}	2.34
(1,2)	7.603×10^{-4}	2.011×10^{-4}	2.30
(1,3)	8.671×10^{-4}	1.137×10^{-4}	2.01
(0,4)	9.327×10^{-4}	1.372×10^{-4}	1.87
(0,5)	10.139×10^{-4}	1.169×10^{-4}	1.72
(1,4)	10.335×10^{-4}	1.168×10^{-4}	1.69

TABLE I

NSU LIBRARY

$$A = \frac{B}{|\omega_n - \omega|}$$



POWER SPECTRUM FOR THE LOWEST THREE UNDERDAMPED MODES
Figure 4-7

JOHN WILEY & SONS, INC. · BROOKLYN 17, N. Y.

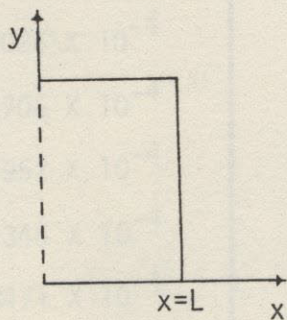
NSU LIBRARY

quite broad and would be difficult to detect in a measured spectrum where statistical uncertainties provide a background noise that would hide such a slowly undulating frequency structure. The resonant Q's for each mode are listed in Table II.

THE CASE OF ZERO FREQUENCY

In order to understand the zero frequency modes, a few analytically tractable problems will be treated.

Semi-enclosed, Constant Depth, Non-rotating Basin with Friction



The Helmholtz mode in this case is one-dimensional with dependence only in the x direction. The differential equation for ζ becomes:

$$\zeta_{tt} + R'\zeta_t = gh \zeta_{xx} \quad (4-18)$$

If $\zeta = Z(x)e^{i\omega t}$,

$$Z_{xx} + K^2Z = 0 \quad (4-19)$$

where $K^2 = (\omega^2 - i\omega R') / gh$. (4-20)

NSU LIBRARY

NORMAL MODE RESONANT Q'S

MODE	Ω_R (RAD/SEC)	Q
(0,1)	2.3250×10^{-4}	0.93
(0,2)	4.4031×10^{-4}	1.45
(1,0)	5.9633×10^{-4}	2.70
(1,1)	5.9436×10^{-4}	1.36
(0,3)	7.4616×10^{-4}	2.78
(1,2)	7.6026×10^{-4}	2.03
(1,3)	8.6706×10^{-4}	3.72
(0,4)	9.4952×10^{-4}	4.04
(0,5)	10.1346×10^{-4}	4.05
(1,4)	10.3471×10^{-4}	4.14

TABLE II

NSU LIBRARY

Boundary conditions require that:

$$K = (2n+1) \pi / 2L \quad n = 0,1,2,\dots \quad (4-21)$$

In particular, $K = \pi / 2L$ (4-22)

for the Helmholtz mode.

Eliminating K from Eq.'s (4-20) and (4-22) we get,

$$\omega^2 + i\omega R' - \pi^2 gh / 4L^2 = 0 \quad , \quad (4-23)$$

so that if $\omega = \omega_R + i\omega_I$,

$$\omega_R^2 = \pi^2 gh / 4L^2 - R'^2 / 4 \quad (4-24)$$

and $\omega_I = R' / 2 \quad . \quad (4-25)$

Defining $R'_C \equiv \pi \sqrt{gh} / L$, then for $R' < R'_C$, ω_R is real and describes a circle as a function of R' . ω_I has a linear dependence on R' . There are two solutions, $|\omega_R| + i\omega_I$ and $-|\omega_R| + i\omega_I$. For $R' > R'_C$, ω_R is imaginary and, therefore, ω is pure imaginary. Two roots result:

$$\omega = i (R' / 2 \pm \sqrt{ R'^2 / 4 - \pi^2 gh / 4L^2 }) \quad .$$

The imaginary part of ω is plotted as a function of R' in Figure 4-8.

Semi-enclosed, Constant Depth, Rotating Basin with Friction

A numerical solution for the Helmholtz mode is obtained in the case of the semi-enclosed basin on a rotating f plane. Results are shown in Figure 4-9. It can be seen that the introduction of rotation produces a third solution,

NSU LIBRARY

$\omega = iR'$. The other solutions shown in Figure 4-9 resemble the solutions for the non-rotating basin of Figure 4-8.

The Circular Basin

An analytical solution exists for the case of a constant depth, circular, fully enclosed basin on a rotating f plane (Lamb, 1932). With slight modification, the same treatment yields a solution for a basin influenced by linear bottom friction (see Appendix C). The resulting differential equation is of the form,

$$\nabla^2 \zeta + K^2 \zeta = 0 \quad , \quad (4-26)$$

where

$$K^2 = \frac{\omega^2(2\omega + R') - i\omega R'(i\omega + R') - i\omega^2 f^2}{gh(i\omega + R')} \quad . \quad (4-27)$$

ω and K are the complex frequency and the complex wave number, respectively.

Consider the basin to be fully open rather than fully closed -- that is, rather than a vertical wall enclosing the basin, let a very large discontinuity in bottom depth exist along the periphery. The resulting boundary condition to be satisfied is:

$$\zeta_{r=a} = 0 \quad . \quad (4-28)$$

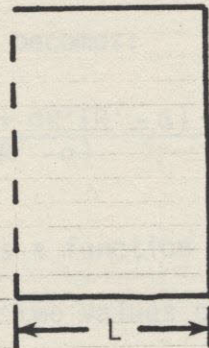
Solutions to Eq. (4-26) are of the form,

$$\zeta_n = A_n J_n(Kr) e^{in\phi} \quad .$$

Eq. (4-28) requires that $J_n(Ka) = 0$, or,

$$K_{m,n} = Z_{m,n} / a \quad . \quad (4-29)$$

HELMHOLTZ MODE
 FOR NON-ROTATING, CONSTANT DEPTH BASIN
 WITH FRICTION



$L = 50 \text{ km}$
 Depth = 10 meters

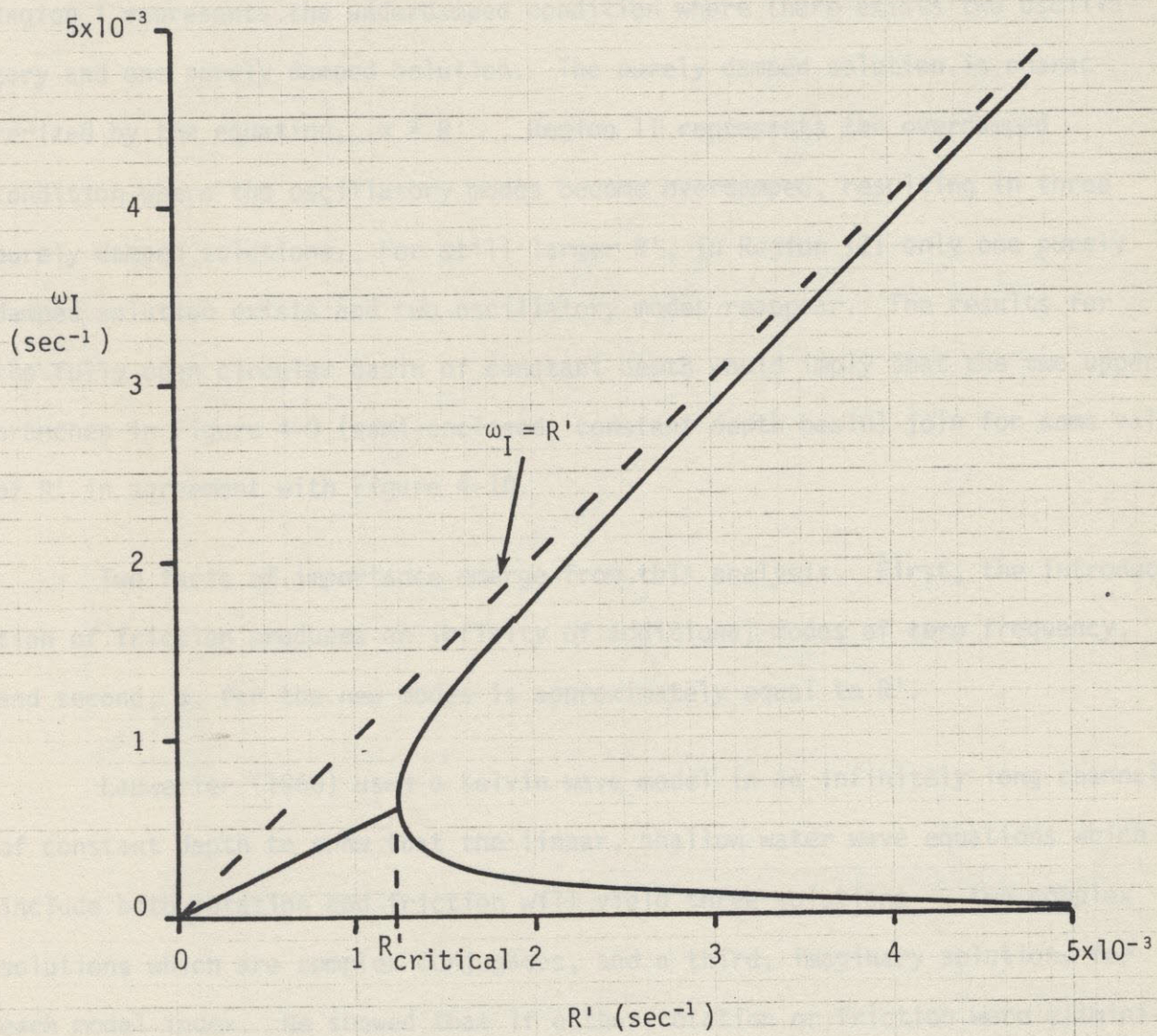


Figure 4-8

$Z_{m,n}$ is the m th zero of the Bessel function. The zero frequency case is investigated by setting $\omega = i\alpha$ and searching for possible solutions for α . Upon substituting for ω , Eq. (4-27) becomes:

$$K^2 = \frac{-\alpha^2(R' - \alpha) + \alpha R'(R' - \alpha) + \alpha f^2}{gh(R' - \alpha)} \quad (4-30)$$

Eq. (4-30) is solved for α as a function of R' for fixed K by using a Newton-Raphson method. Results for two values of K are shown in Figure 4-10. Region I represents the underdamped condition where there exists two oscillatory and one purely damped solution. The purely damped solution is characterized by the equation, $\alpha \cong R'$. Region II represents the overdamped condition where the oscillatory modes become overdamped, resulting in three purely damped solutions. For still larger R' , in Region III only one purely damped solution exists and two oscillatory modes reappear. The results for the fully open circular basin of constant depth would imply that the two upper branches in Figure 4-9 (semi-enclosed, constant depth basin) join for some value of R' in agreement with Figure 4-10.

Two facts of importance emerge from this analysis. First, the introduction of friction produces an infinity of additional modes of zero frequency, and second, α , for the new modes is approximately equal to R' .

Lauwerier (1960) used a Kelvin wave model in an infinitely long channel of constant depth to show that the linear, shallow water wave equations which include both rotation and friction will yield three solutions -- two complex solutions which are complex conjugates, and a third, imaginary solution, for each modal index. He showed that if either rotation or friction were eliminated, the imaginary solution would disappear.

HELMHOLTZ MODE
FOR ROTATING, CONSTANT DEPTH BASIN
WITH FRICTION

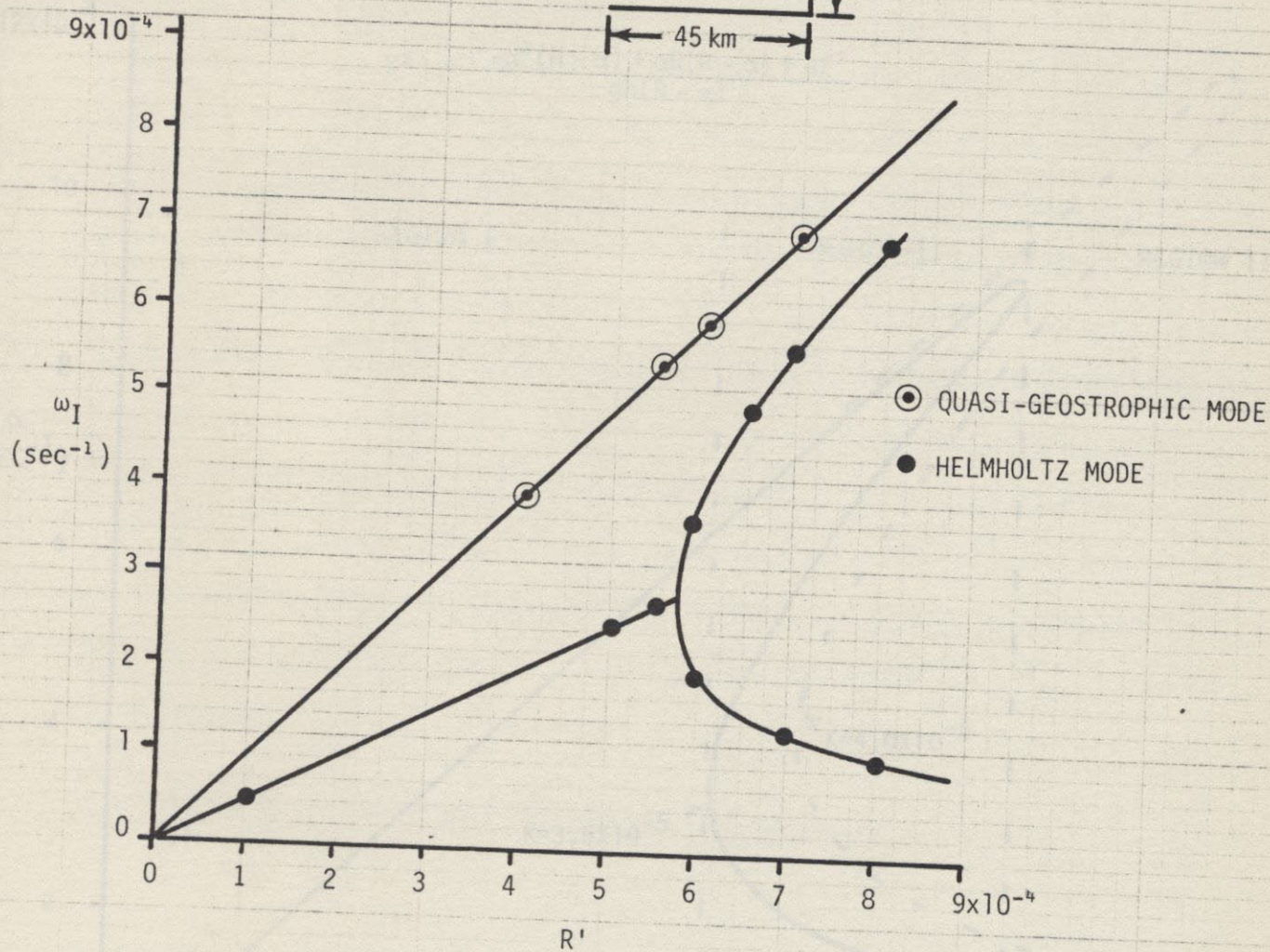
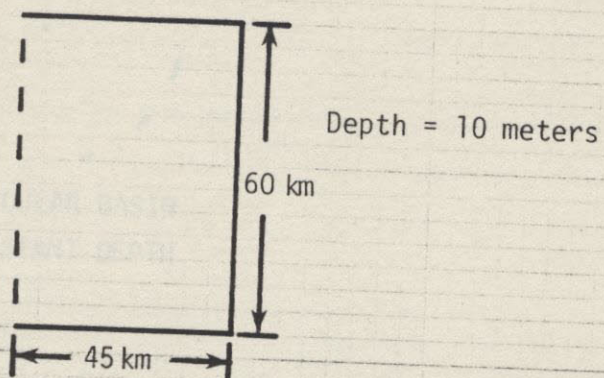
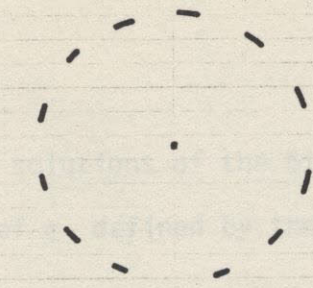


Figure 4-9

NSU LIBRARY

DAMPING FACTOR, α , VERSUS DRAG COEFFICIENT FOR ZERO FREQUENCY MODES



OPEN CIRCULAR BASIN
OF CONSTANT DEPTH

$$K^2 = \frac{-\alpha^2(R - \alpha) + \alpha R(R - \alpha) + \alpha f^2}{gh(R - \alpha)}$$

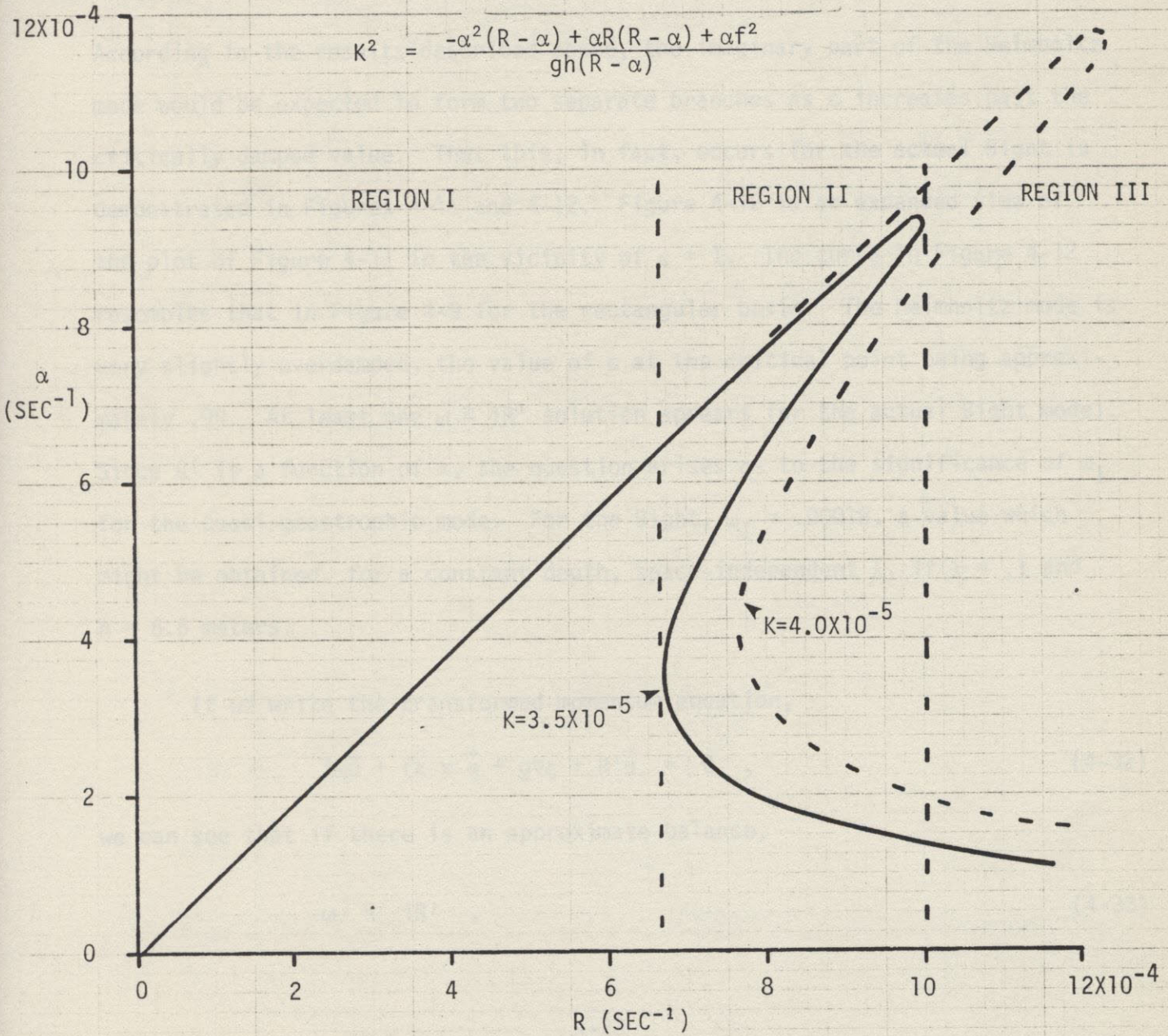


Figure 4-10

The Bight of Abaco Model

The zero frequency solutions of the Bight of Abaco model are investigated for varying values of ϵ , defined by the relation,

$$R(x) = \epsilon(R_0 + R_1\lambda(\vec{x})) \quad (4-31)$$

where $0 < \epsilon < 1$.

According to the results described above, the imaginary part of the Helmholtz mode would be expected to form two separate branches as ϵ increases past the critically damped value. That this, in fact, occurs for the actual Bight is demonstrated in Figures 4-11 and 4-12. Figure 4-12 is an expanded view of the plot of Figure 4-11 in the vicinity of $\epsilon = 1$. The curve in Figure 4-12 resembles that in Figure 4-9 for the rectangular basin. The Helmholtz mode is very slightly overdamped, the value of ϵ at the critical point being approximately .99. At least one $\omega \cong iR'$ solution appears for the actual Bight model. Since R' is a function of x , the question arises as to the significance of ω_I for the quasi-geostrophic mode. For the Bight, $\omega_I = .00018$, a value which might be obtained, for a constant depth, space-independent λ , if $\lambda = .1$ and $h = 6.6$ meters.

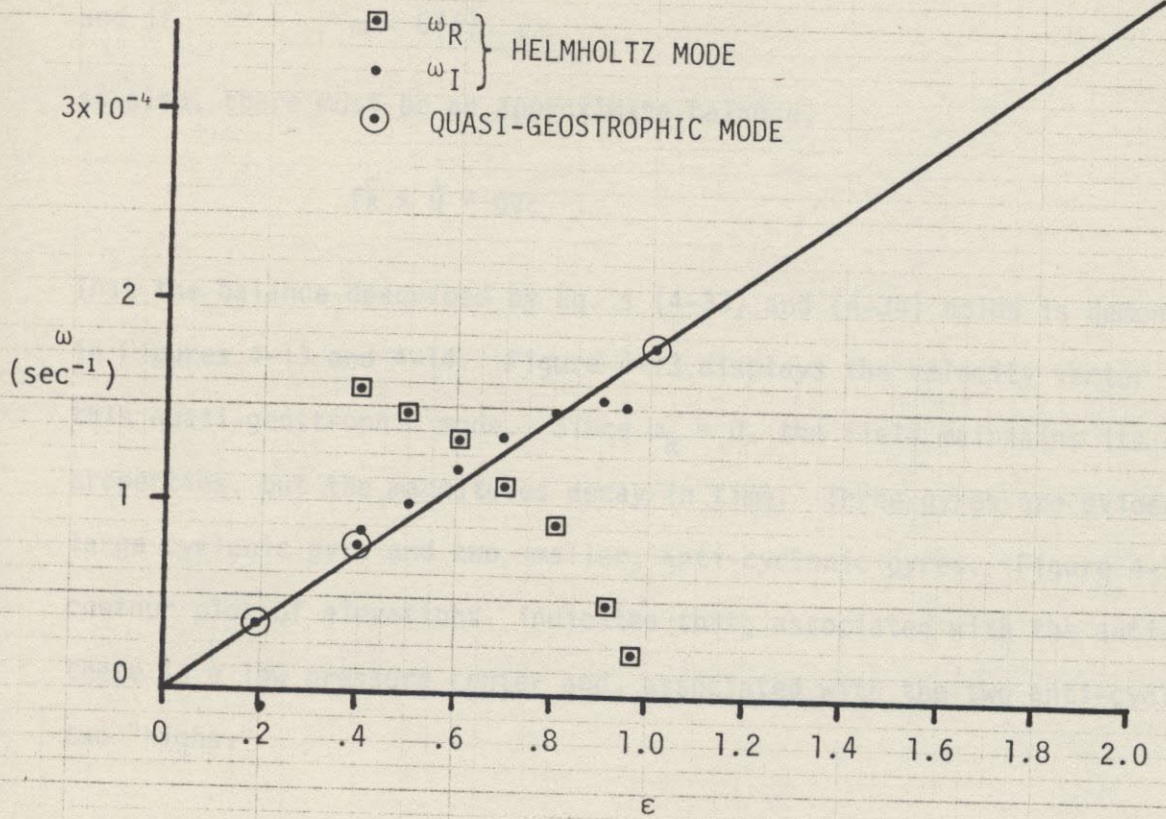
If we write the transformed momentum equation,

$$i\omega\vec{u} + f\hat{k} \times \vec{u} + g\nabla\zeta + R'\vec{u} = 0 \quad , \quad (4-32)$$

we can see that if there is an approximate balance,

$$\omega \cong iR' \quad , \quad (4-33)$$

FULL BIGHT MODEL



$$R(x) = \epsilon(R_0 + R_1 \lambda(x))$$

$$R_0 = .00086$$

$$R_1 = .0033$$

Figure 4-11

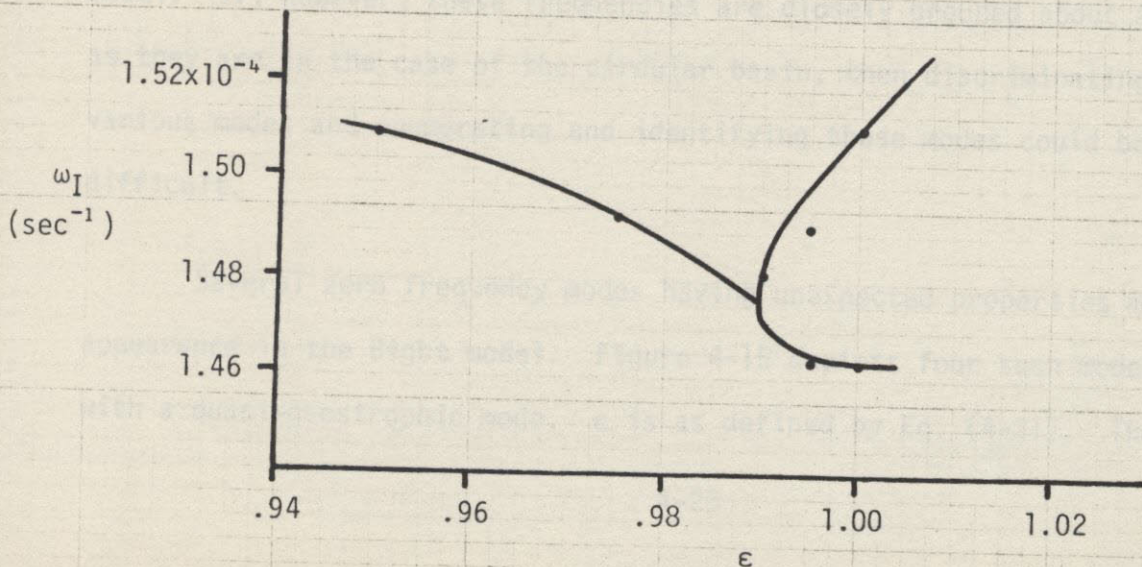


Figure 4-12

NSU LIBRARY

and if $\omega \sim 0(f)$,

so also, there must be an approximate balance,

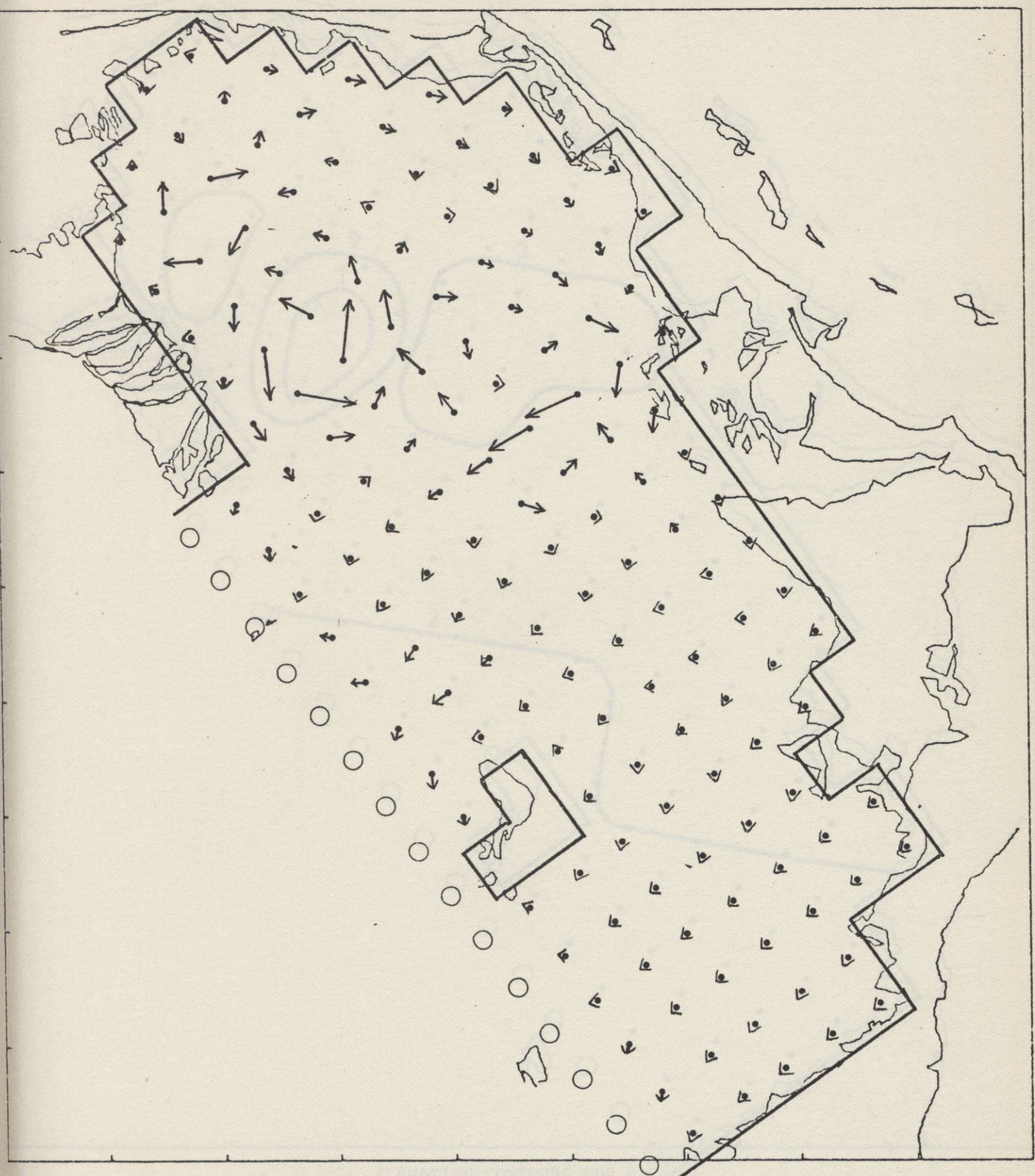
$$f\hat{k} \times \vec{u} \cong g\nabla\zeta . \quad (4-34)$$

That the balance described by Eq.'s (4-33) and (4-34) holds is demonstrated in Figures 4-13 and 4-14. Figure 4-13 displays the velocity vector field for this quasi-geostrophic mode. Since $\omega_R = 0$, the field maintains its directional properties, but the magnitudes decay in time. Three gyres are evident -- a large cyclonic gyre and two smaller, anti-cyclonic gyres. Figure 4-14, a contour plot of elevations, indicates that, associated with the anti-cyclone, there is a low pressure center and, associated with the two anti-cyclones are two "highs."

Additional Zero Frequency Modes

Since the simplified, circular basin model, treated analytically above, possessed an infinity of quasi-geostrophic modes -- one for each oscillatory mode -- we can expect to observe a large number of such modes in the Bight model. If, however, these frequencies are closely grouped about a single R' , as they are in the case of the circular basin, then discriminating between the various modes and enumerating and identifying these modes could be quite difficult.

Several zero frequency modes having unexpected properties make their appearance in the Bight model. Figure 4-15 depicts four such modes, together with a quasi-geostrophic mode. ϵ is as defined by Eq. (4-31). These modes

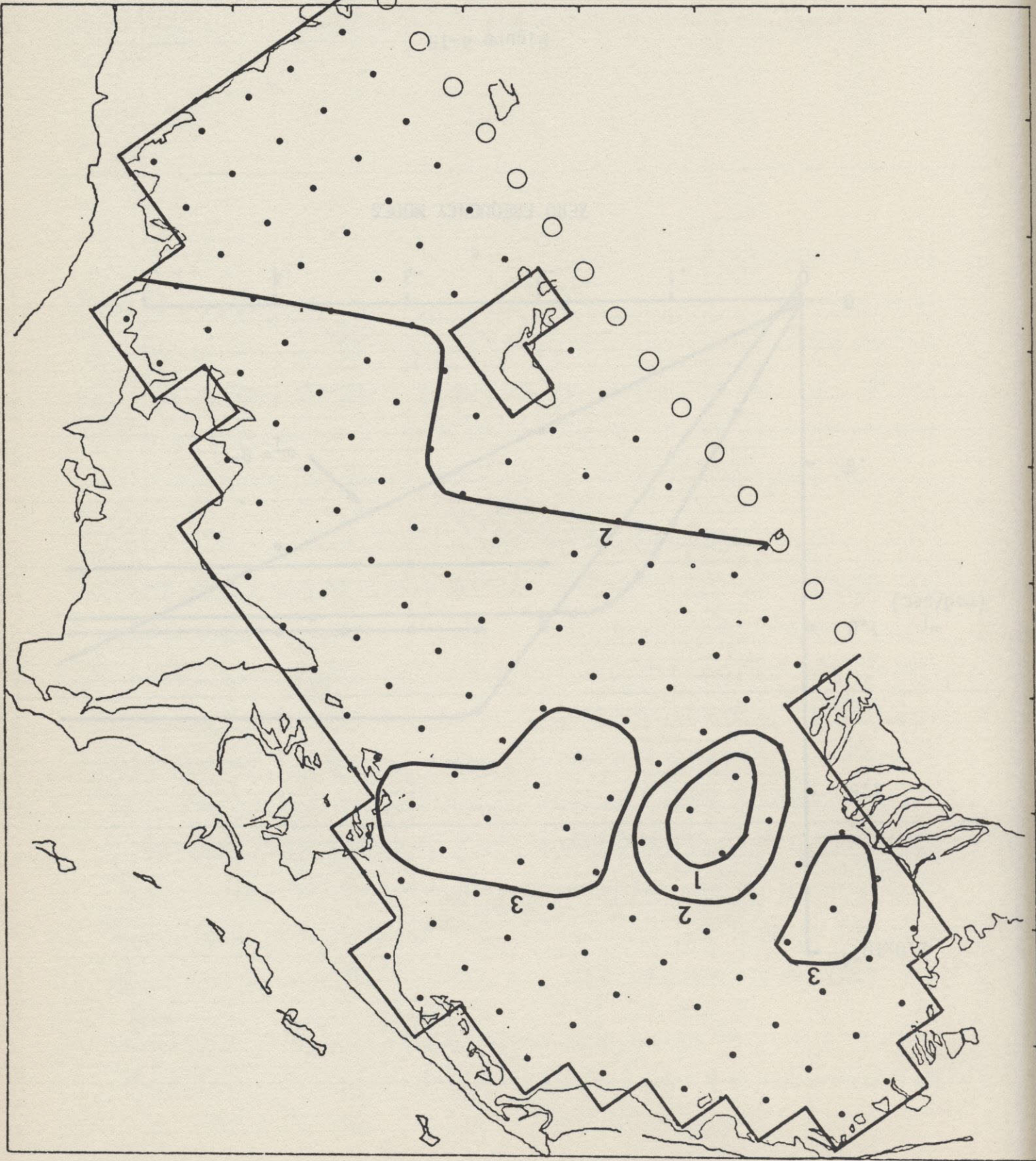


VELOCITIES FOR A QUASI-GEOSTROPHIC MODE $\omega \approx iR'$

Figure 4-13

Figure 4-14

ELEVATION CONTOURS FOR A
QUASI-GEOSTROPHIC MODE $\omega \approx 1R'$



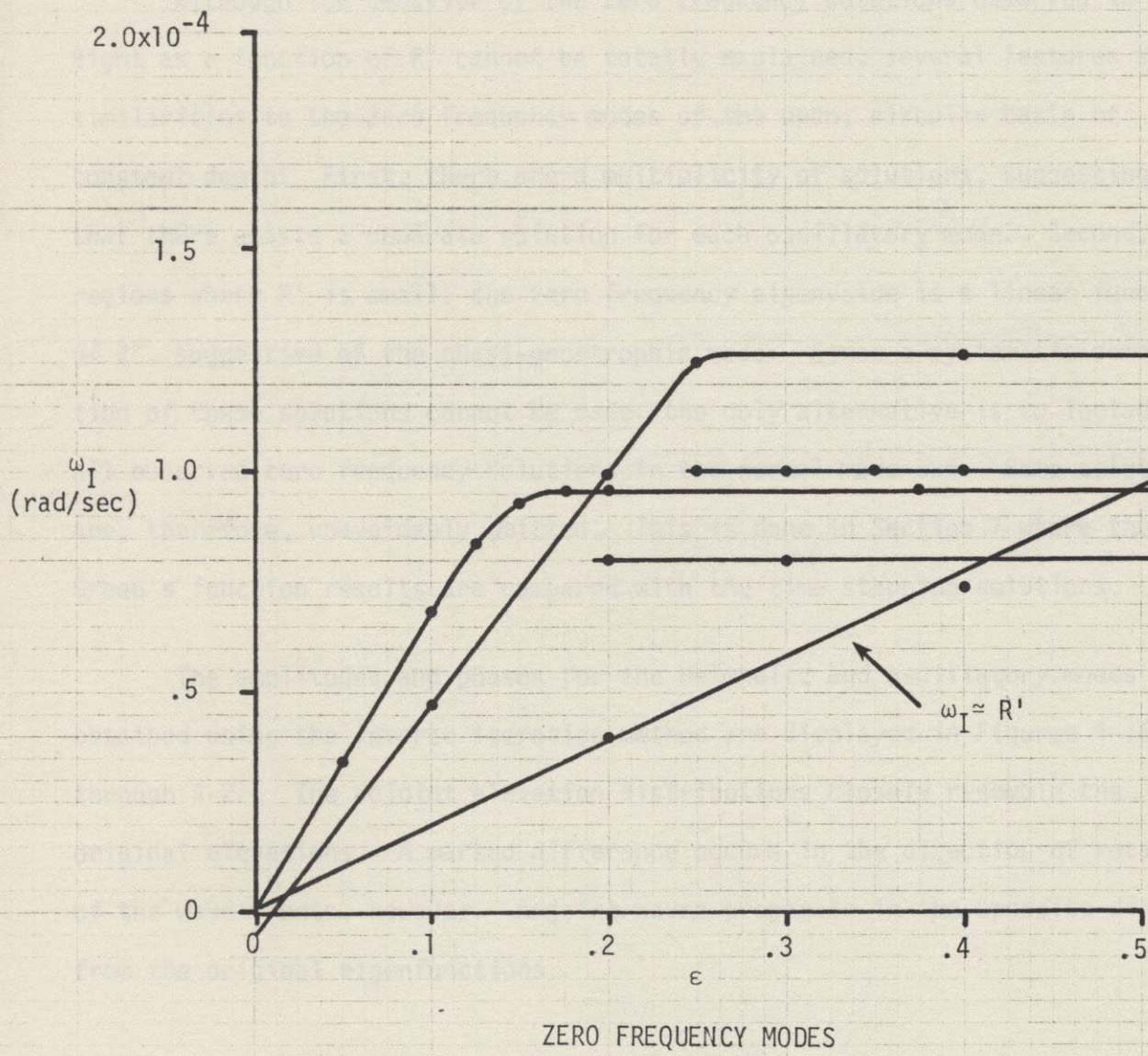


Figure 4-15

are characterized by a quasi-geostrophic-like behavior for small ϵ . At larger ϵ , however, ω_1 appears to be insensitive to the value of the friction.

Although the behavior of the zero frequency solutions observed in the Bight as a function of R' cannot be totally explained, several features show similarities to the zero frequency modes of the open, circular basin of constant depth. First, there are a multiplicity of solutions, suggesting that there exists a separate solution for each oscillatory mode. Second, in regions where R' is small, the zero frequency eigenvalue is a linear function of R' , suggestive of the quasi-geostrophic mode. Since a systematic compilation of these solutions cannot be made, the only alternative is to include all observed zero frequency solutions in the normal mode sum. Some solutions are, therefore, unavoidably omitted. This is done in Section 7 where the Green's function results are compared with the time stepping solutions.

The amplitudes and phases for the Helmholtz and oscillatory modes obtained using the inverse iteration method are displayed in Figures 4-16 through 4-27. The adjoint elevation distributions closely resemble the original elevations. A marked difference occurs in the direction of rotation of the wave fronts, however. Adjoint waves propagate in the opposite direction from the original eigenfunctions.

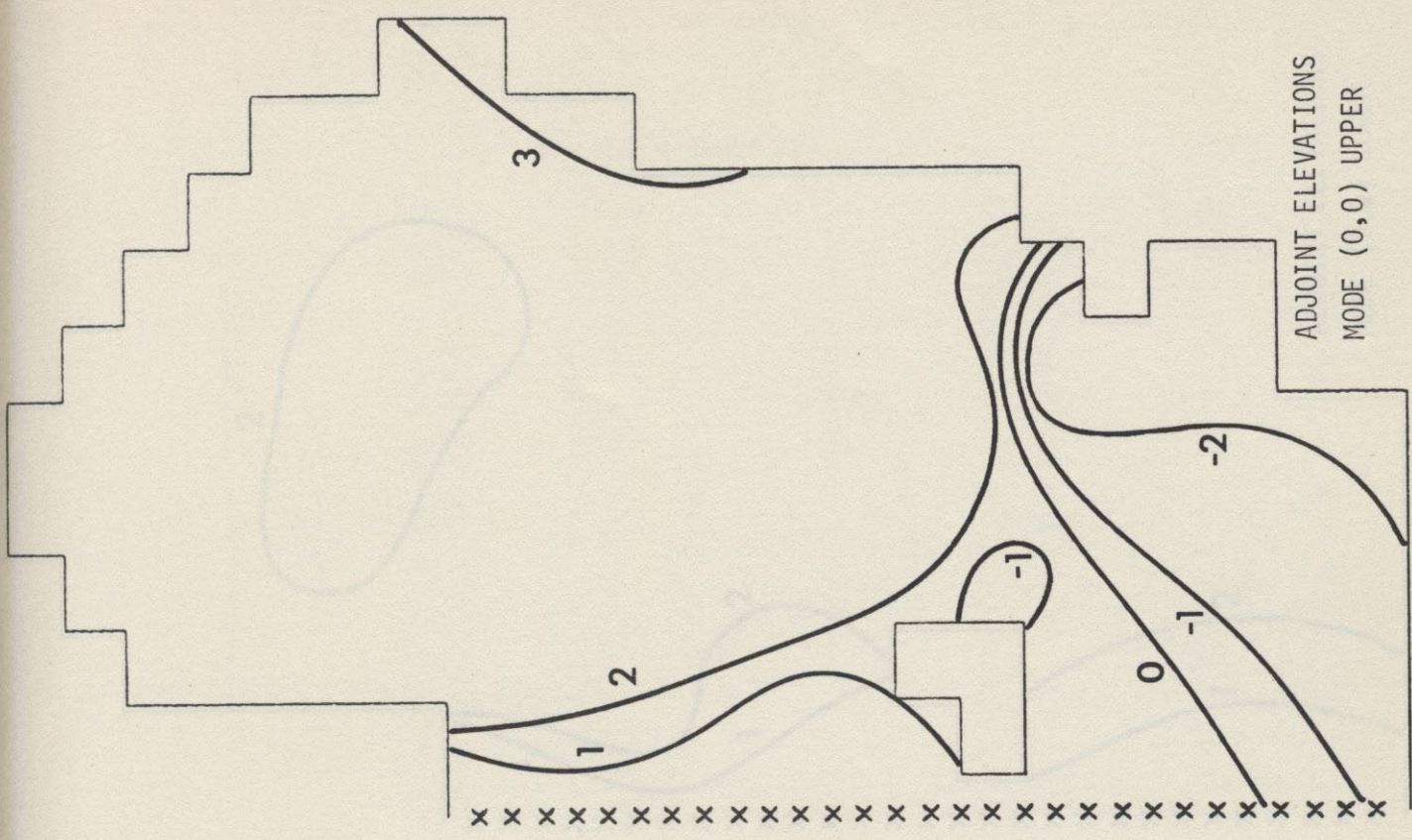
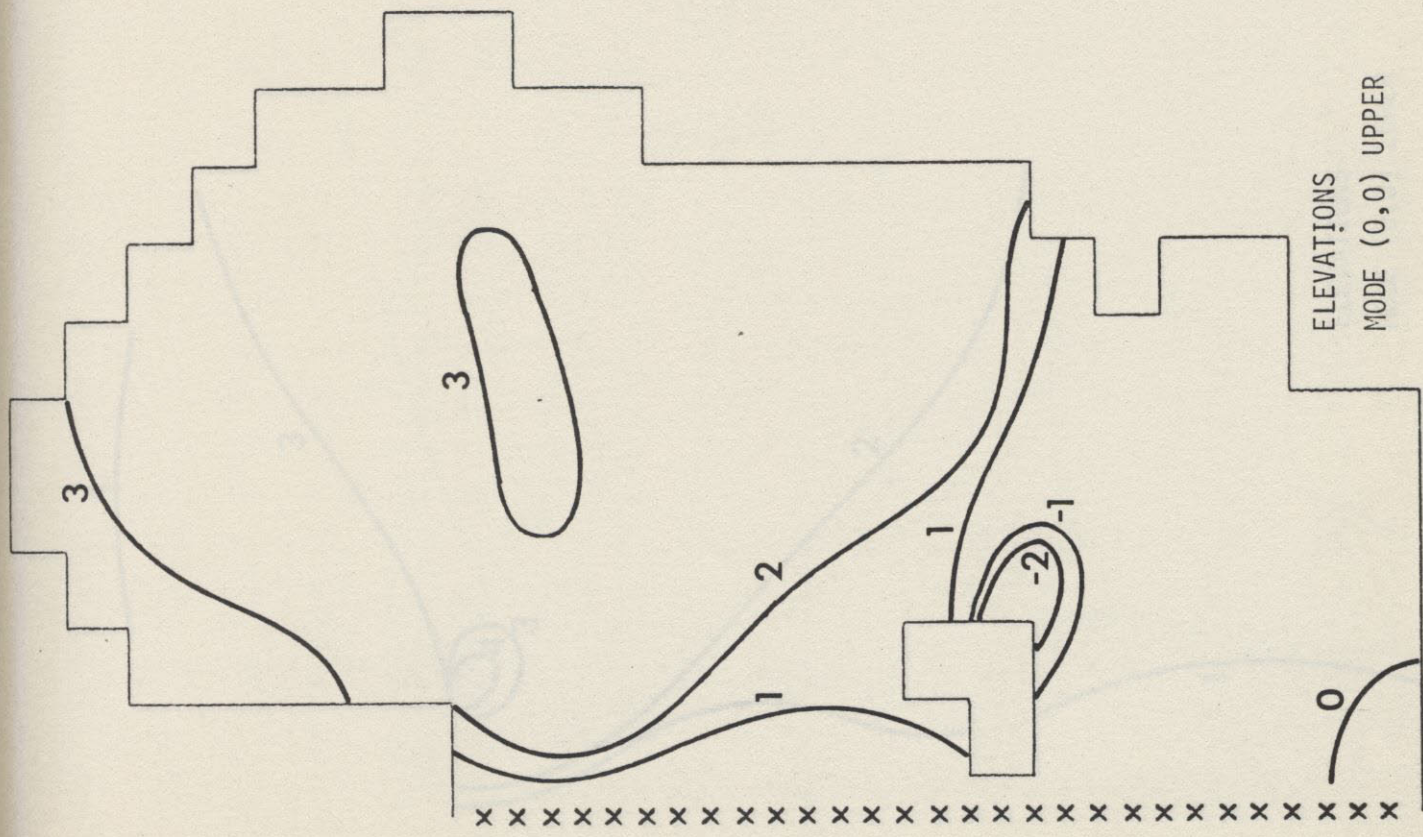


Figure 4-16

NSA/IR/P&A

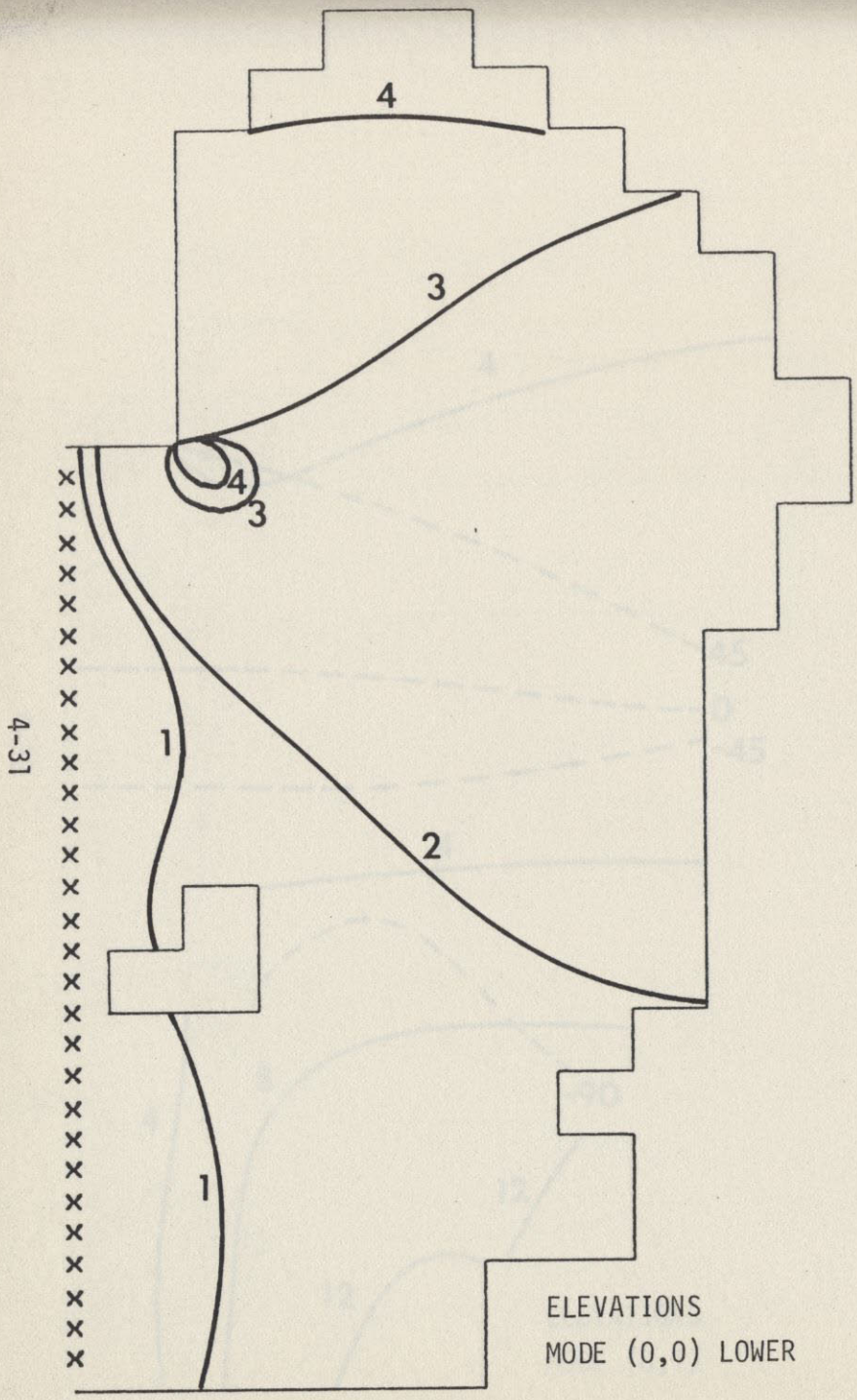


Figure 4-

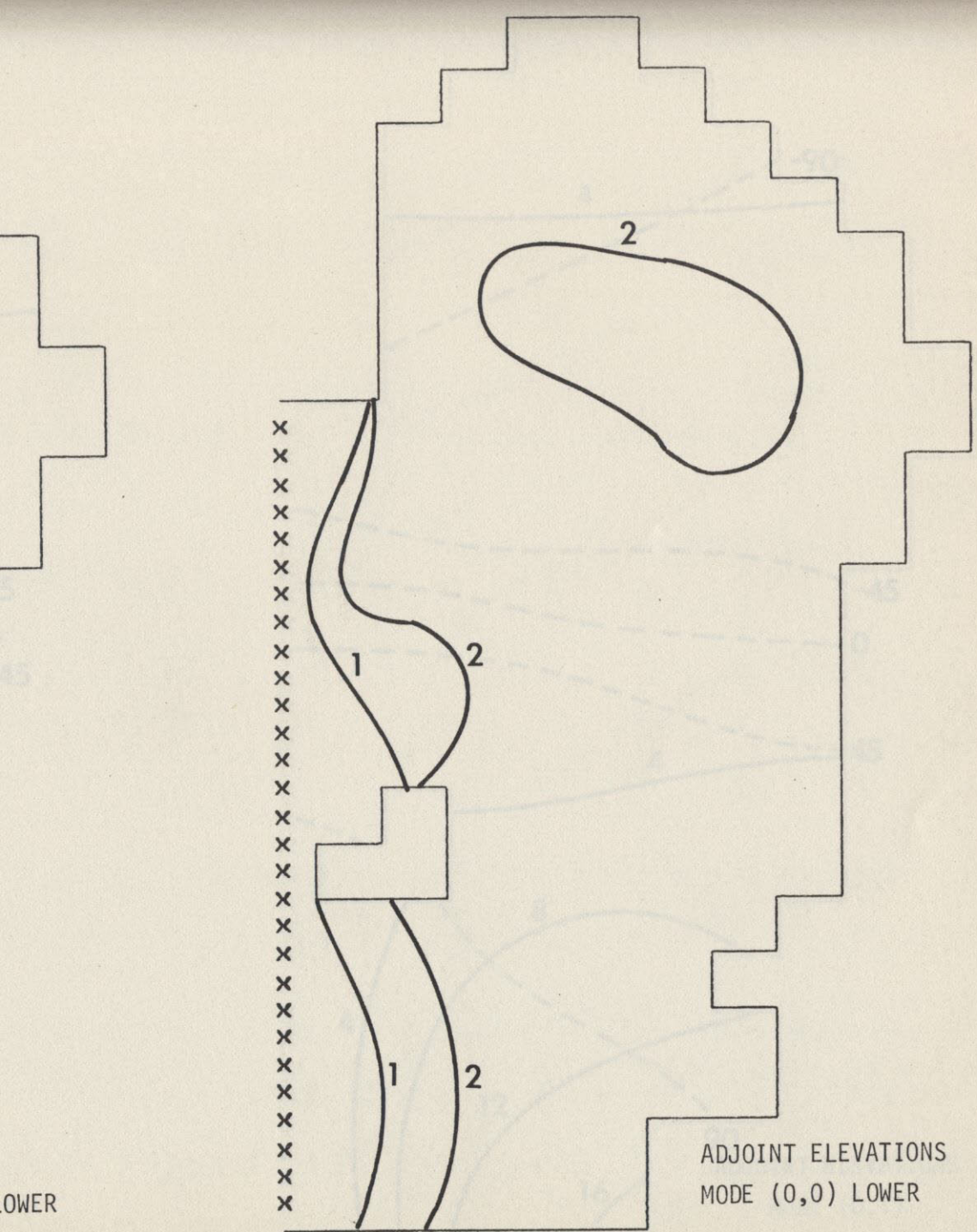


Figure 4-17

OWER

ADJOINT ELEVATIONS

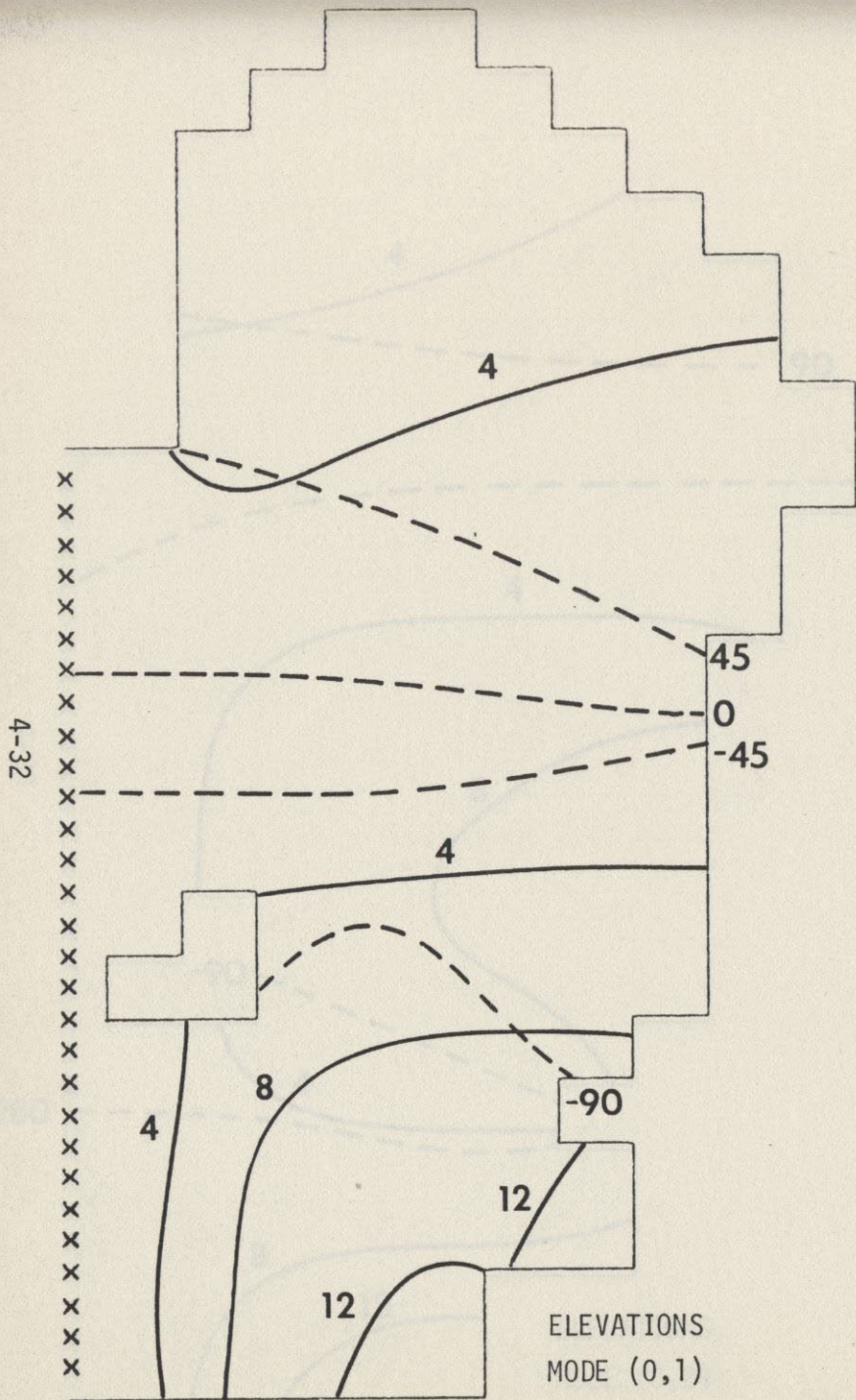


Figure 4-18

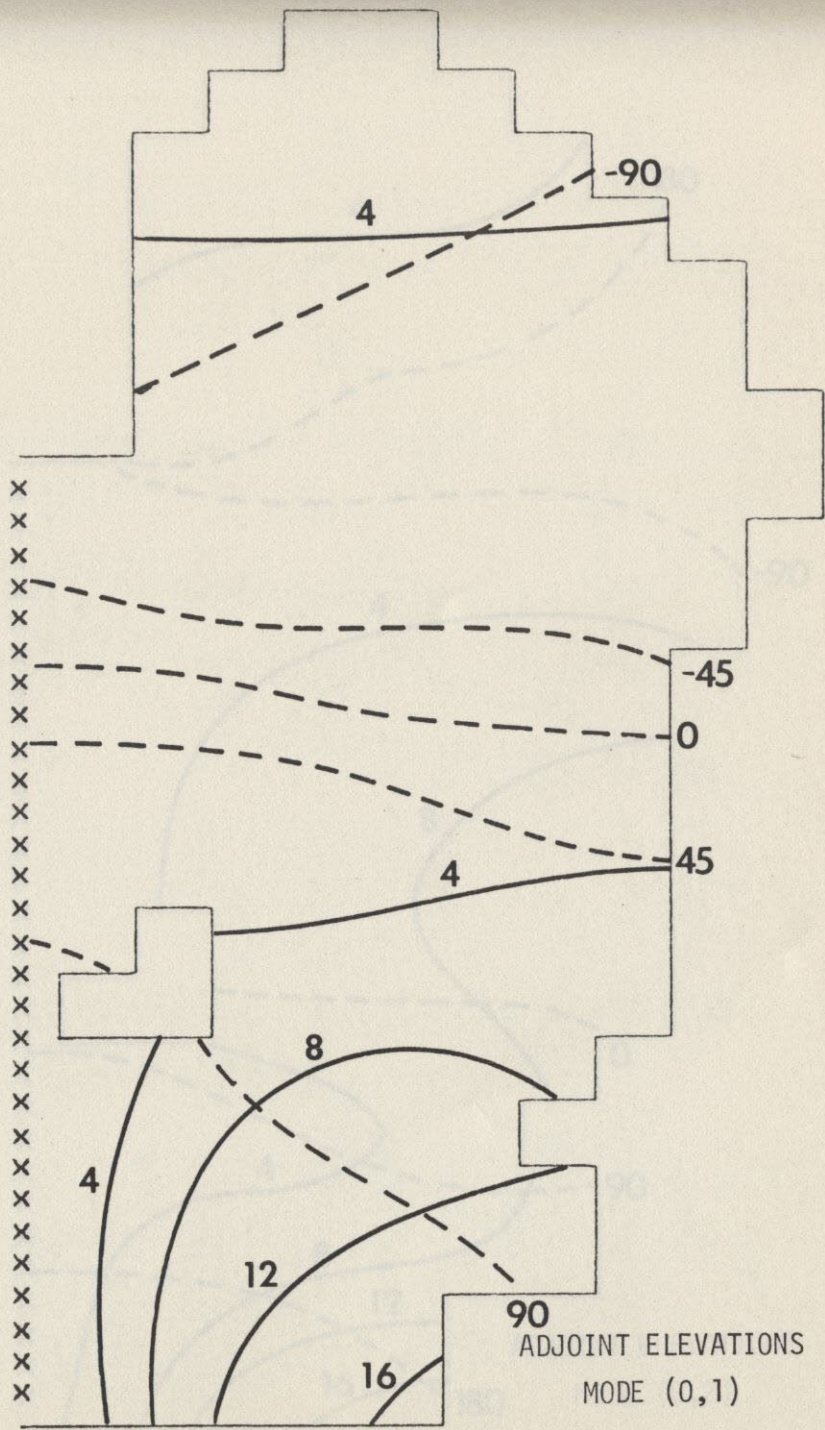


Figure 4-18

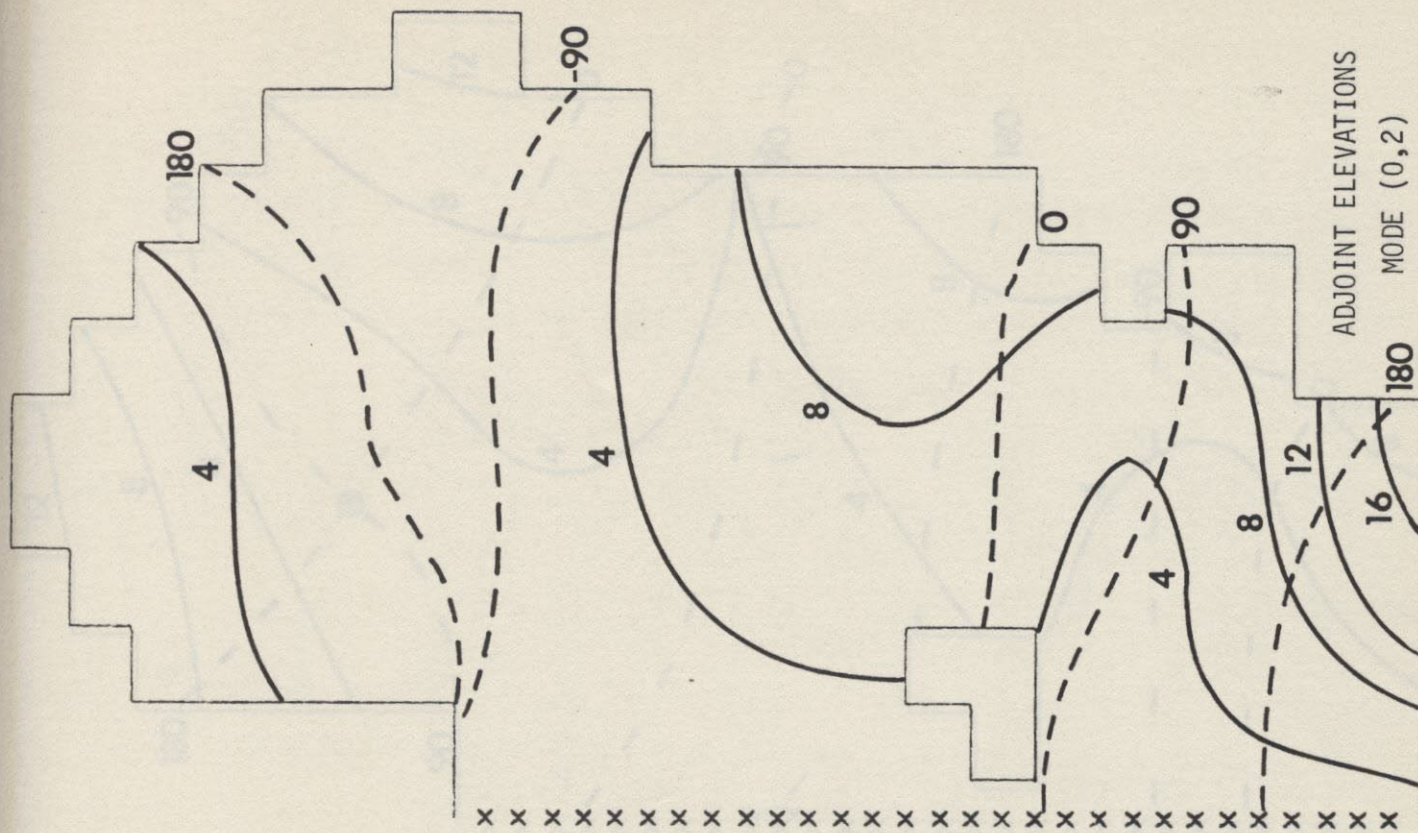
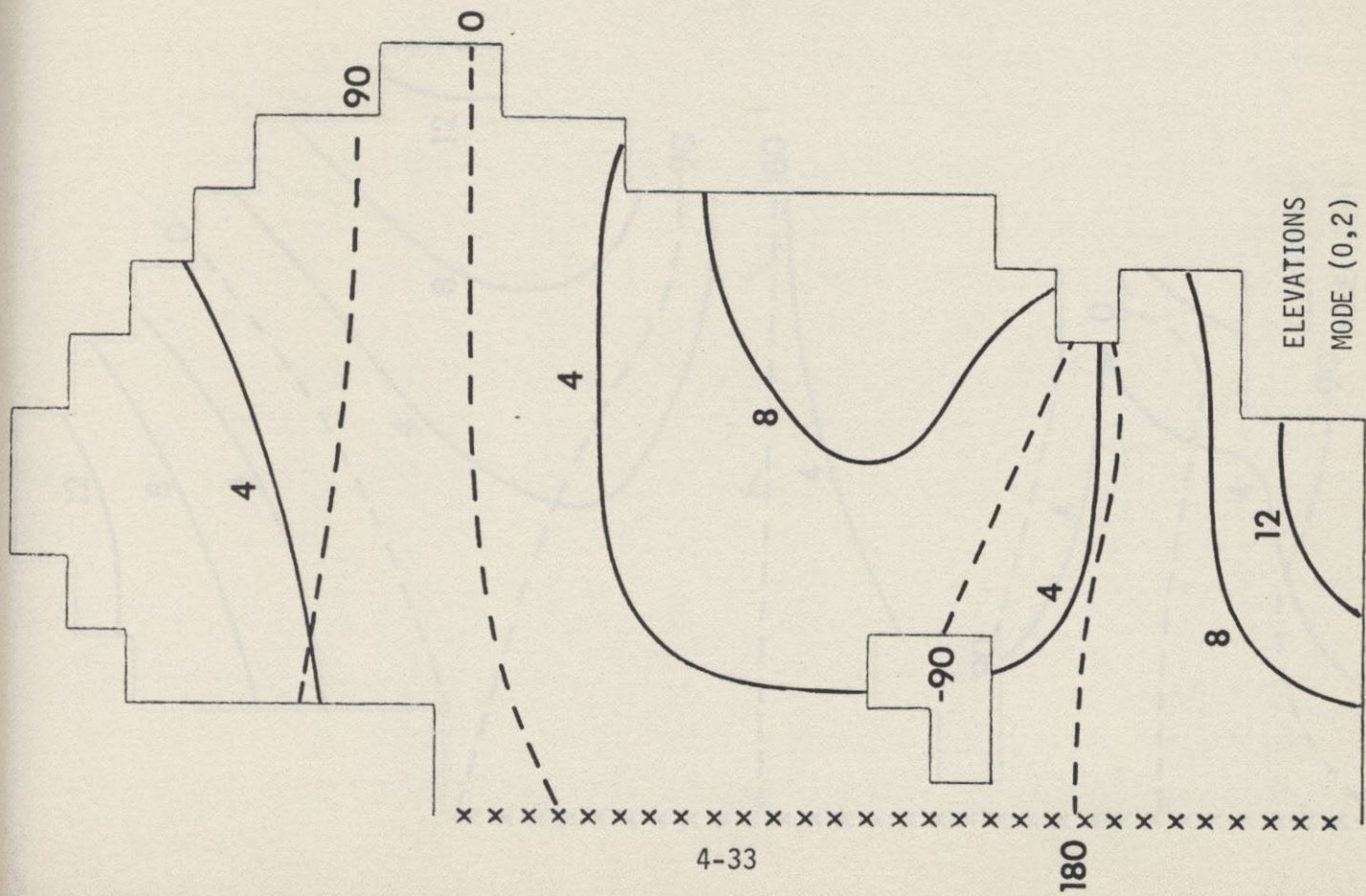


Figure 4-19

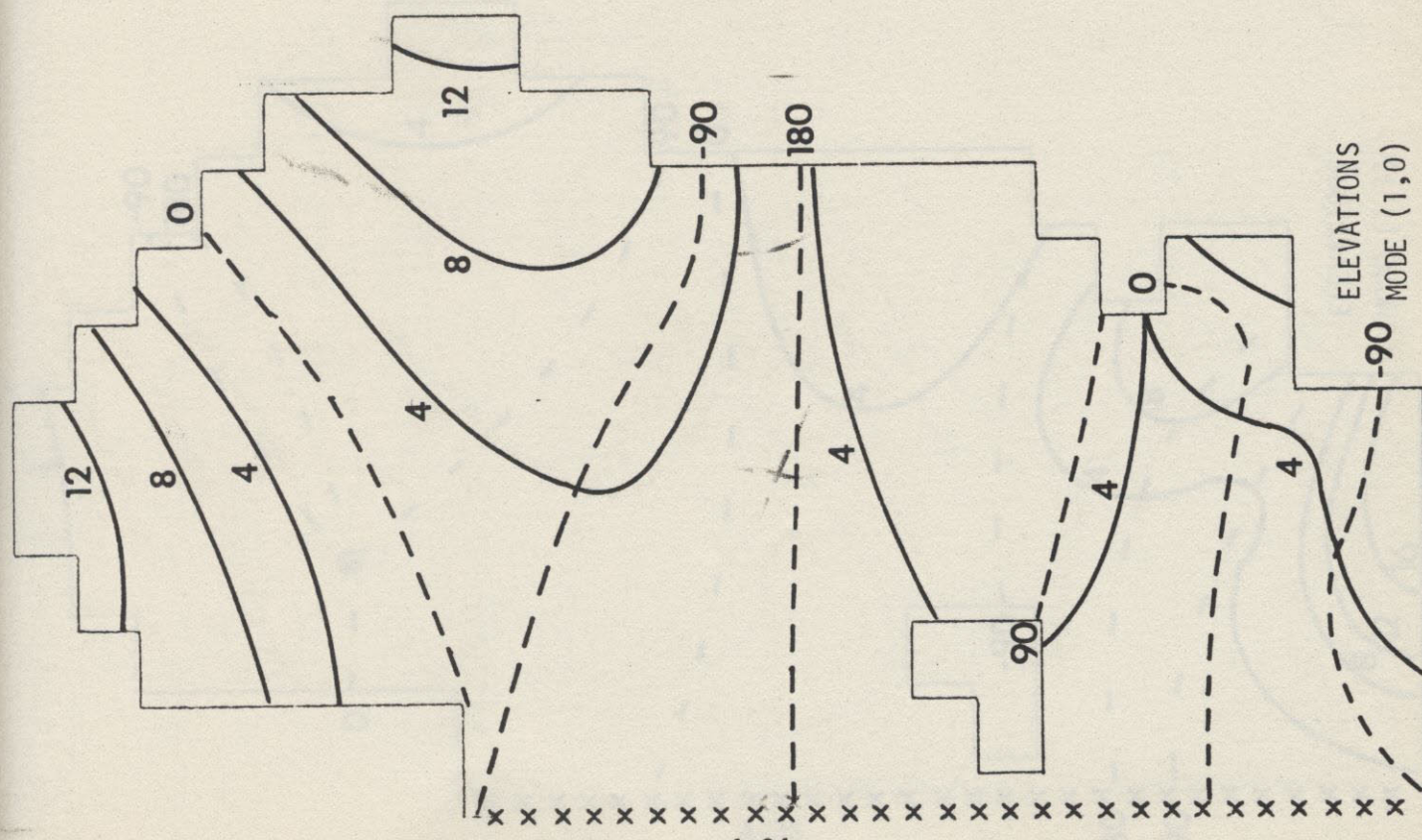
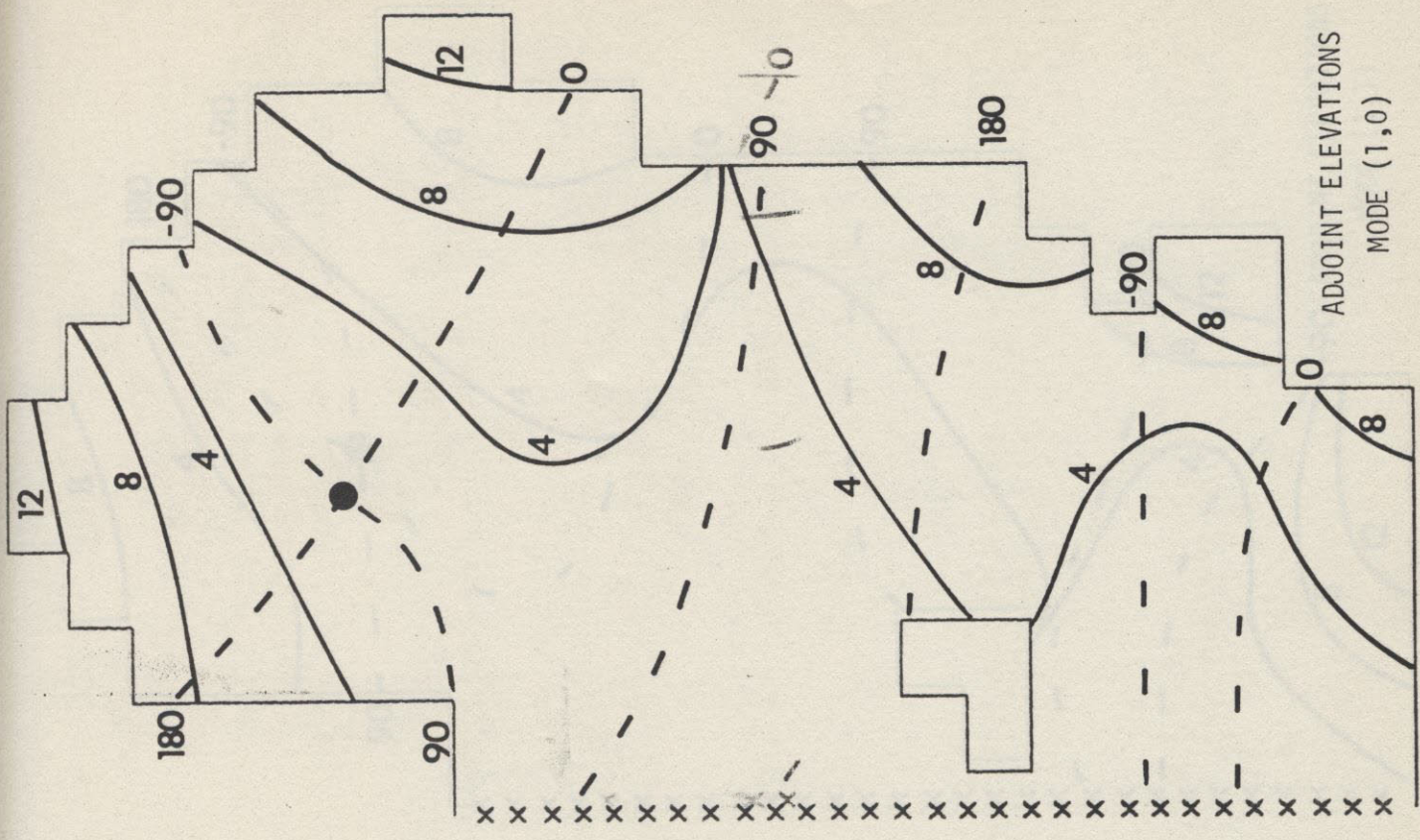


Figure 4-20

UNIVERSITY MICROFILMS

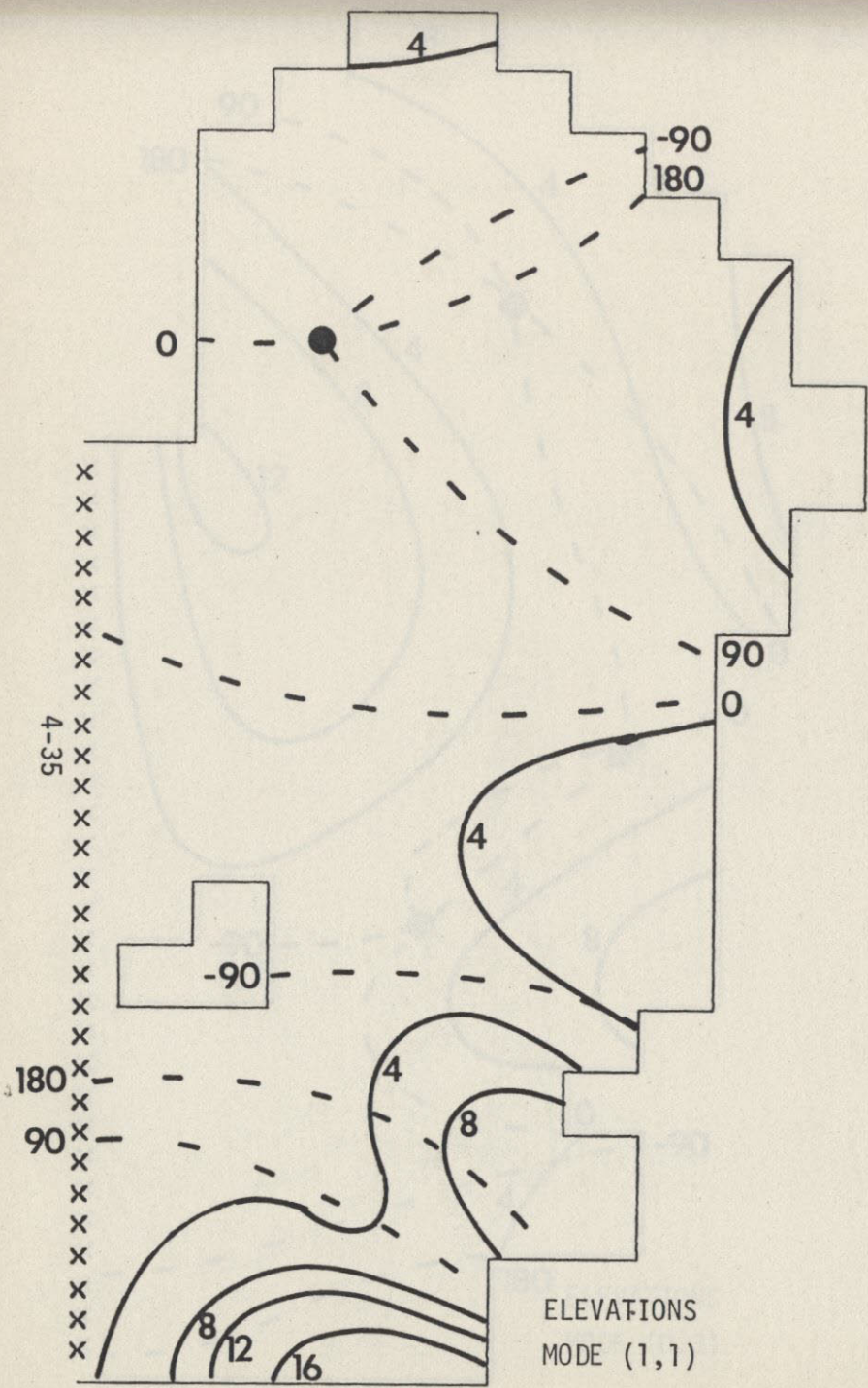


Figure 4-2

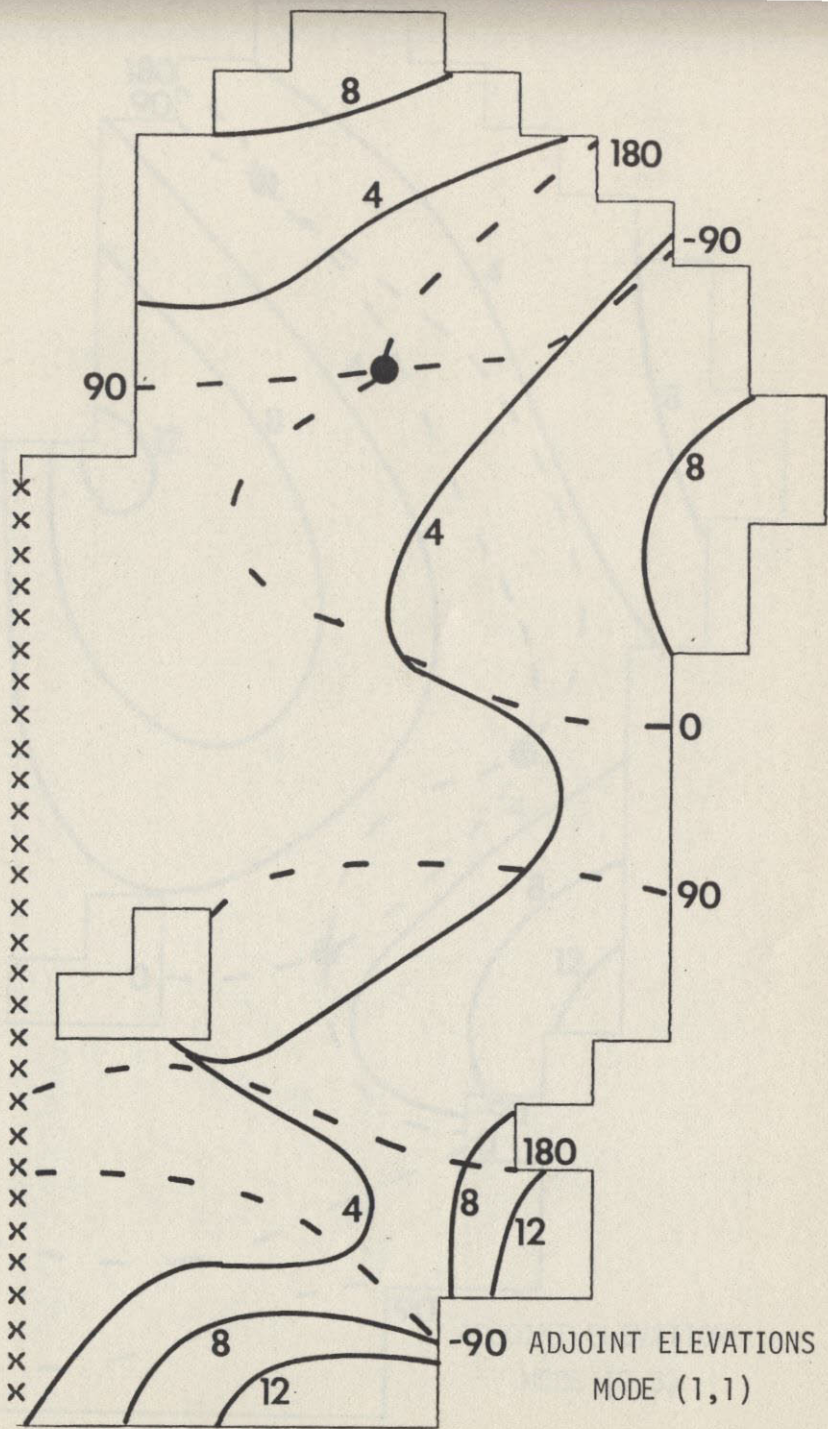


Figure 4-21

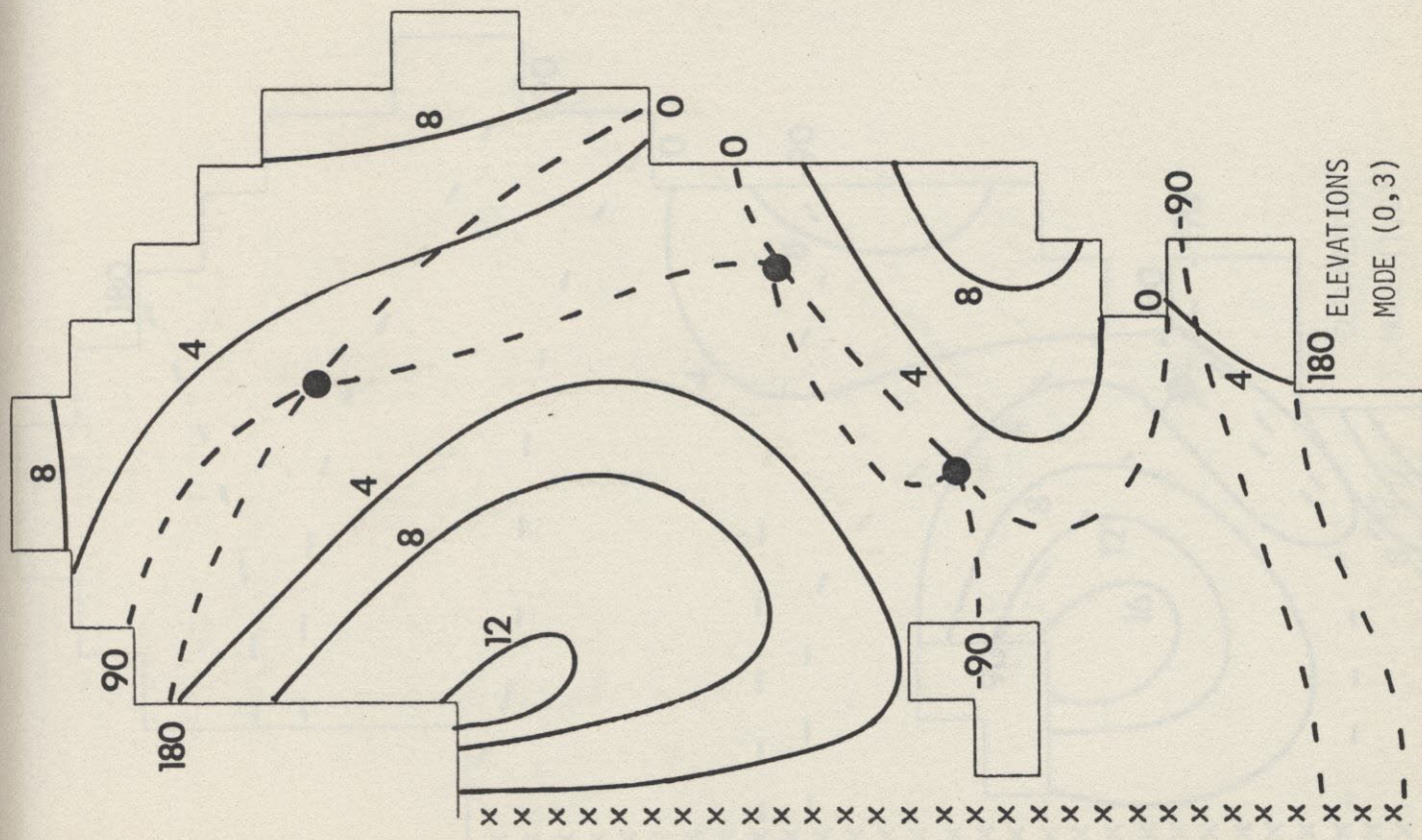
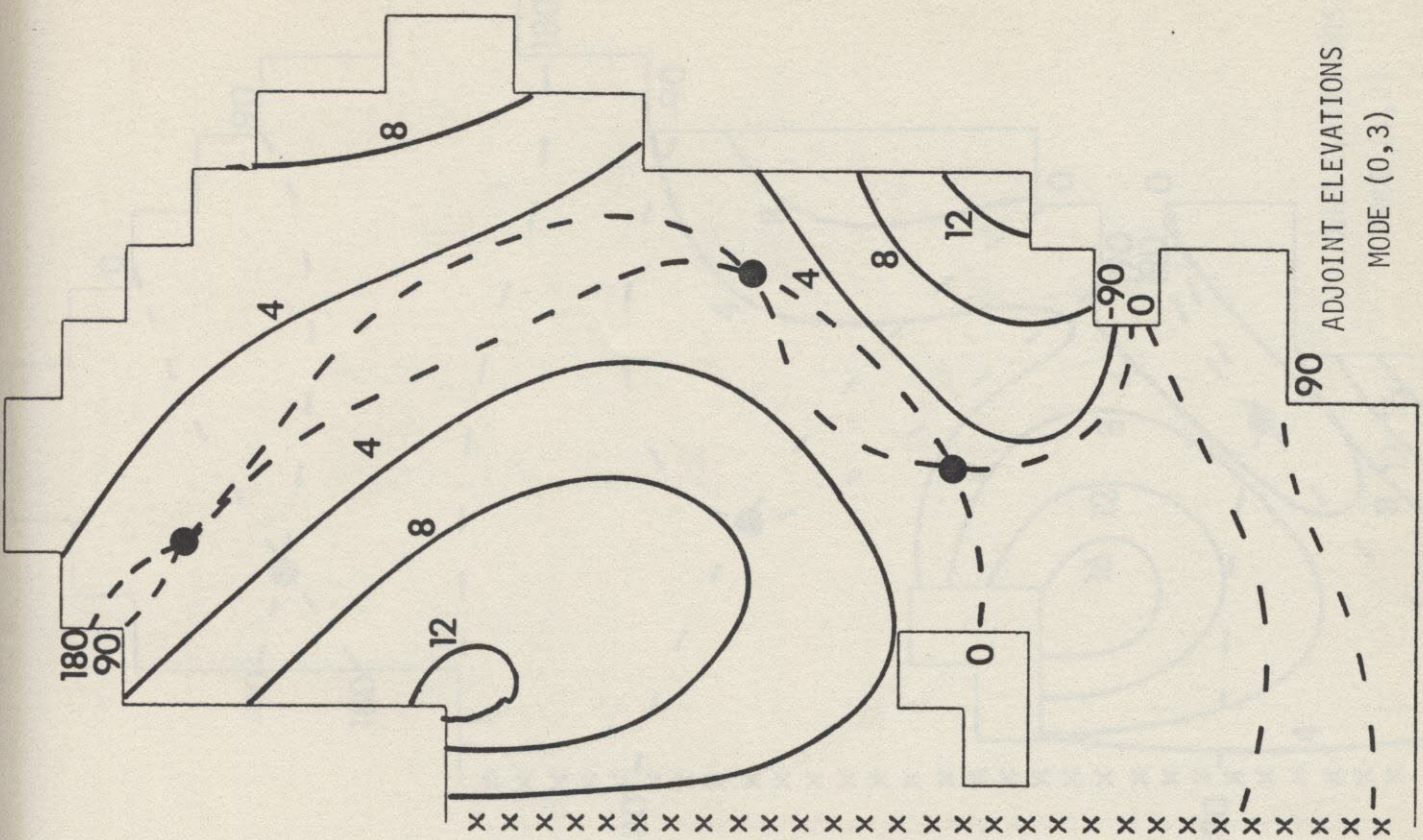
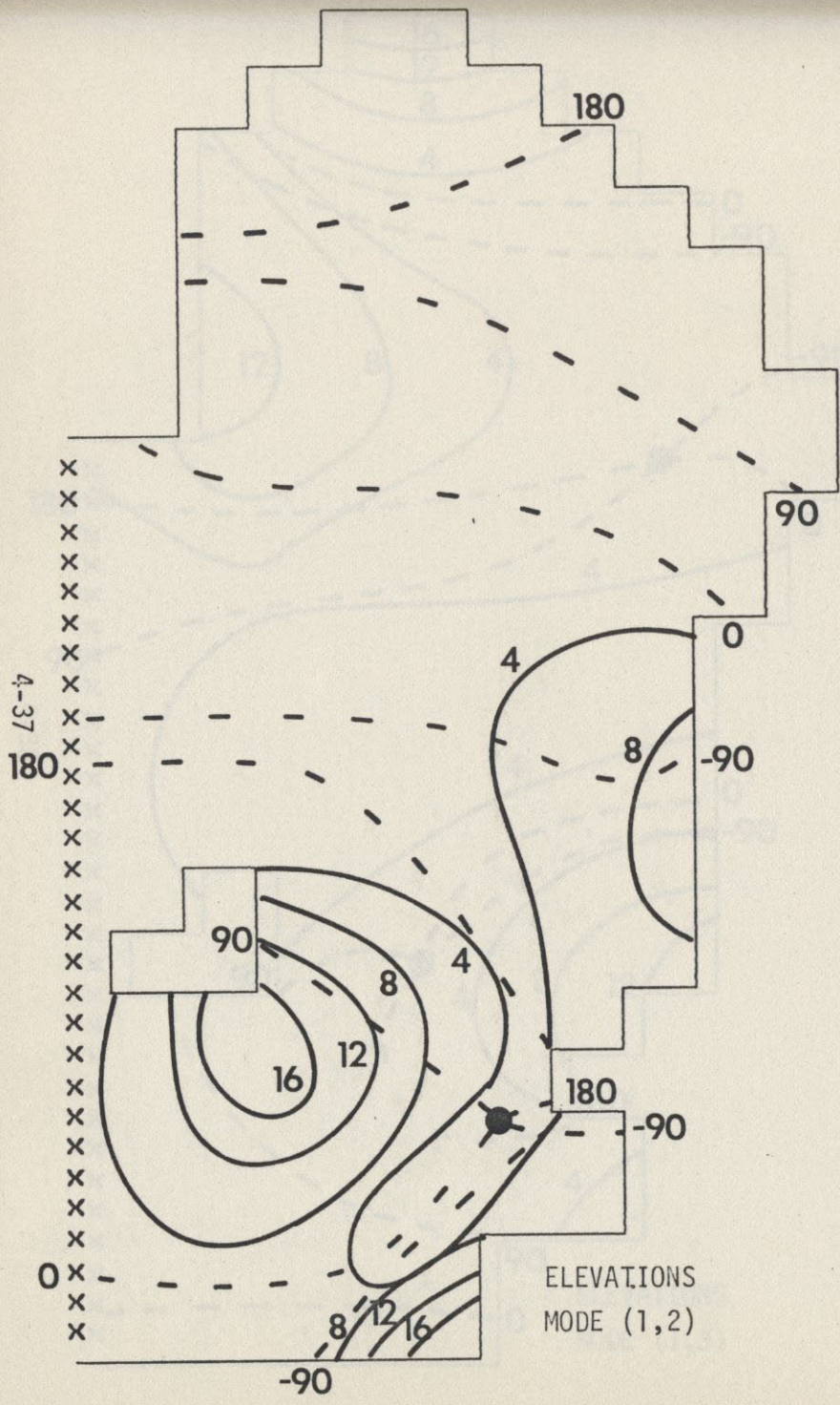


Figure 4-22

KRIEGER



Figure

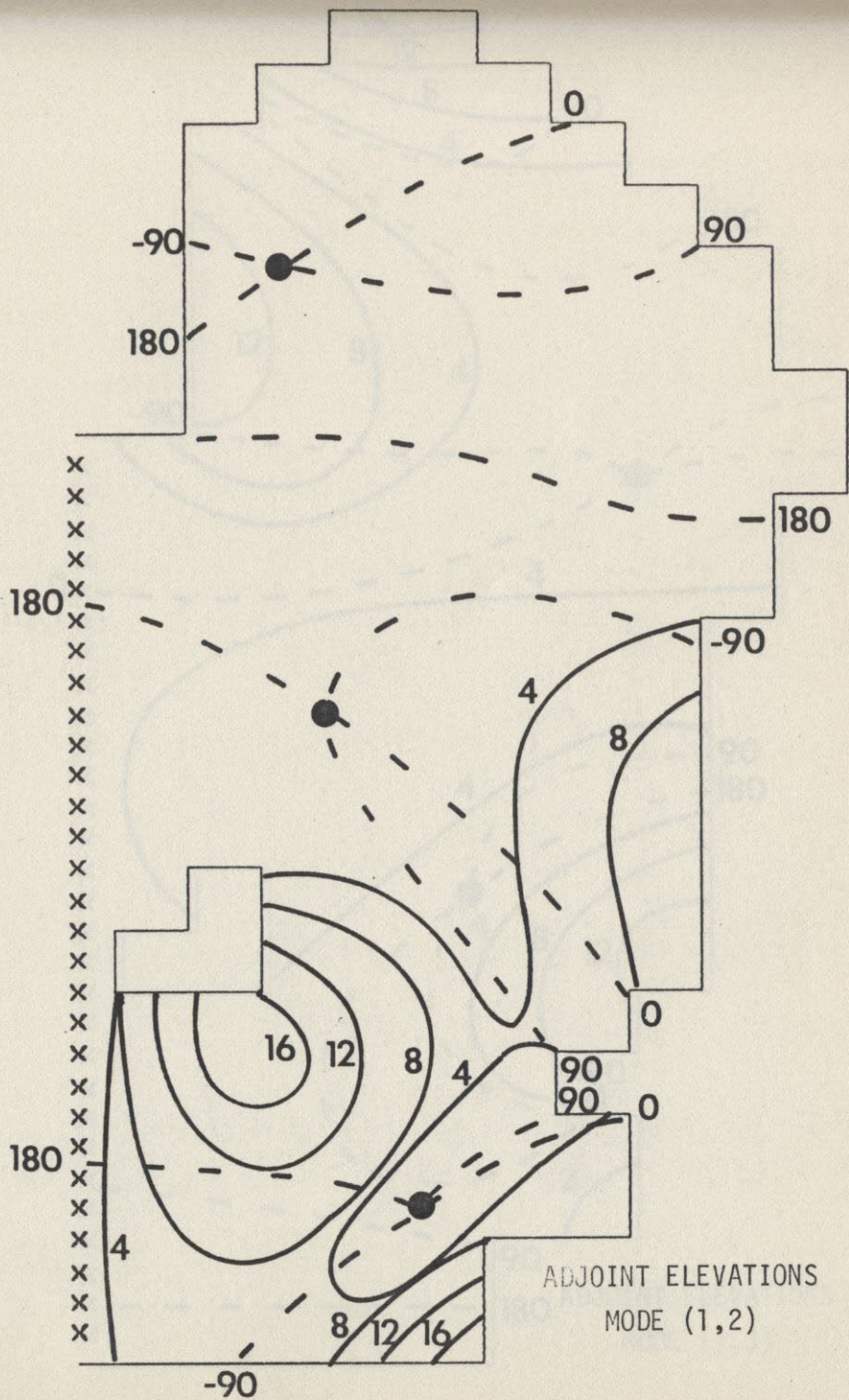


Figure 4-23

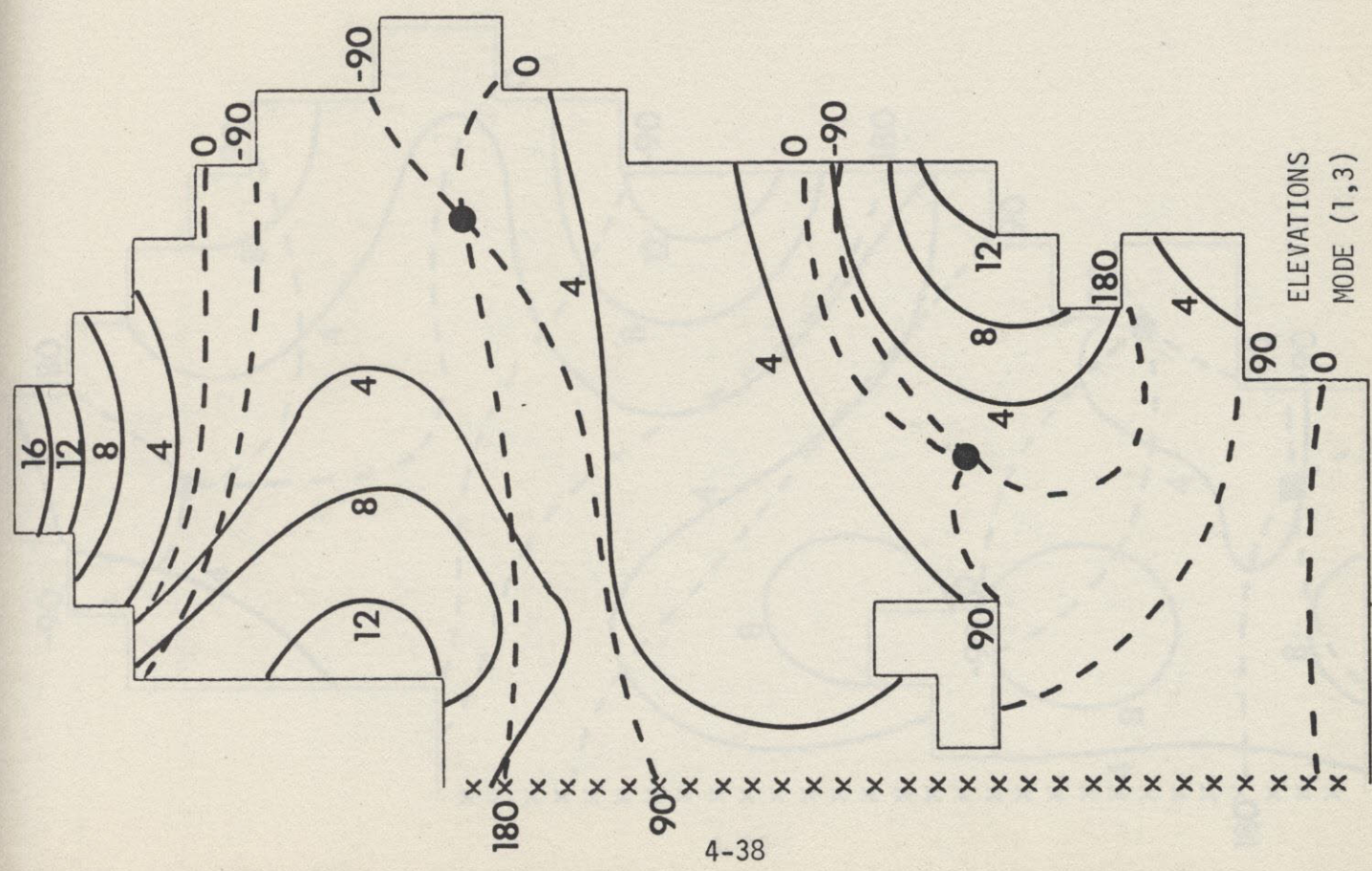
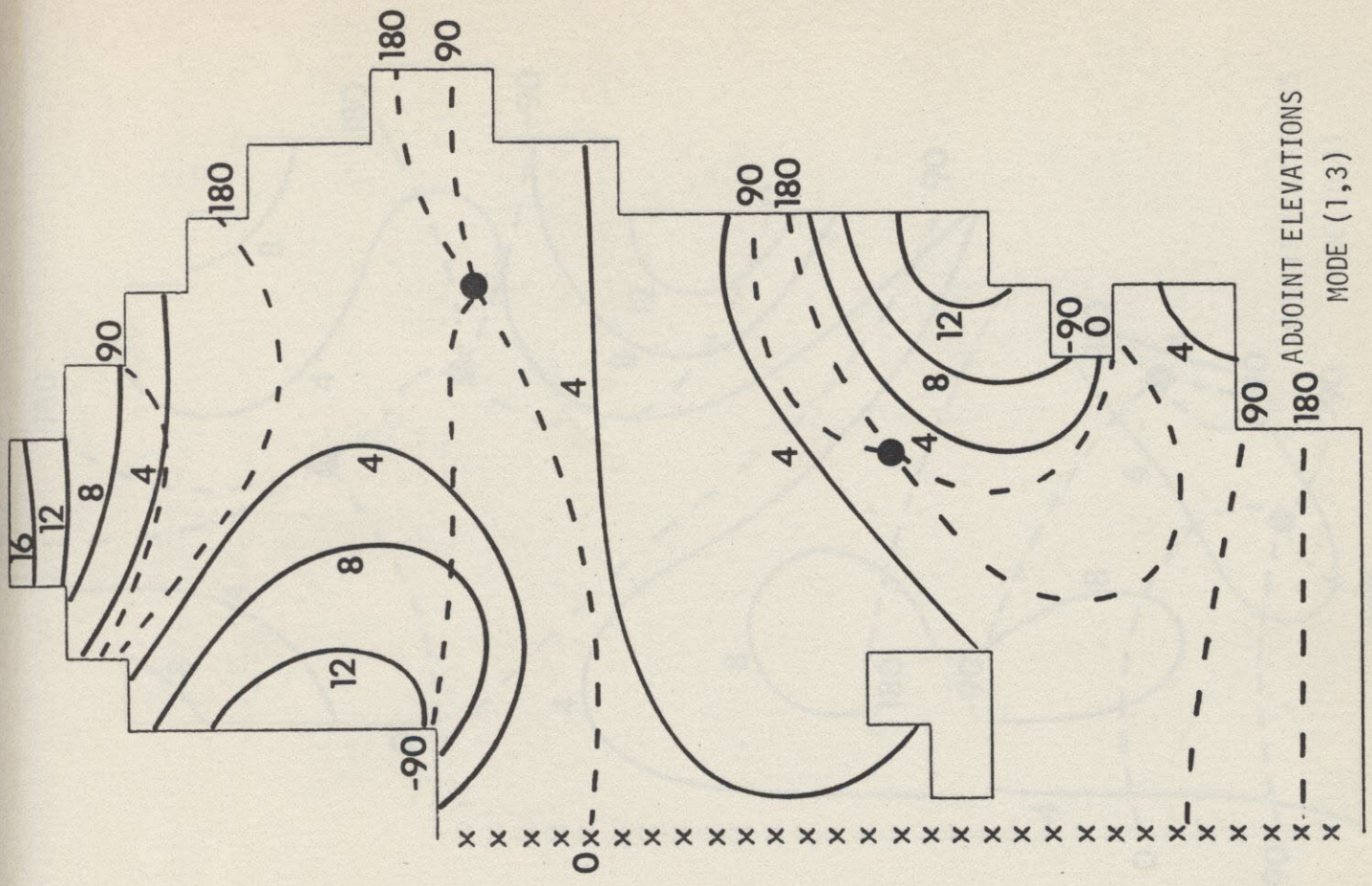


Figure 4-24

414790111214

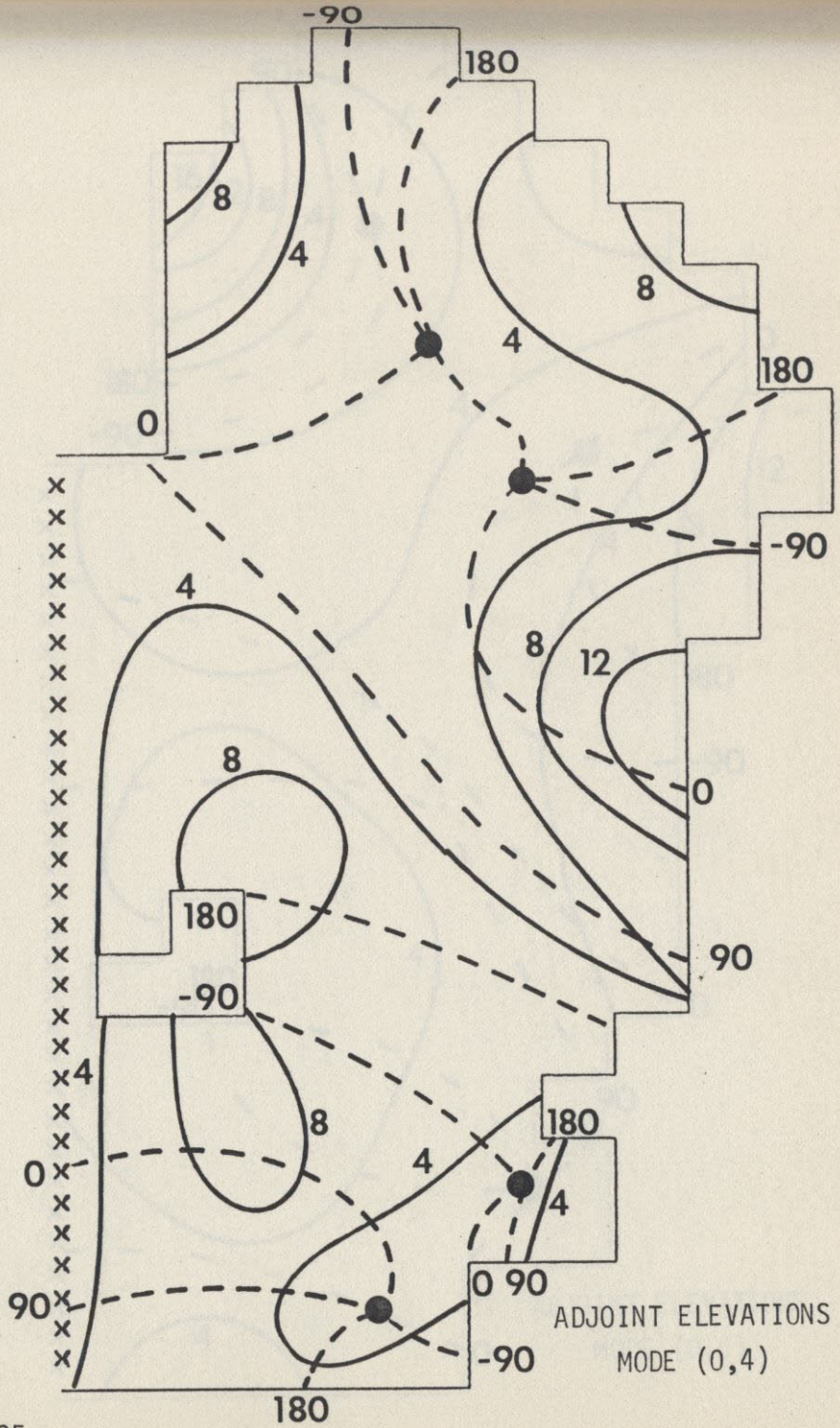


Figure 4-25

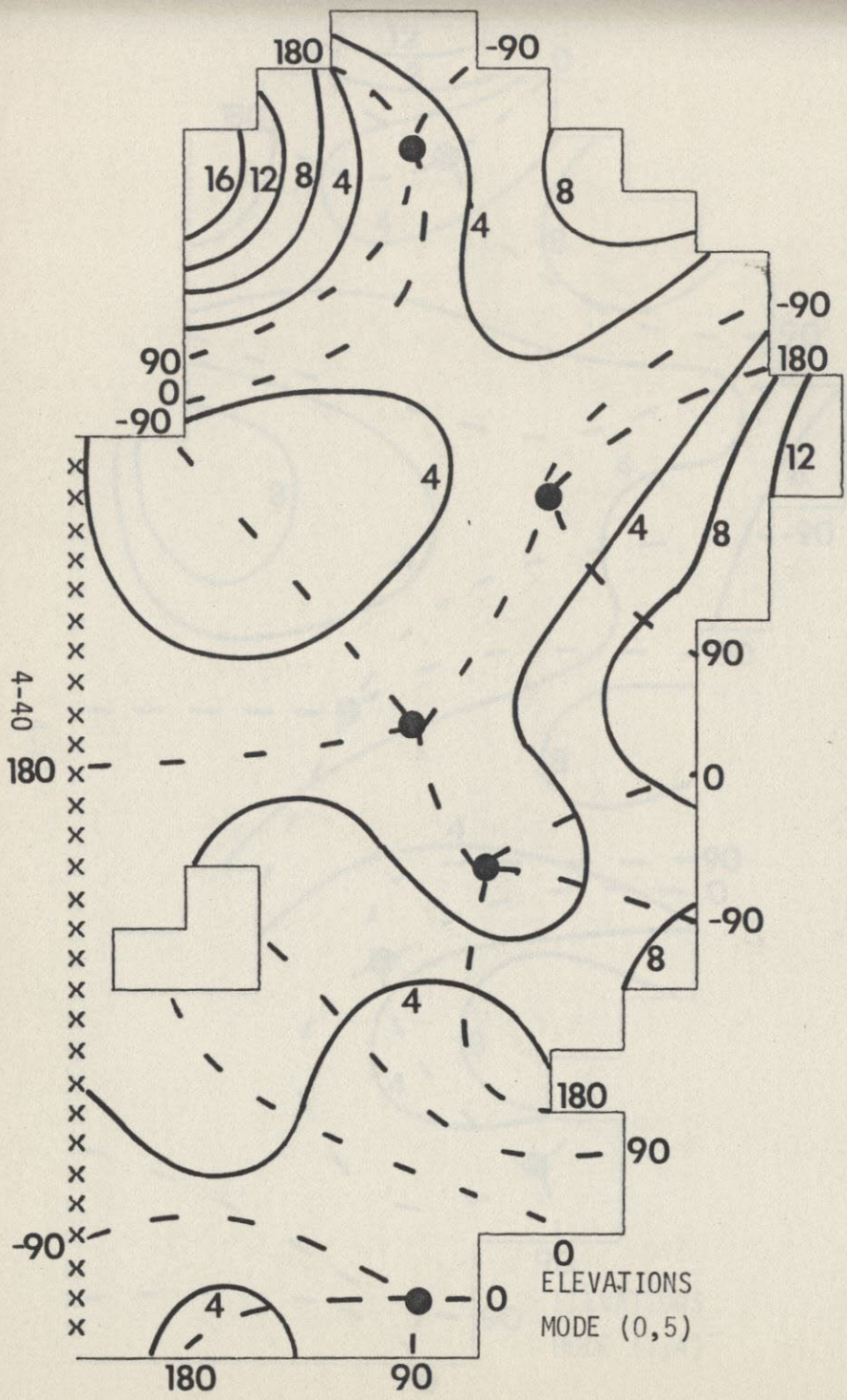


Figure 4-26

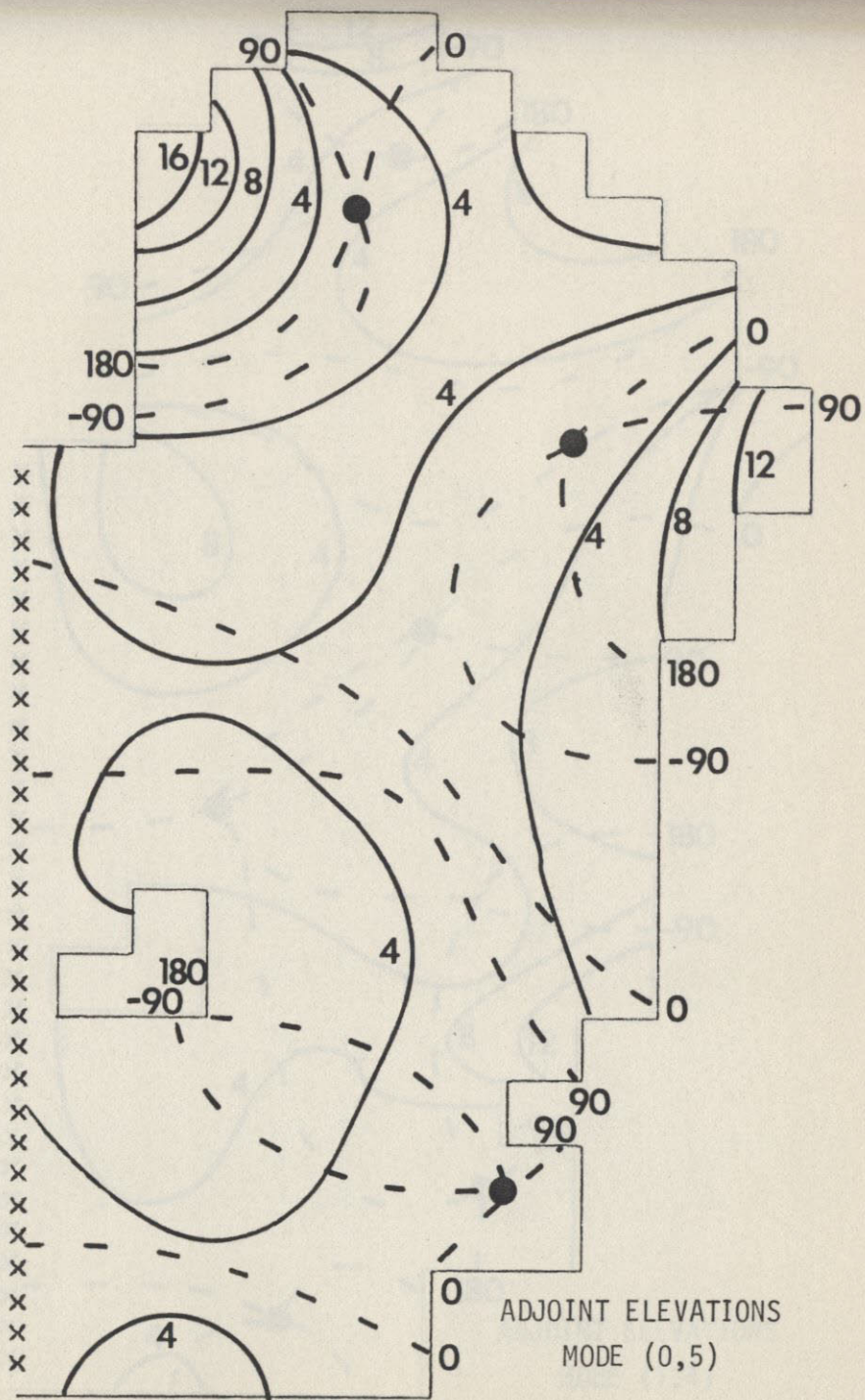


Figure 4-26

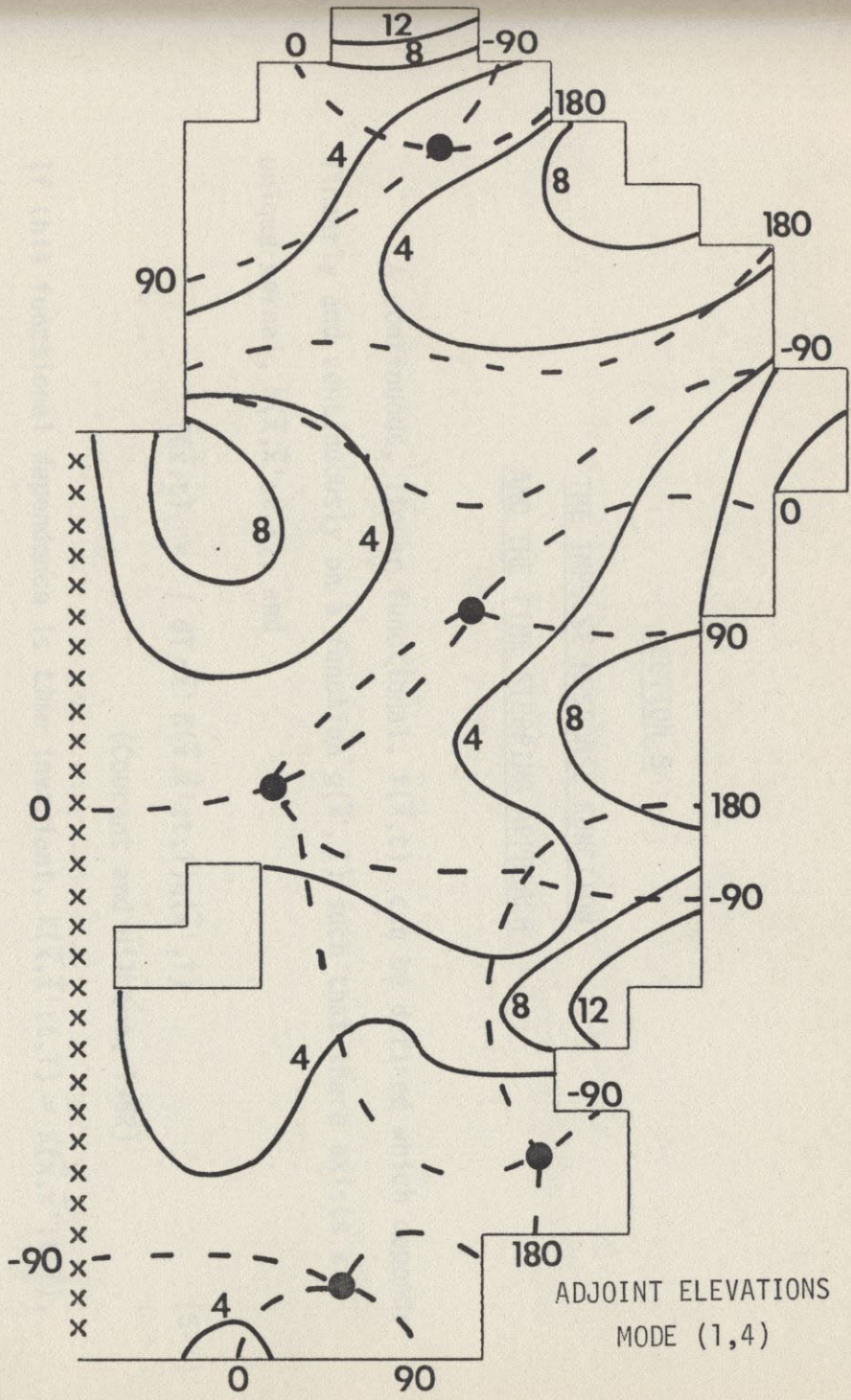


Figure 4-27

SECTION 5

THE IMPULSE RESPONSE FUNCTION AND THE TIME STEPPING APPROACH

A continuous, linear functional, $f(\vec{x}, t)$, can be defined which depends linearly and continuously on a function $g(\vec{x}', T)$ such that there exists a unique kernel, $K(\vec{x}, \vec{x}'; t, T)$, and

$$f(\vec{x}, t) = \int dT d\vec{x}' K(\vec{x}, \vec{x}'; t, T) g(\vec{x}', T) . \quad (5-1)$$

(Courant and Hilbert, 1962)

If this functional dependence is time invariant, $K(\vec{x}, \vec{x}'; t, T) = K(\vec{x}, \vec{x}'; t-T)$, and Eq. (5-1) can be rewritten,

$$f(\vec{x}, t) = \int dT d\vec{x}' K(\vec{x}, \vec{x}'; t-T) g(\vec{x}', T) . \quad (5-2)$$

Eq. (5-2) will be used below to obtain the response of a basin to a forcing, $g(\vec{x}', T)$.

The Bight of Abaco is forced, primarily, by surface winds and a surface boundary condition along the open boundary. These forcing functions, $\zeta_0(\vec{x}, t)$ and $\vec{\tau}(\vec{x}, t)$, are assumed to be homogeneous; that is,

$$\vec{\tau}(\vec{x}, t) = \vec{\tau}(t) \quad \text{and} \quad \zeta_0(\vec{x}, t) = \zeta_0(t) . \quad (5-3)$$

Homogeneity of $\vec{\tau}$ is justified on the grounds that the only energetically important frequencies occur at periods of 24 hours or greater. It is shown

in Section 6 that on 24 hour time scales the coherence of atmospheric signals is essentially one over the extent of the Bight. The homogeneity of $\zeta_0(\vec{x},t)$ is on less solid ground. Homogeneity along the boundary implies that either the external ocean wave arrives along the sill in constant phase, or that the synoptic scale of the atmospheric disturbance is large enough and gradual enough that the Northwest Providence Channel free surface rises and falls with constant phase everywhere. Since the energetically important changes in the wind direction and speed in February are due to frontal passages, the above conditions of large synoptic scales may well be justified. In the absence of evidence to the contrary, I will assume that sea surface forcing from outside is homogeneous.

$\zeta_0(\vec{x},t)$ also contains contributions from waves reflected from within the Bight. The amplitudes of such waves are likely to be small since there exists a shallow sill along the opening, and most of the wave energy impinging on the open boundary from within will be reflected due to the large depth discontinuity. Some energy will not, however, and this contribution is not expected to be homogeneous.

If we assume that the response, $\zeta(\vec{x},t)$, of the Bight is linearly related to the assumed homogeneous forcing functions, $\zeta_0(t)$ and $\vec{\tau}(t)$, Eq. (5-2) becomes:

$$\begin{aligned} \zeta(\vec{x},t) = & \int dT K_{\zeta_0}(\vec{x};t-T)\zeta_0(T) \\ & + \int dT K_{\vec{\tau}}(\vec{x};t-T)\vec{\tau}(T) \quad . \end{aligned} \quad (5-4)$$

The problem of solving for $\zeta(\vec{x}, t)$ becomes a problem of determining the kernals, K_{ζ_0} and $K_{\vec{\tau}}$.

We partition $\zeta(\vec{x}, t)$,

$$\zeta(\vec{x}, t) = \zeta_{\zeta_0}(\vec{x}, t) + \zeta_{\vec{\tau}}(\vec{x}, t) \quad , \quad (5-5)$$

where

$$\zeta_{\zeta_0}(\vec{x}, t) = \int dT K_{\zeta_0}(\vec{x}; t-T) \zeta_0(T) \quad (5-6)$$

and

$$\zeta_{\vec{\tau}}(\vec{x}, t) = \int dT K_{\vec{\tau}}(\vec{x}; t-T) \vec{\tau}(T) \quad . \quad (5-7)$$

The kernals, K_{ζ_0} and $K_{\vec{\tau}}$, are the responses to impulse forcing in ζ_0 and $\vec{\tau}$ as can be seen by substituting $\zeta_0(t) = \delta(t)$ and $\vec{\tau}(t) = \delta(t)$:

$$\zeta_{\zeta_0}(\vec{x}, t) = \int dT K_{\zeta_0}(\vec{x}; t-T) \zeta_0(T) = K_{\zeta_0}(\vec{x}; t) \quad (5-8)$$

$$\zeta_{\vec{\tau}}(\vec{x}, t) = \int dT K_{\vec{\tau}}(\vec{x}; t-T) \delta(T) = K_{\vec{\tau}}(\vec{x}; t) \quad . \quad (5-9)$$

Hence, the kernals are commonly known as impulse response functions and could be obtained by calculating $\zeta_{\zeta_0}(\vec{x}, t)$ and $\zeta_{\vec{\tau}}(\vec{x}, t)$ using a time stepping scheme.

However, step functions can be defined with more precision, numerically, than can delta functions since the discretized delta function must be a square pulse approximation. The response to a step function is merely the integral of the impulse response function as is shown below.

$$\text{Let } \Gamma(t) = \begin{cases} 0 & t < 0 \\ 1 & t \geq 0 \end{cases} \quad (5-10)$$

be a unit step function so that,

$$\zeta^\Gamma(\vec{x}, t) = \int_{-\infty}^{\infty} dT K(\vec{x}; t-T) \Gamma(T) = \int_0^{\infty} dT K(\vec{x}; t-T) \quad (5-11)$$

Substitute the change of variable, $T' = t-T$.

$$\text{Then, } \zeta^\Gamma(\vec{x}, t) = \int_{-\infty}^t dT' K(\vec{x}; T') \quad (5-12)$$

Taking the time derivative of both sides,

$$\frac{\partial \zeta^\Gamma(\vec{x}, t)}{\partial t} = K(\vec{x}; t) \quad (5-13)$$

i.e., $K(\vec{x}; t)$, the impulse response function, can be obtained by taking the time derivative of the step response function. $\lim_{t \rightarrow \infty} \zeta^\Gamma(\vec{x}, t)$ describes the response of the surface at zero frequency.

The velocity field components of the step response function (the response function is in fact a vector, $\begin{pmatrix} \vec{u}^\Gamma(\vec{x}, t) \\ \zeta^\Gamma(\vec{x}, t) \end{pmatrix}$) are stored along with the elevations during the time stepping since the velocity fields form an important feature of the zero frequency response.

$\zeta^\Gamma(t)$ is obtained using a time stepping method common to most storm surge calculations (Sielecki, 1968). A time step of one minute is used. The Friedrich-Lewy-Courant stability criterion,

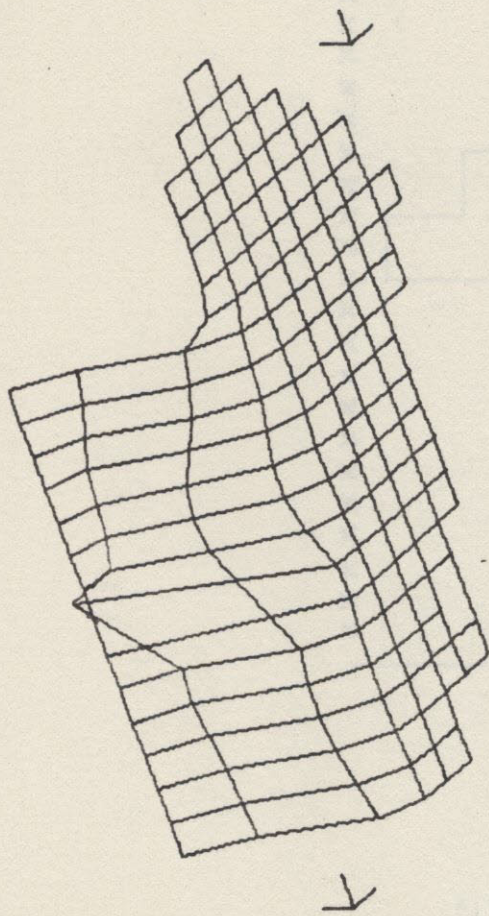
$$\Delta t \leq \sqrt{2} \Delta s / \sqrt{gh} \quad (5-14)$$

requires that $\Delta t < 680$ seconds. The criterion is easily satisfied.

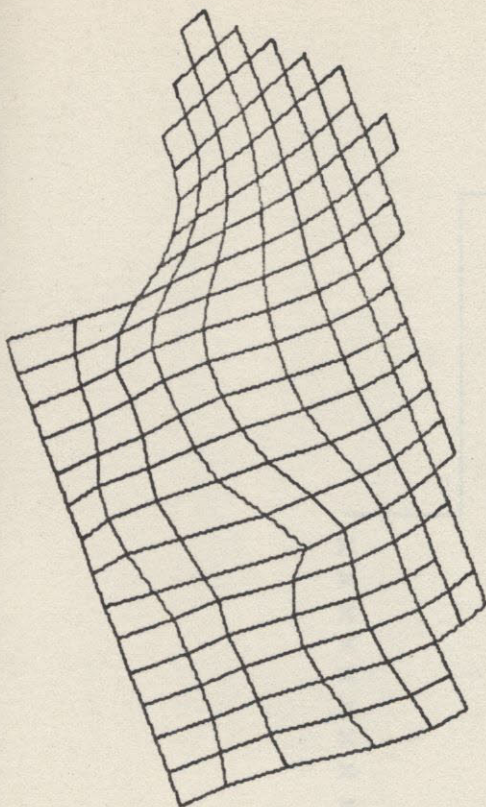
The lattice used is the Richardson lattice described in Section 4 and Figure 4-1. A double Richardson lattice (Welander, 1961) was tried originally, but the Coriolis coupling between the two lattices was too weak to dampen the " $2\Delta x$ " oscillations. Artificial damping via an extra diffusion equation was imposed, but the damping required to reduce the numerical oscillations severely dampens the seiche signals as well. Although the double Richardson lattice offers higher spatial resolution, mesh instabilities render it ineffective in this case.

The response to $\zeta_0^\Gamma(t)$ is shown as a time series of 3-D surfaces in Figure 5-1. The elevation time series at four mesh points is shown in Figure 5-3. The locations of the mesh points are shown in Figure 5-2. $\zeta_0^\Gamma(t) = 1$ meter for $t \rightarrow \infty$. The elevations at each of the observation points approach 1 meter elevation as expected. The lee of the island appears to be a source of strong oscillations. A wave appears to enter the upper Bight traveling in a northeasterly direction. This is verified by the zero phase difference observed between the "+" and "x" signals in Figure 5-3.

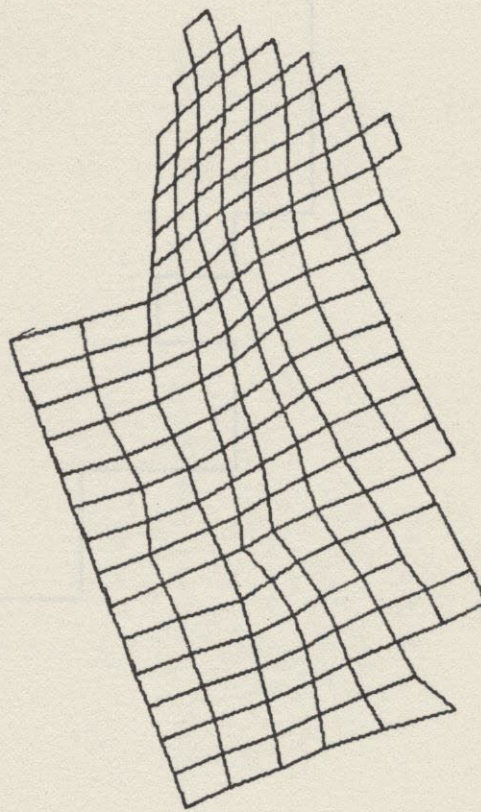
Responses to τ_x^Γ and τ_y^Γ are shown in Figures 5-4 and 5-5, respectively. The associated surface contours appear in Figures 5-6 and 5-7, respectively. The surface responds more strongly at lower frequencies to the τ_x^Γ and τ_y^Γ transients since the forcing is not localized as is the $\zeta_0^\Gamma(t)$ forcing. Of special interest is the equilibrium velocity field produced by τ_x^Γ and τ_y^Γ as shown in Figures 5-8 and 5-9. In both cases, a large gyre appears in the north end of the Bight as a result of the $\nabla \times \vec{\tau} / h$ term in the vorticity equation.



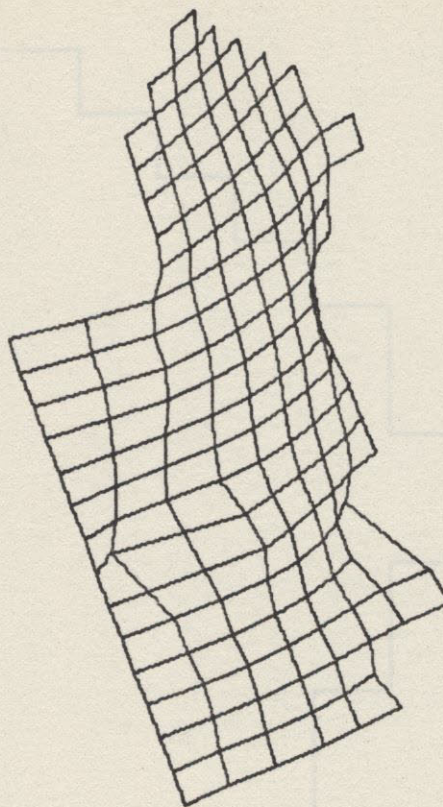
TIME = .5 hrs



TIME = 1.0 hrs



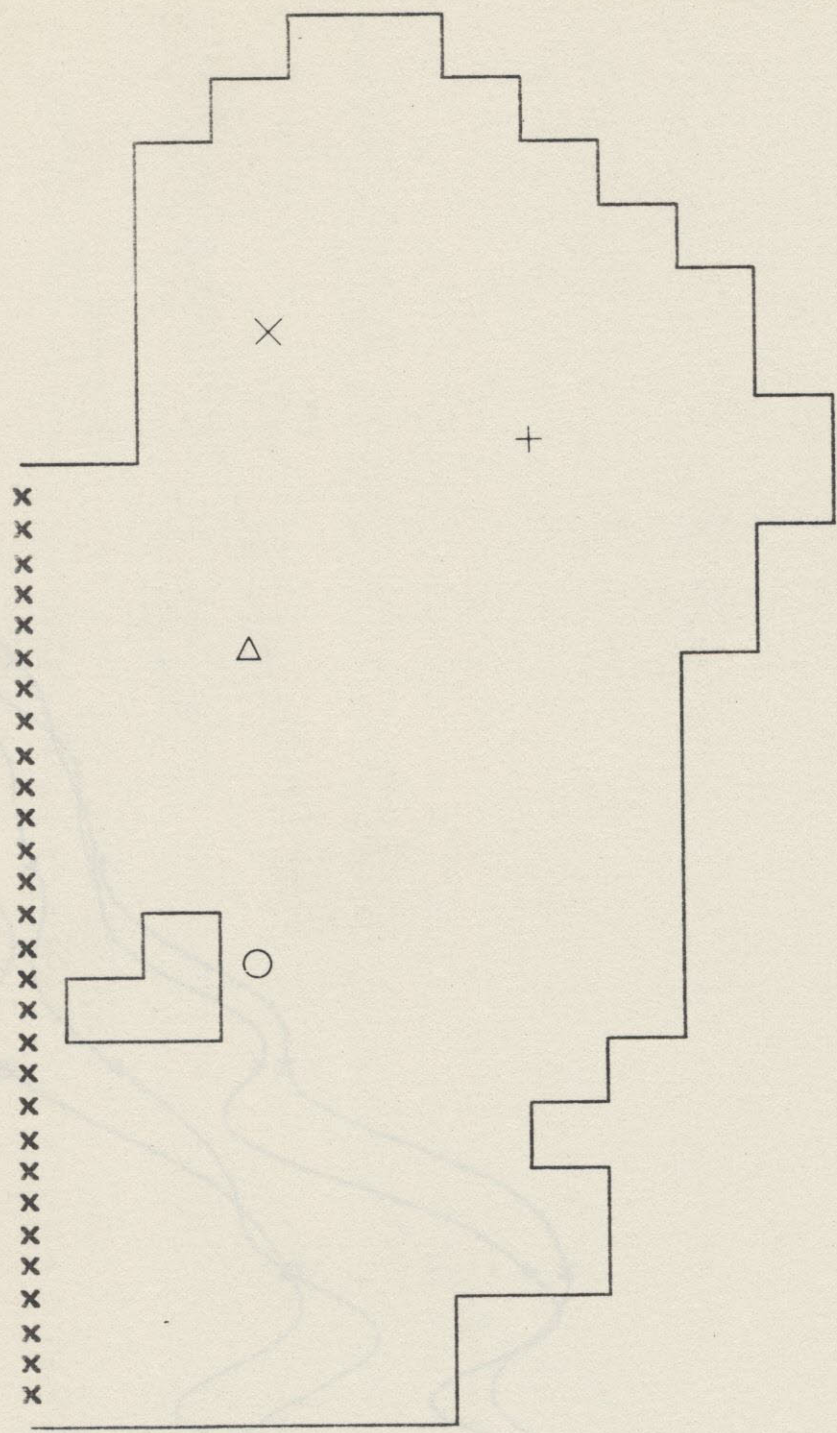
TIME = 1.5 hrs



TIME = 2.0 hrs

ELEVATION RESPONSE TO ELEVATION STEP AT OPENING

Figure 5-1



ELEVATION SAMPLING POINTS

Figure 5-2

RESPONSE TO A STEP IN THE BOUNDARY ELEVATION

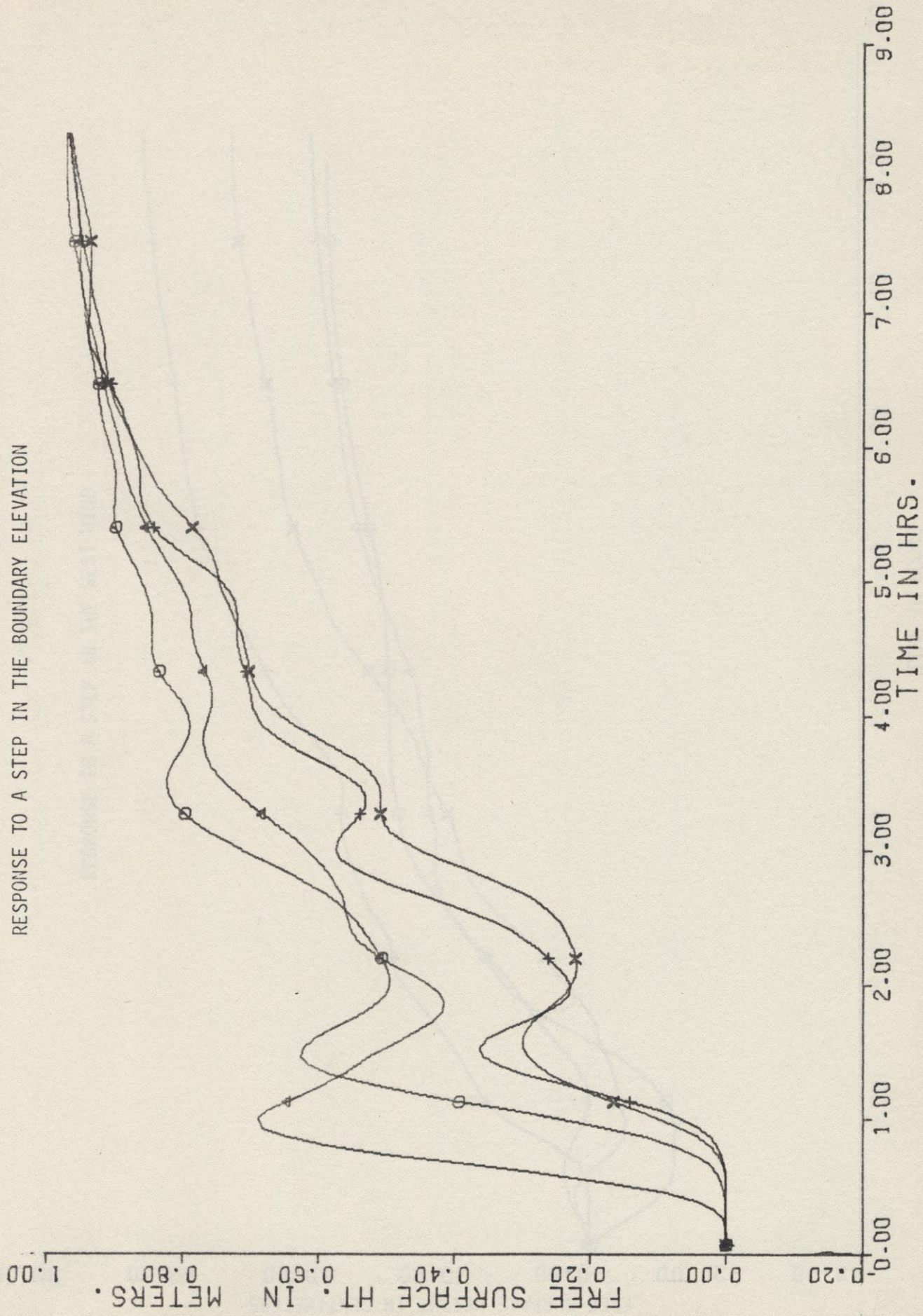
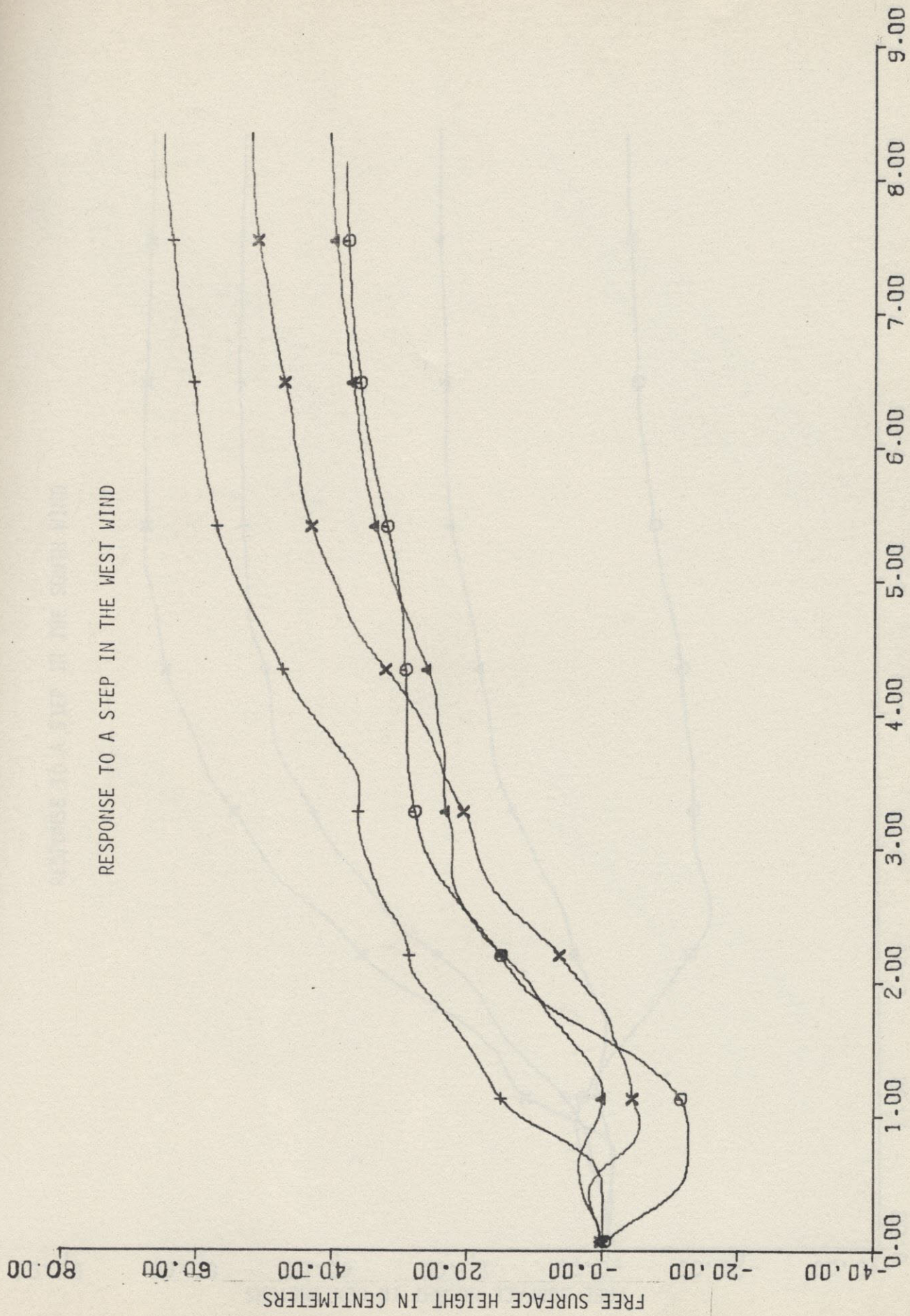


Figure 5-3

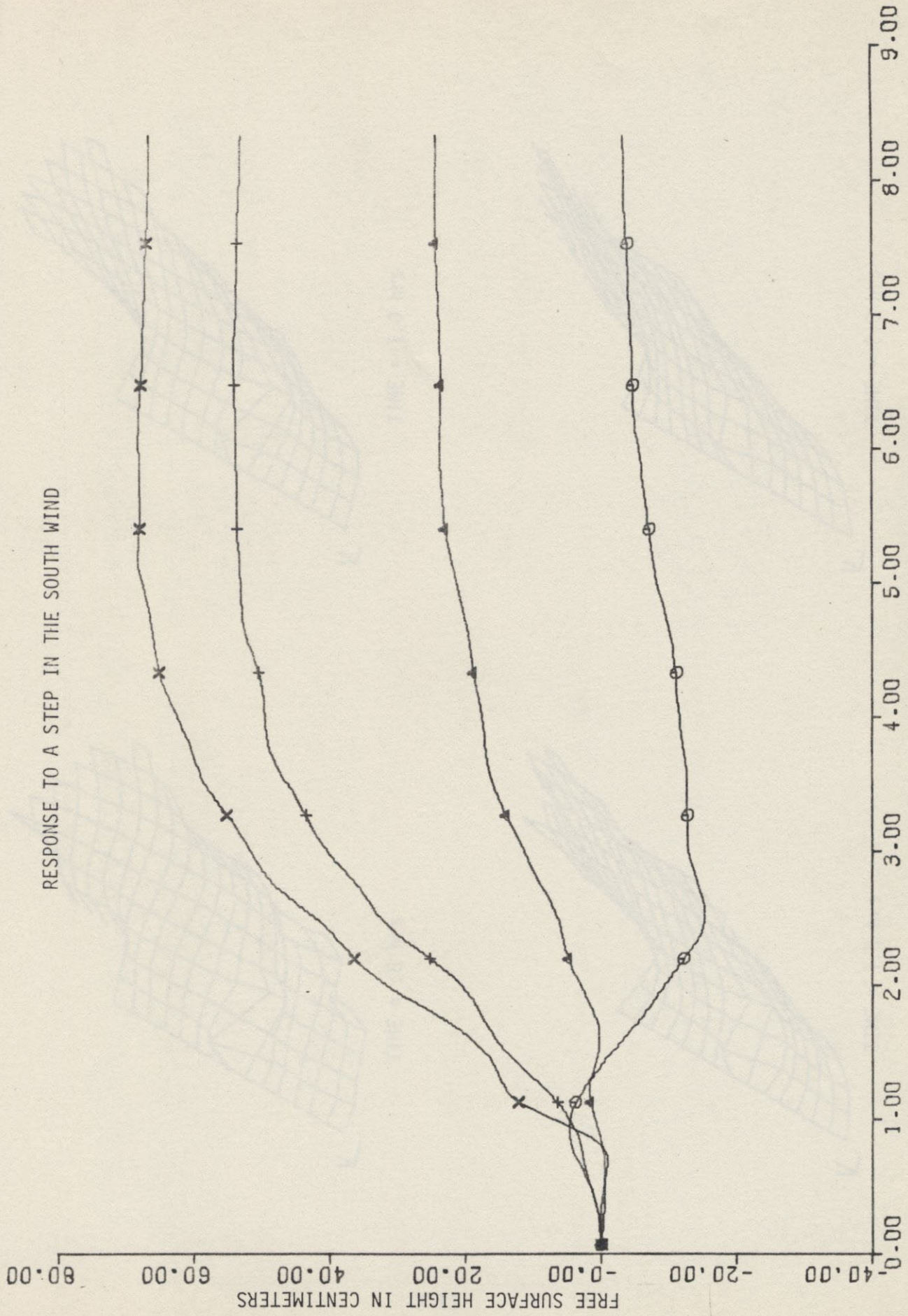
RESPONSE TO A STEP IN THE WEST WIND



TIME IN HOURS

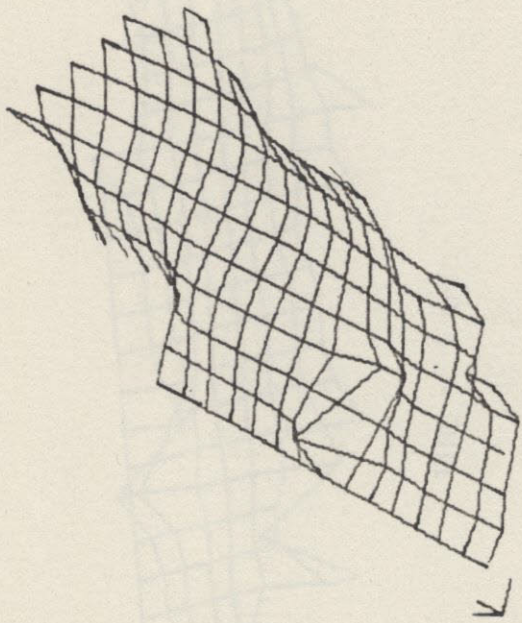
Figure 5-4

RESPONSE TO A STEP IN THE SOUTH WIND

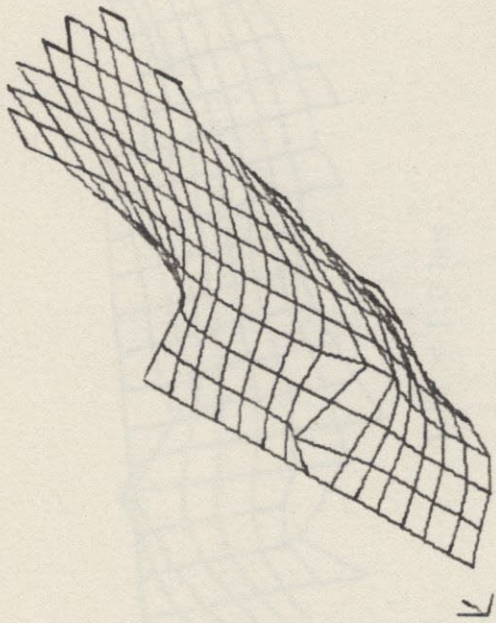


TIME IN HOURS

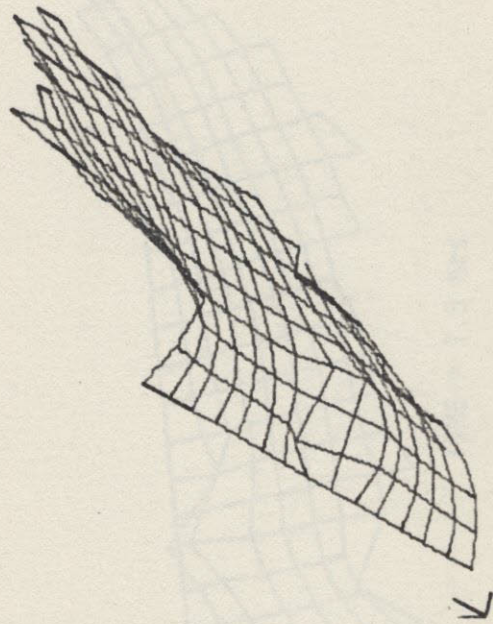
Figure 5-5



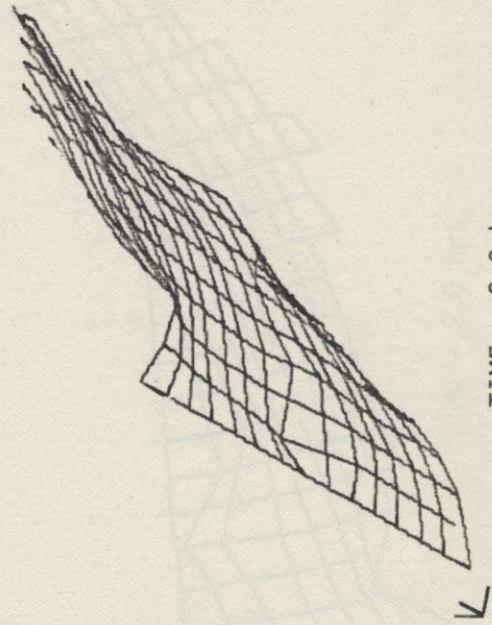
TIME = .5 hrs



TIME = 1.0 hrs



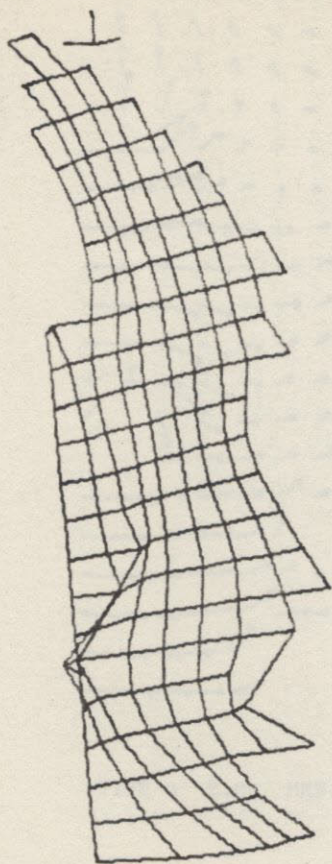
TIME = 1.5 hrs



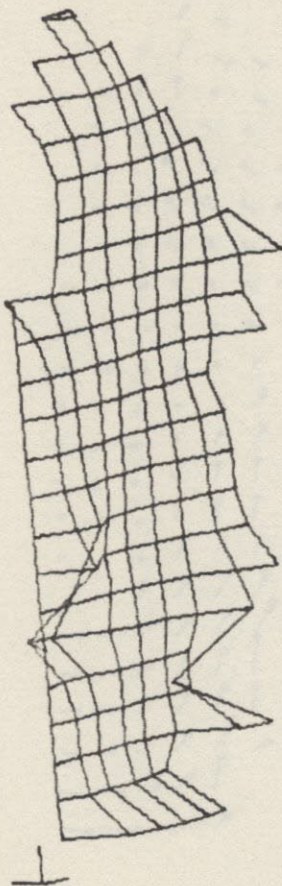
TIME = 2.0 hrs

ELEVATION RESPONSE TO A STEP IN THE WEST WIND

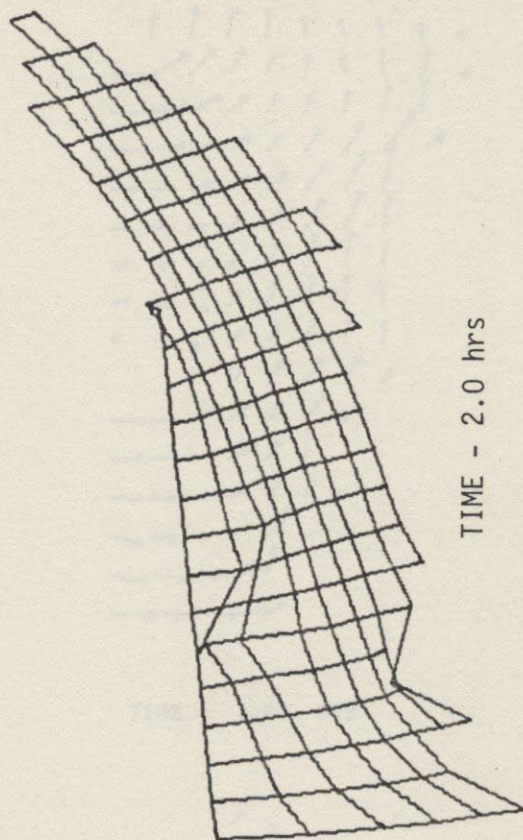
Figure 5-6



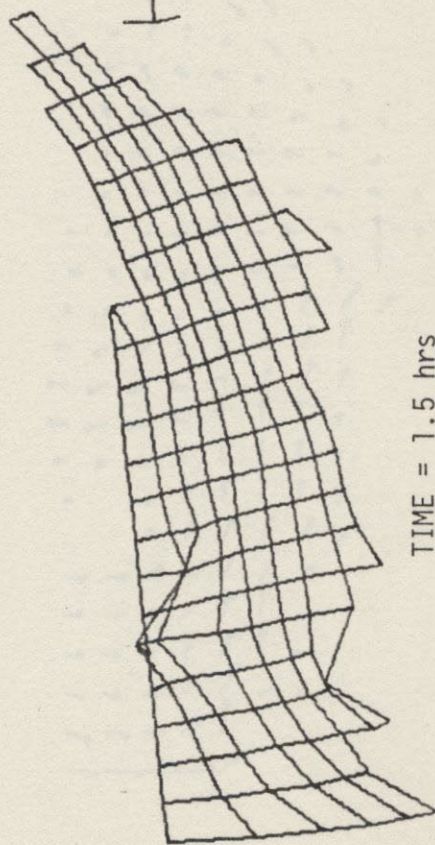
TIME = 1.0 hrs



TIME = .5 hrs



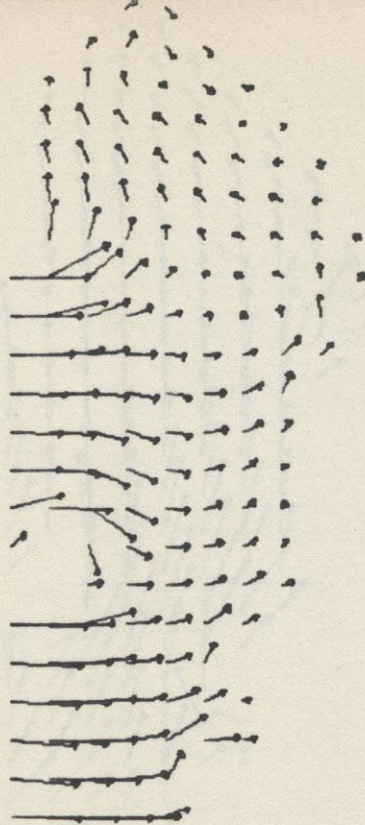
TIME = 2.0 hrs



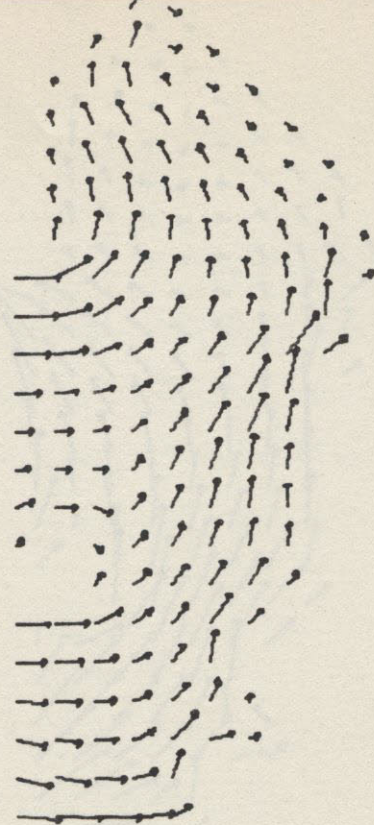
TIME = 1.5 hrs

ELEVATION RESPONSE TO A STEP IN THE SOUTH WIND

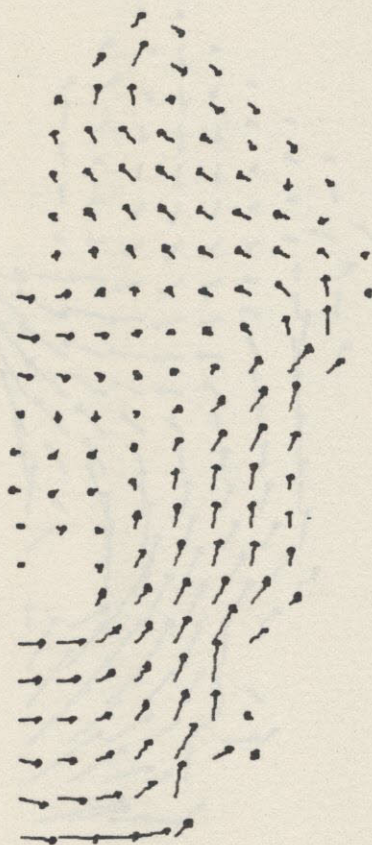
Figure 5-7



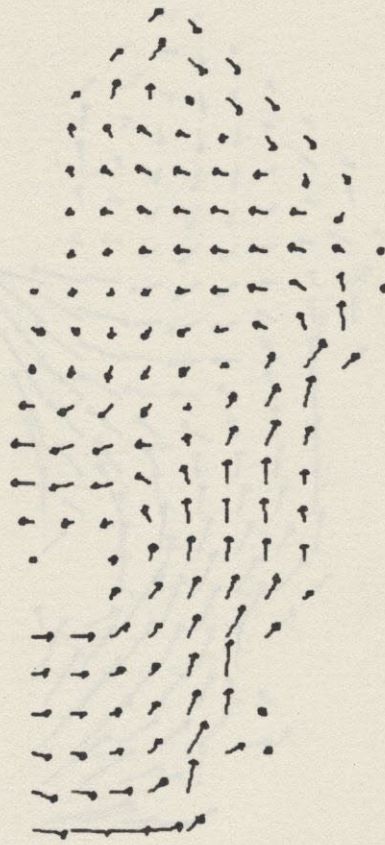
TIME = 2.00 HRS.



TIME = 4.00 HRS.



TIME = 6.00 HRS.

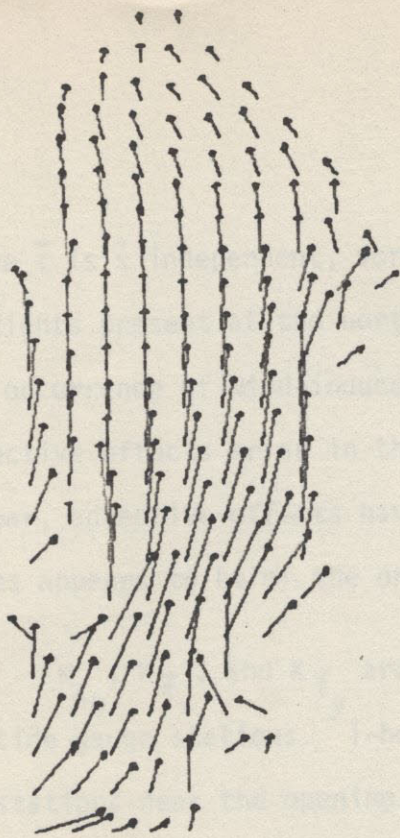


TIME = 8.00 HRS.

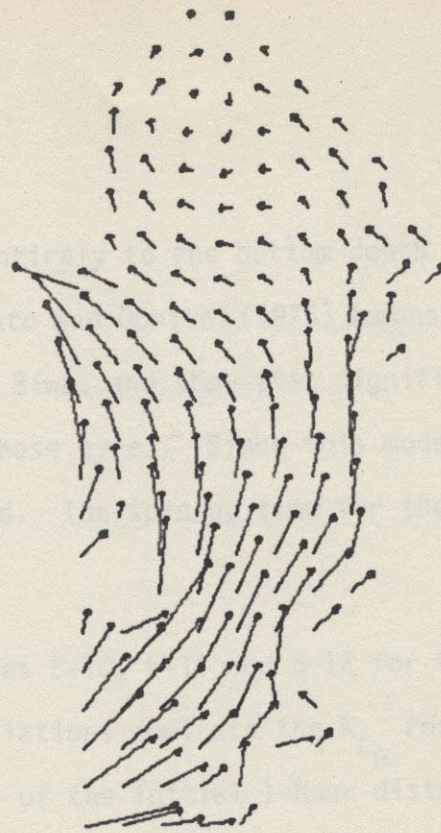
Figure 5-8

5-13

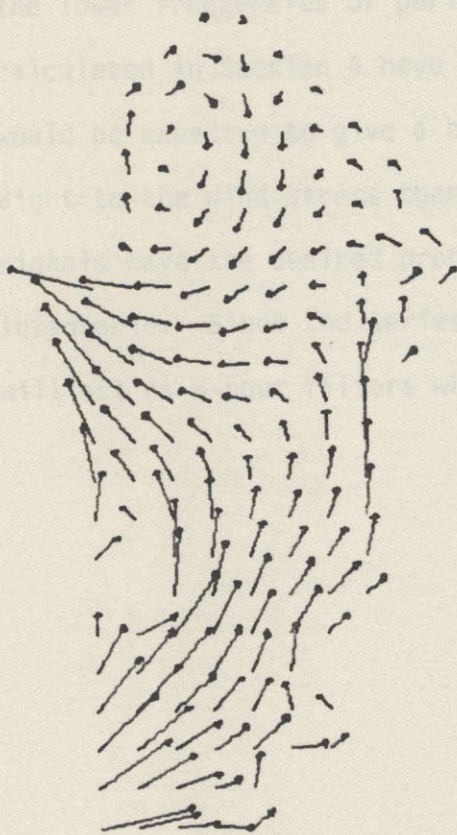
VELOCITY FIELD RESPONSE TO A STEP IN THE WEST WIND



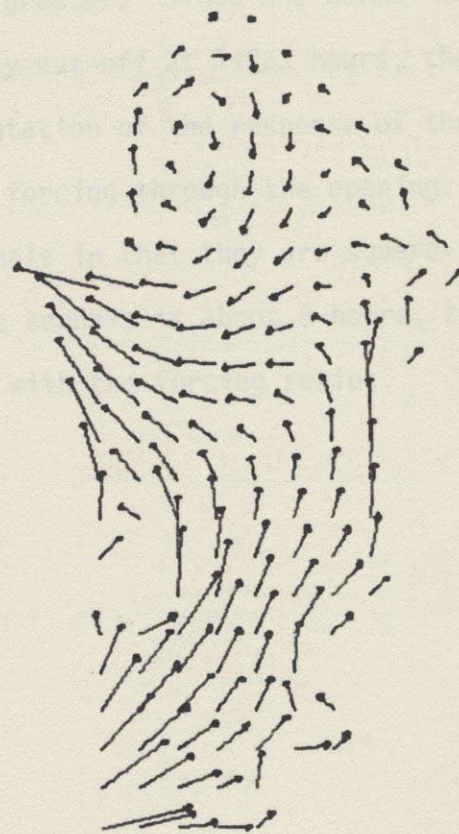
TIME = 2.00 HRS.



TIME = 4.00 HRS.



TIME = 6.00 HRS.



TIME = 8.00 HRS.

Figure 5-9

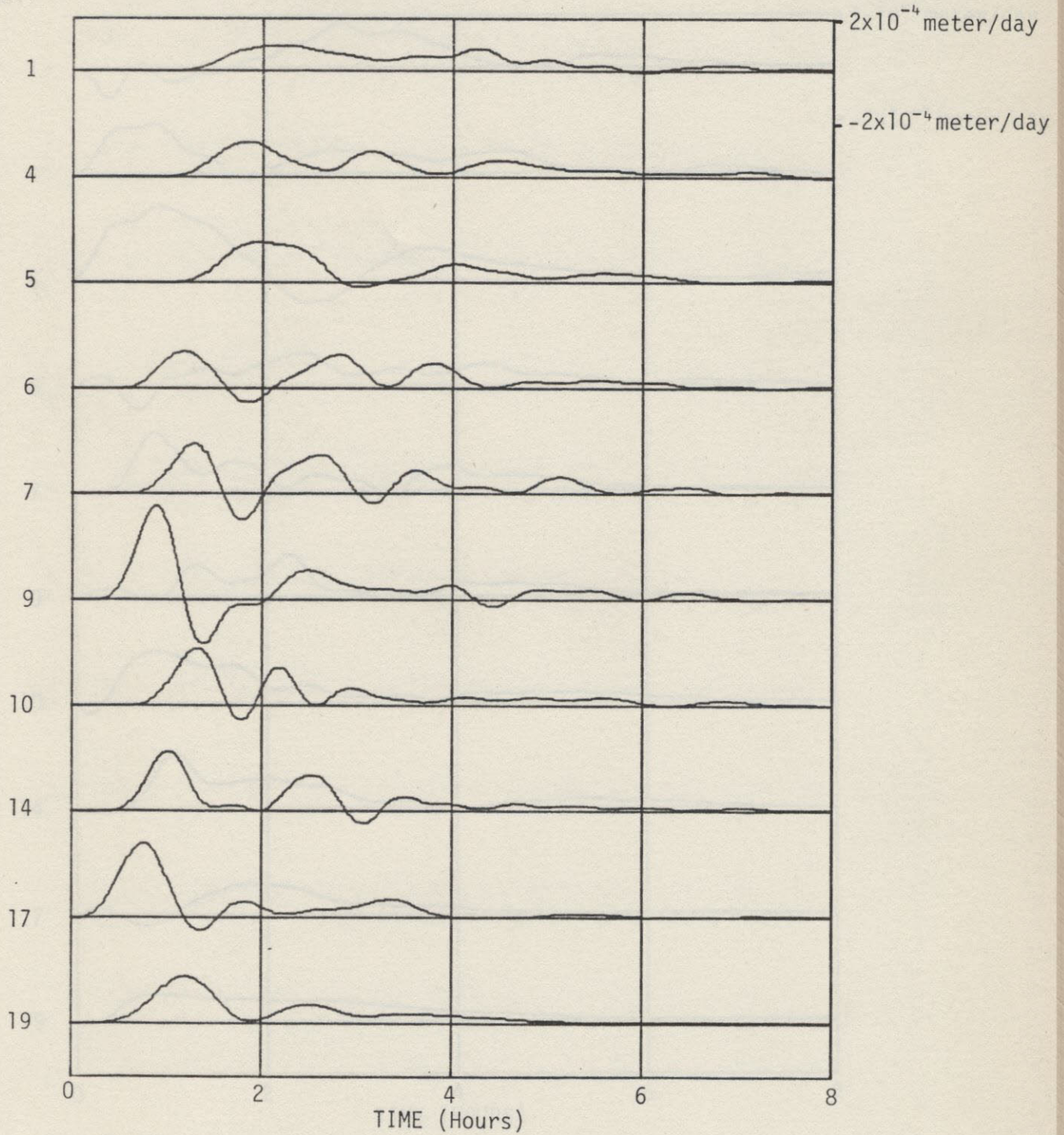
VELOCITY FIELD RESPONSE TO A STEP IN THE SOUTH WIND

Since $\vec{\tau}$ is \vec{x} independent, vorticity is due entirely to the bottom depth gradients present at the northern end. Imasato and Oonishi (1975) demonstrate the occurrence of wind-induced gyres in Lake Biwa, and show that significant advective effects arise in the vicinity of these gyres. Since this model is linear, advective effects have been neglected. The spin-up time for the gyres appears to be of the order of 6 hours.

K_{ζ_0} , $K_{\vec{\tau}_x}$, and $K_{\vec{\tau}_y}$ are shown in Figures 5-10, 5-11 and 5-12 for the 10 tide gauge stations. 1-hour period oscillations dominate the K_{ζ_0} response at stations near the opening. The amplitude of the initial 1-hour disturbance dampens toward the north end as the energy input at the opening dissipates. $K_{\vec{\tau}_x}$ and $K_{\vec{\tau}_y}$ are characterized by a concentration of energy in the lower frequencies of period 2 hours or greater. Since the normal modes calculated in Section 4 have a low frequency cut-off at 1-2/3 hours, they would be expected to give a better representation of the response of the Bight to the wind stress than to elevation forcing through the opening. The signals have the desired properties of kernels in that they are square-integrable. Since the series length of the kernels is about 8 hours, they will act as 8-hour filters when convoluted with the forcing series.



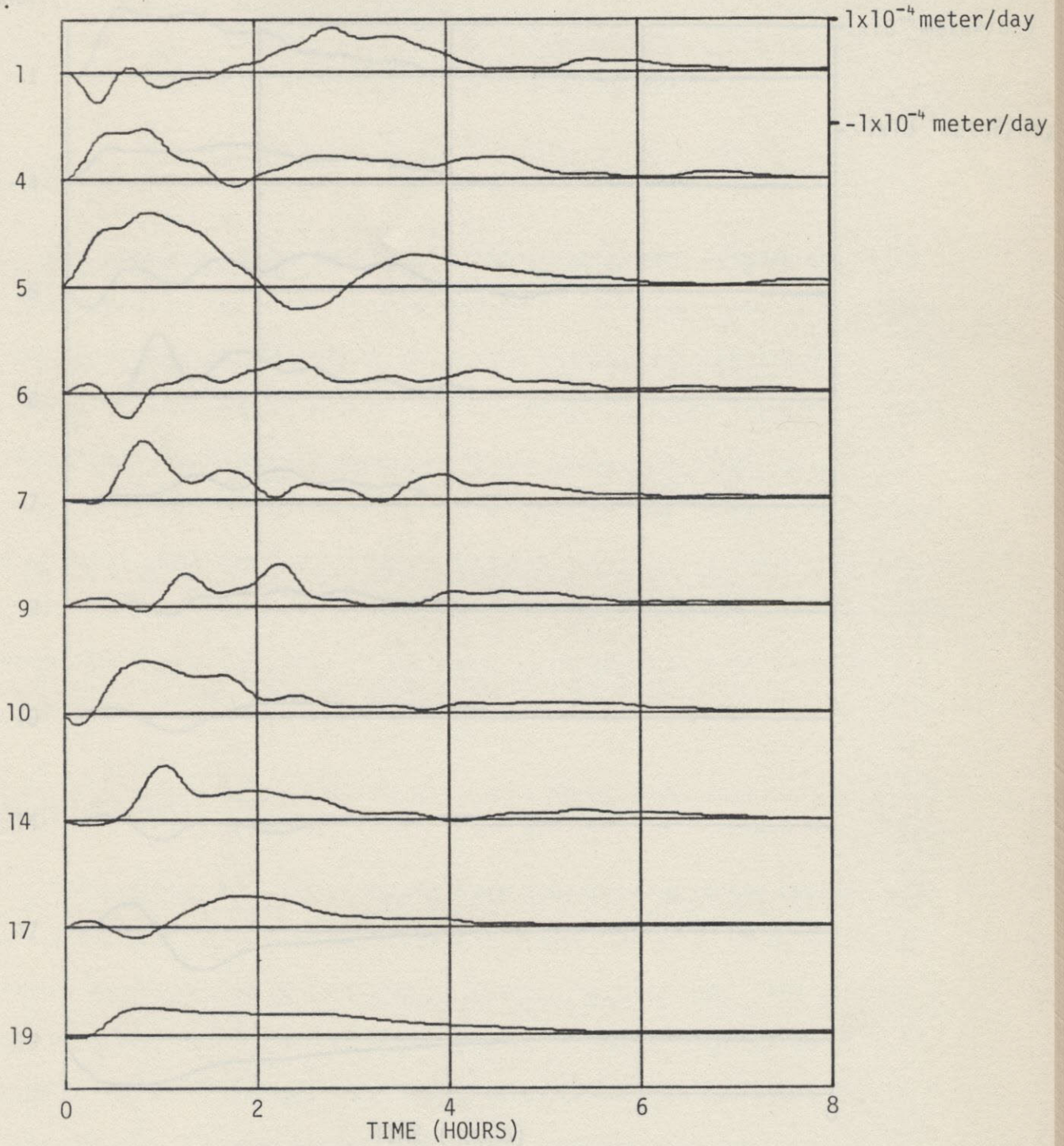
STATION
NO.



RESPONSE TO DELTA FUNCTION RISE IN
ELEVATION AT THE OPENING

Figure 5-10

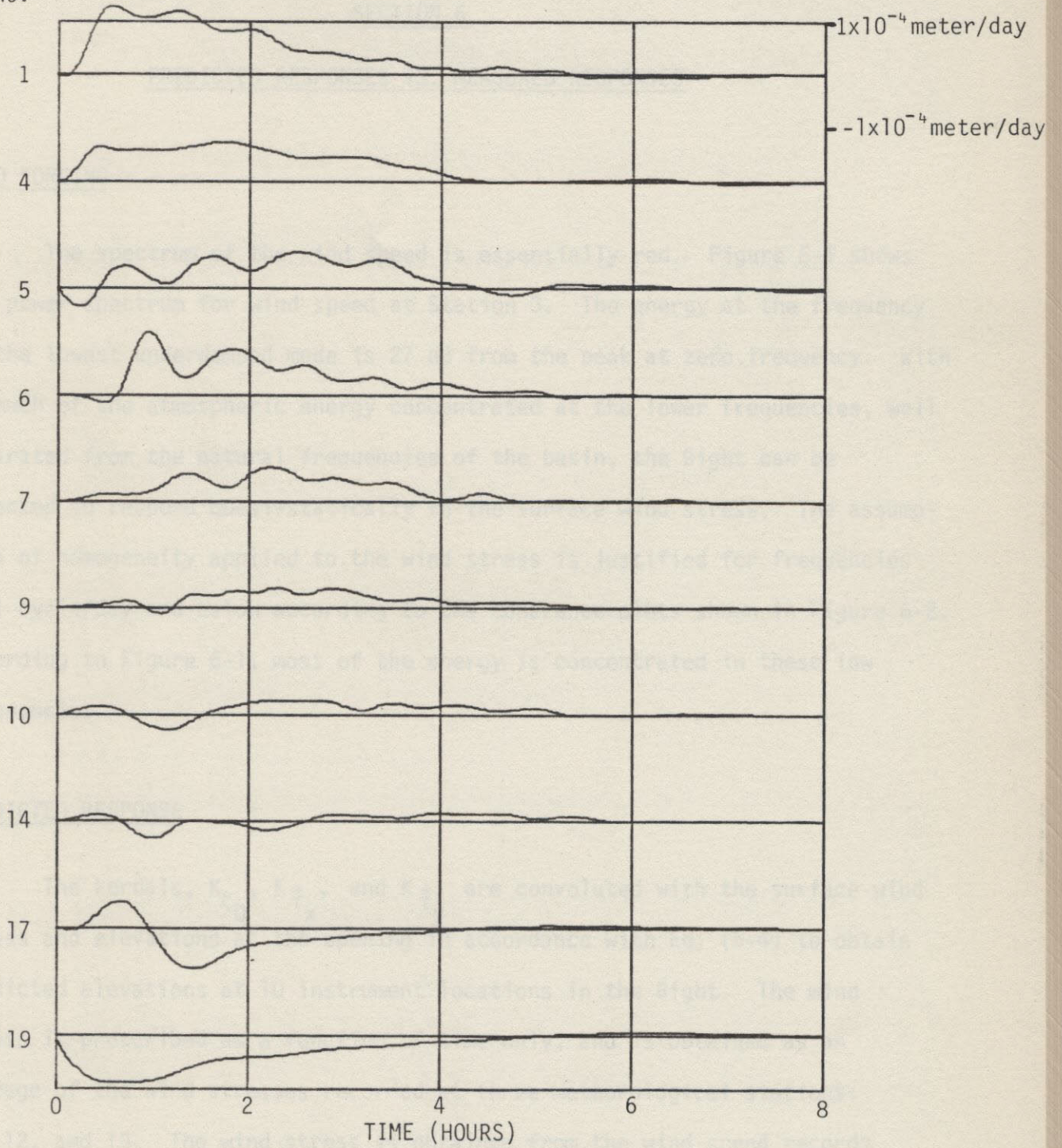
STATION
NO.



RESPONSE TO DELTA FUNCTION WIND STRESS
IN THE X DIRECTION

Figure 5-11

STATION
NO.



RESPONSE TO DELTA FUNCTION WIND STRESS
IN THE Y DIRECTION

Figure 5-12

SECTION 6

PREDICTED RESPONSES VS. MEASURED RESPONSES

WIND FORCING

The spectrum of the wind speed is essentially red. Figure 6-1 shows the power spectrum for wind speed at Station 3. The energy at the frequency of the lowest underdamped mode is 27 dB from the peak at zero frequency. With so much of the atmospheric energy concentrated at the lower frequencies, well separated from the natural frequencies of the basin, the Bight can be expected to respond quasi-statically to the surface wind stress. The assumption of homogeneity applied to the wind stress is justified for frequencies of 1 cycle/day and below according to the coherence plots shown in Figure 6-2. According to Figure 6-1, most of the energy is concentrated in these low frequencies.

PREDICTED RESPONSE

The kernals, K_{ζ_0} , K_{τ_x} , and K_{τ_y} are convoluted with the surface wind stress and elevations at the opening in accordance with Eq. (5-4) to obtain predicted elevations at 10 instrument locations in the Bight. The wind stress is prescribed as a function of time only, and is obtained as an average of the wind stresses recorded at three meteorological stations: 11, 12, and 18. The wind stress is obtained from the wind speed records by employing the quadratic drag law:

POWER SPECTRUM OF WIND SPEED
STATION 3

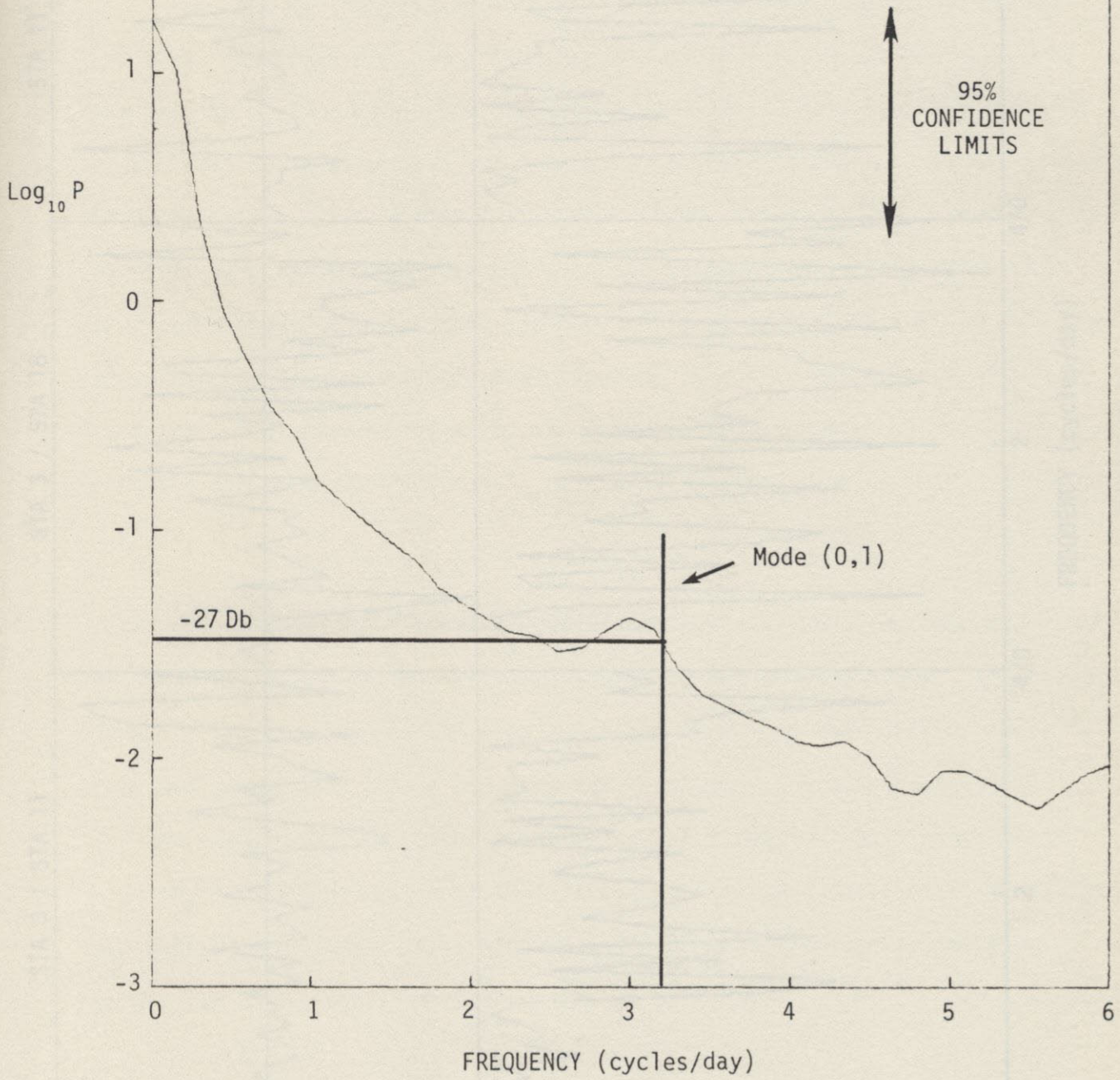


Figure 6-1

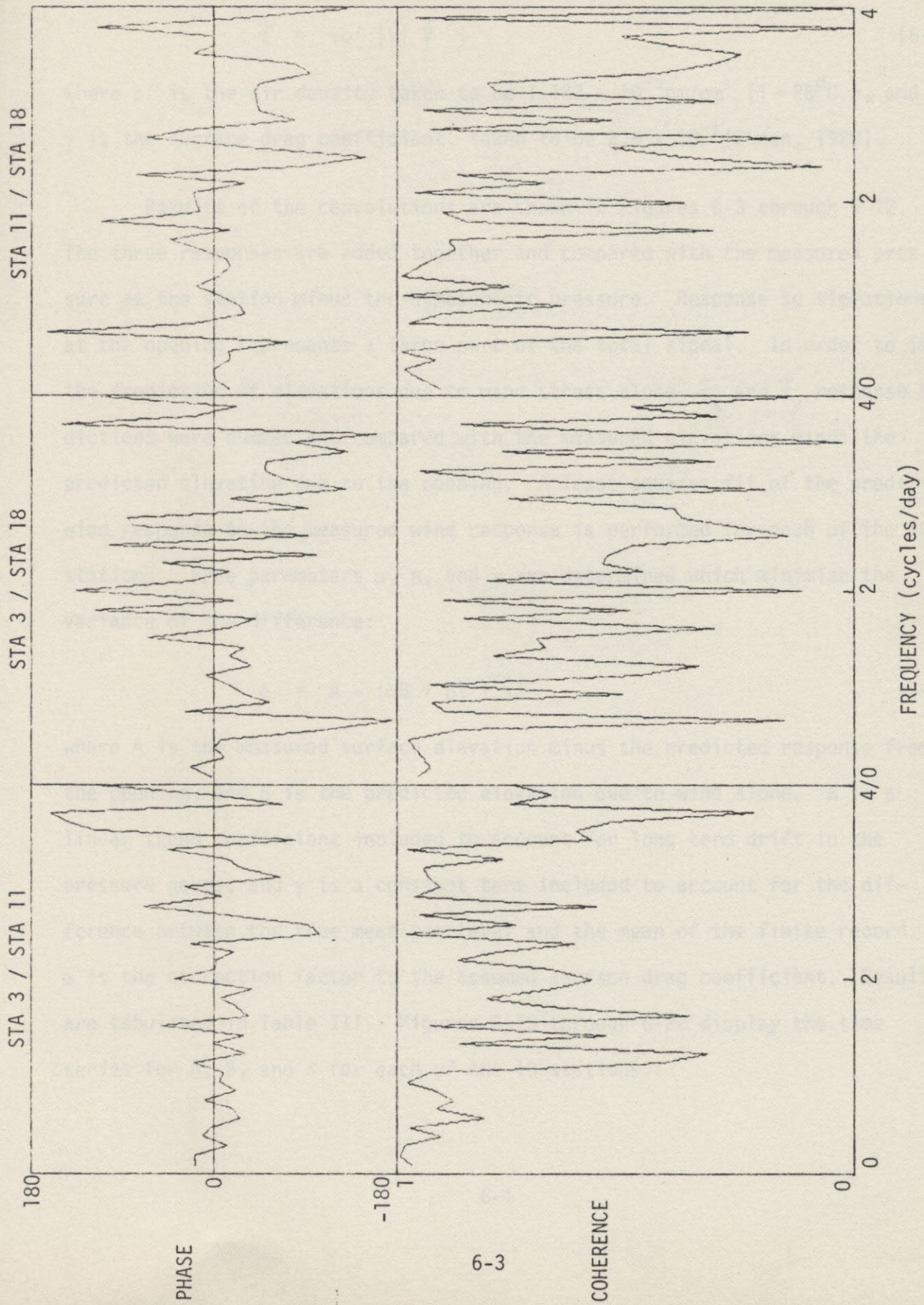


Figure 6-2

$$\vec{\tau} = \gamma \rho' |\vec{V}| \vec{V} , \quad (6-1)$$

where ρ' is the air density taken to be $1.122 \times 10^{-3} \text{ gm/cm}^3$ ($T = 25^\circ\text{C.}$), and γ is the surface drag coefficient, taken to be 2.6×10^{-3} (Ekman, 1928).

Results of the convolutions are shown in Figures 6-3 through 6-12. The three responses are added together and compared with the measured pressure at the station minus the atmospheric pressure. Response to elevations at the opening represents a large part of the total signal. In order to isolate the prediction of elevations due to wind stress alone, $\vec{\tau}_x$ and $\vec{\tau}_y$, response predictions were summed and compared with the measured elevations minus the predicted elevation due to the opening. A least squares fit of the predicted wind response to the measured wind response is performed for each of the 10 stations. Free parameters α , β , and γ are determined which minimize the variance of the difference:

$$\delta = A - (\alpha B + \beta t + \gamma) , \quad (6-2)$$

where A is the measured surface elevation minus the predicted response from the opening, and B is the predicted elevation due to wind alone. β is a linear trend coefficient included to account for long term drift in the pressure gauge, and γ is a constant term included to account for the difference between the true mean sea level and the mean of the finite record. α is the correction factor to the assumed surface drag coefficient. Results are tabulated in Table III. Figures 6-13 through 6-22 display the time series for A , B , and δ for each of the 10 stations.

FIGURES 6-3 TO 6-12

Measured and predicted elevations at 10 stations.

Elevations are scaled from -30cm to +30 cm. Wind velocities are scaled from -30 m/sec to +30 m/sec. Vertical lines are drawn at 2-day intervals.

STATION 1

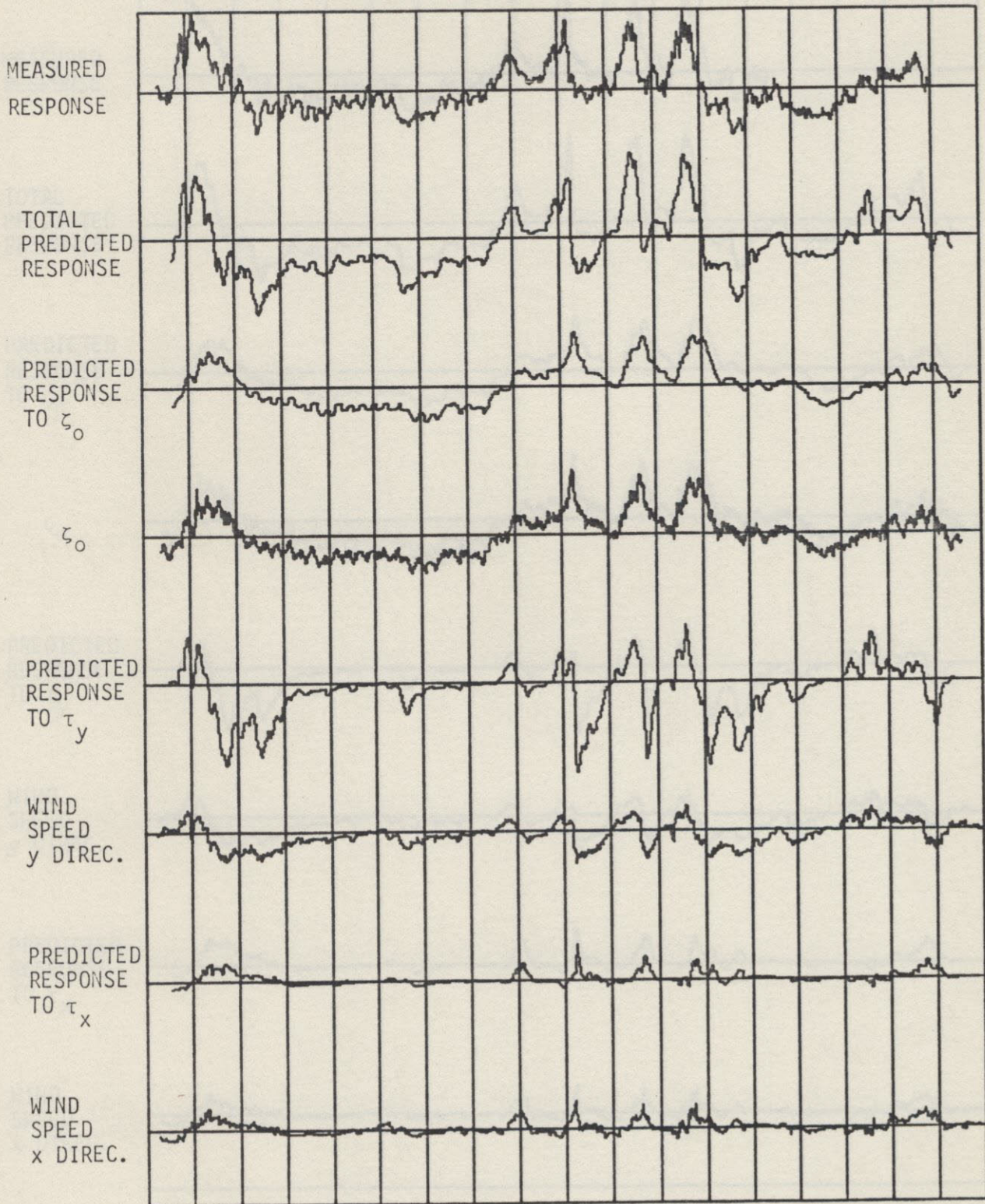


FIGURE 6-3

STATION 4

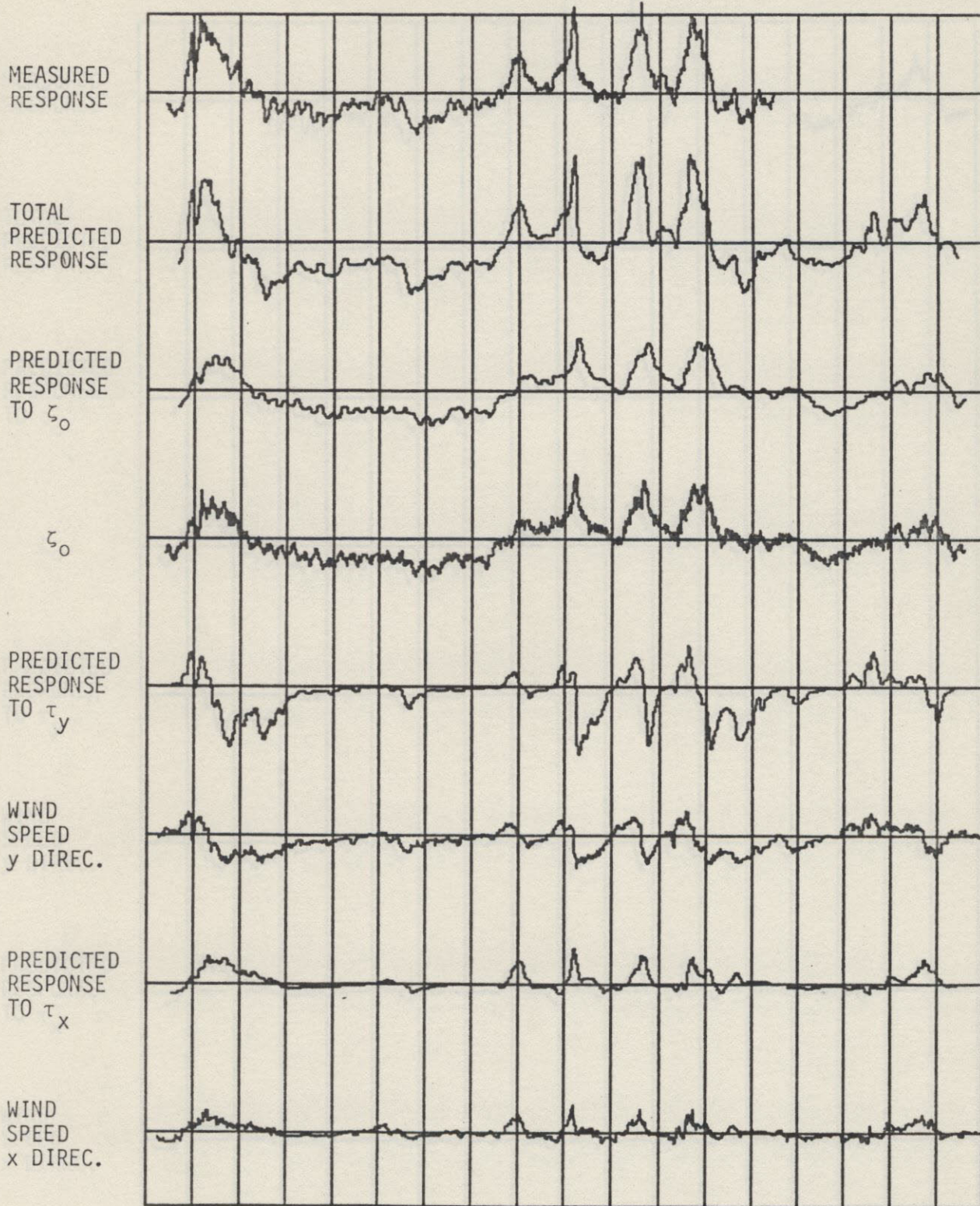


FIGURE 6-4

STATION 5

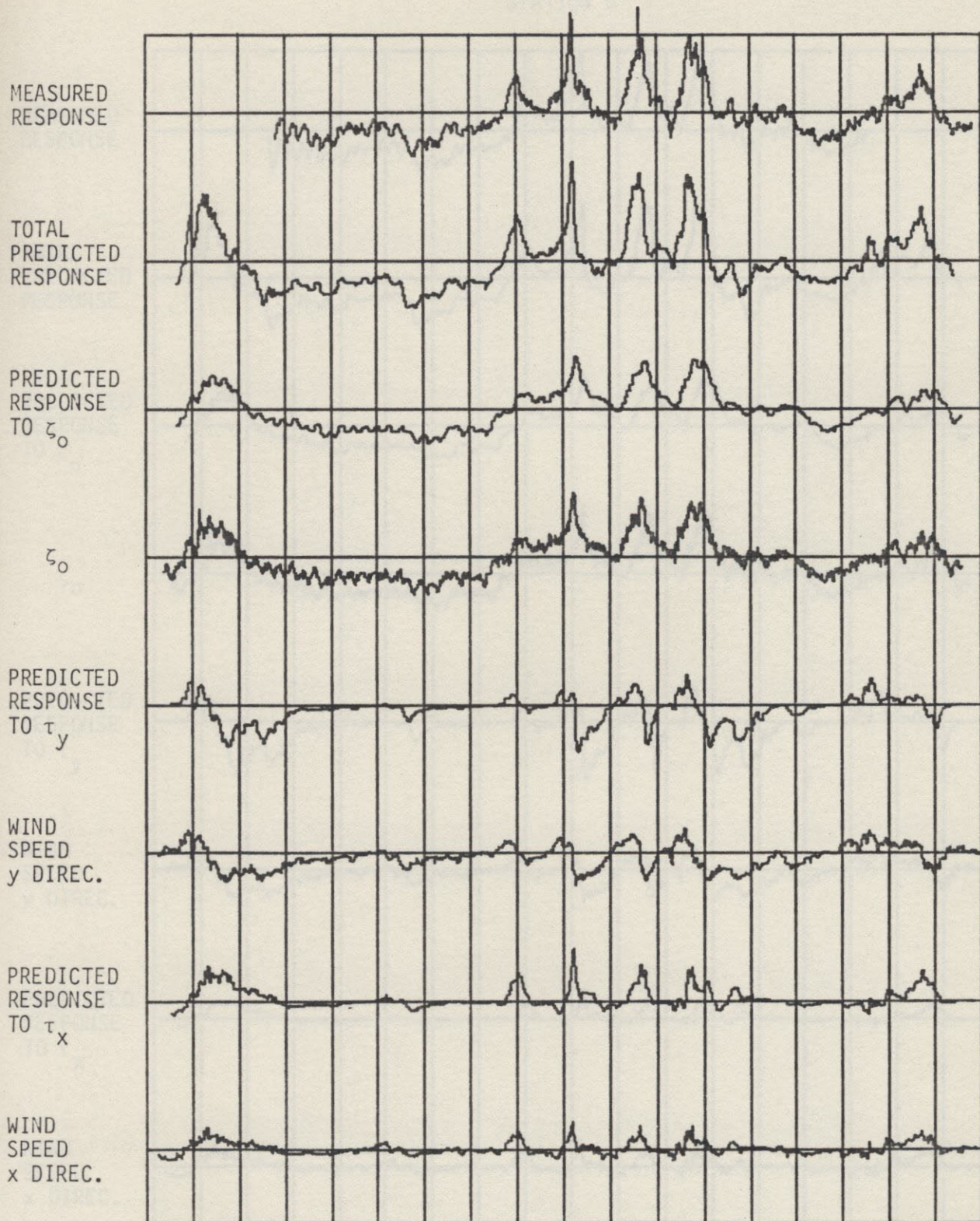


FIGURE 6-5

STATION 6

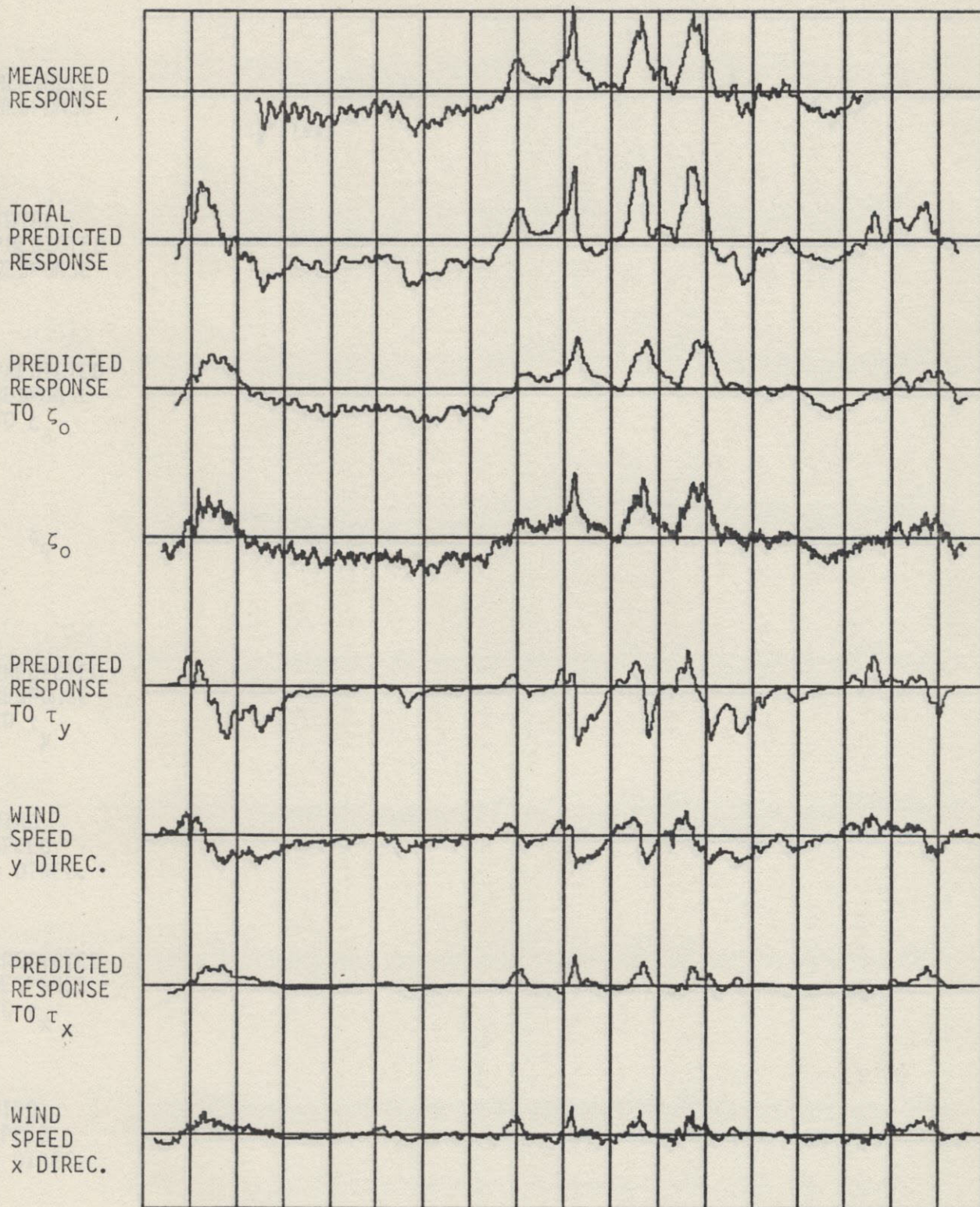


FIGURE 6-6

STATION 7

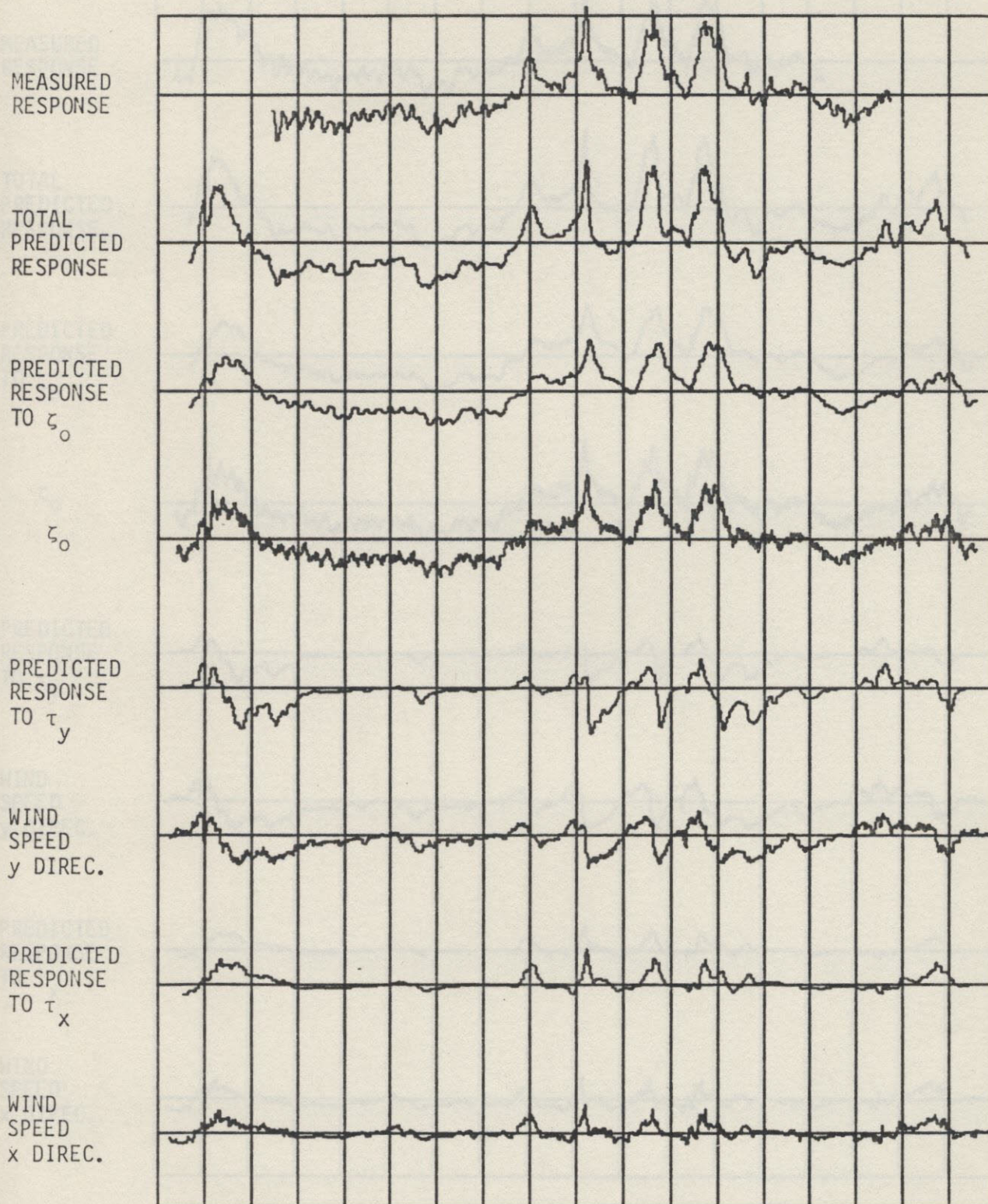


FIGURE 6-7

STATION 9

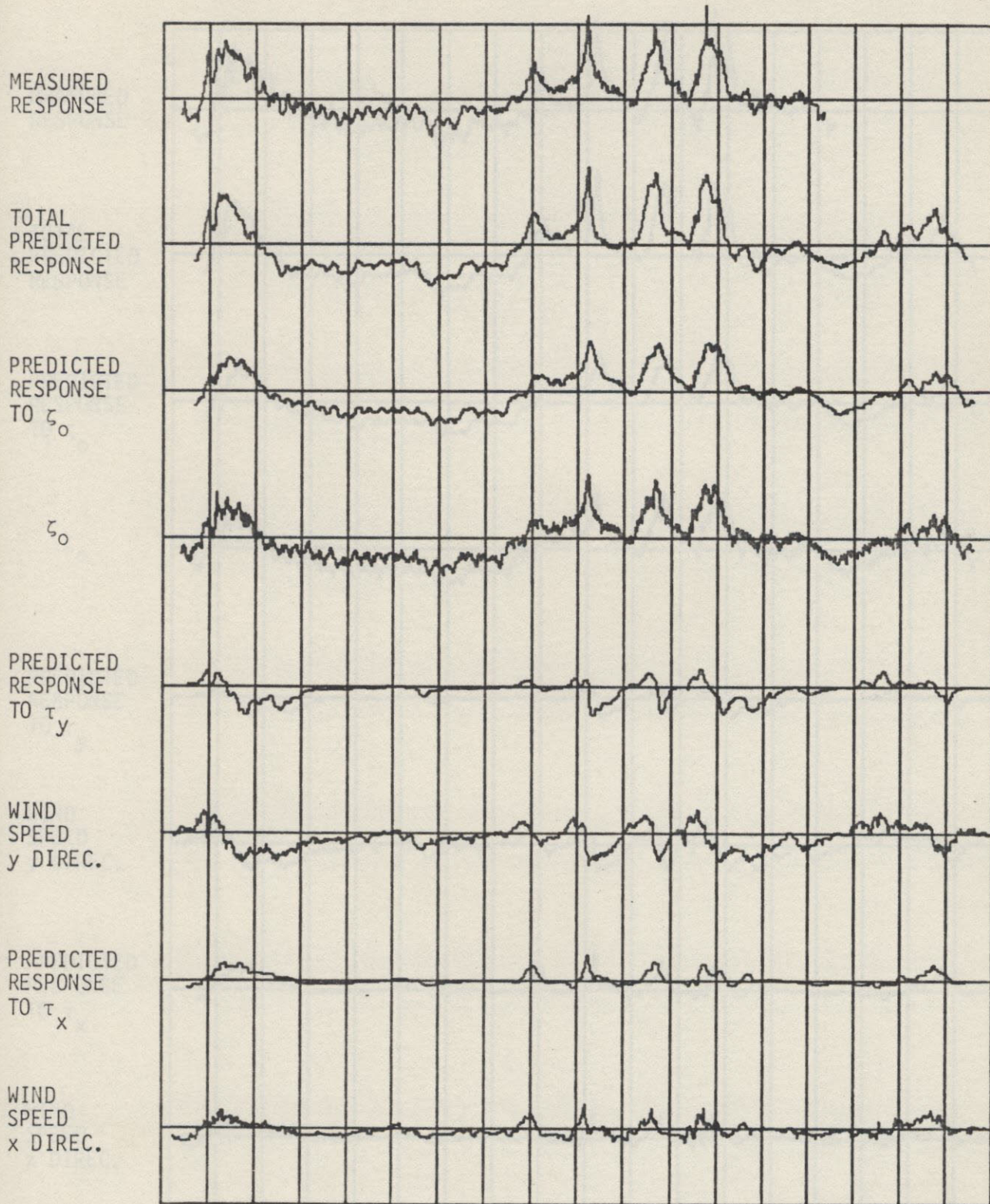


FIGURE 6-8

STATION 10

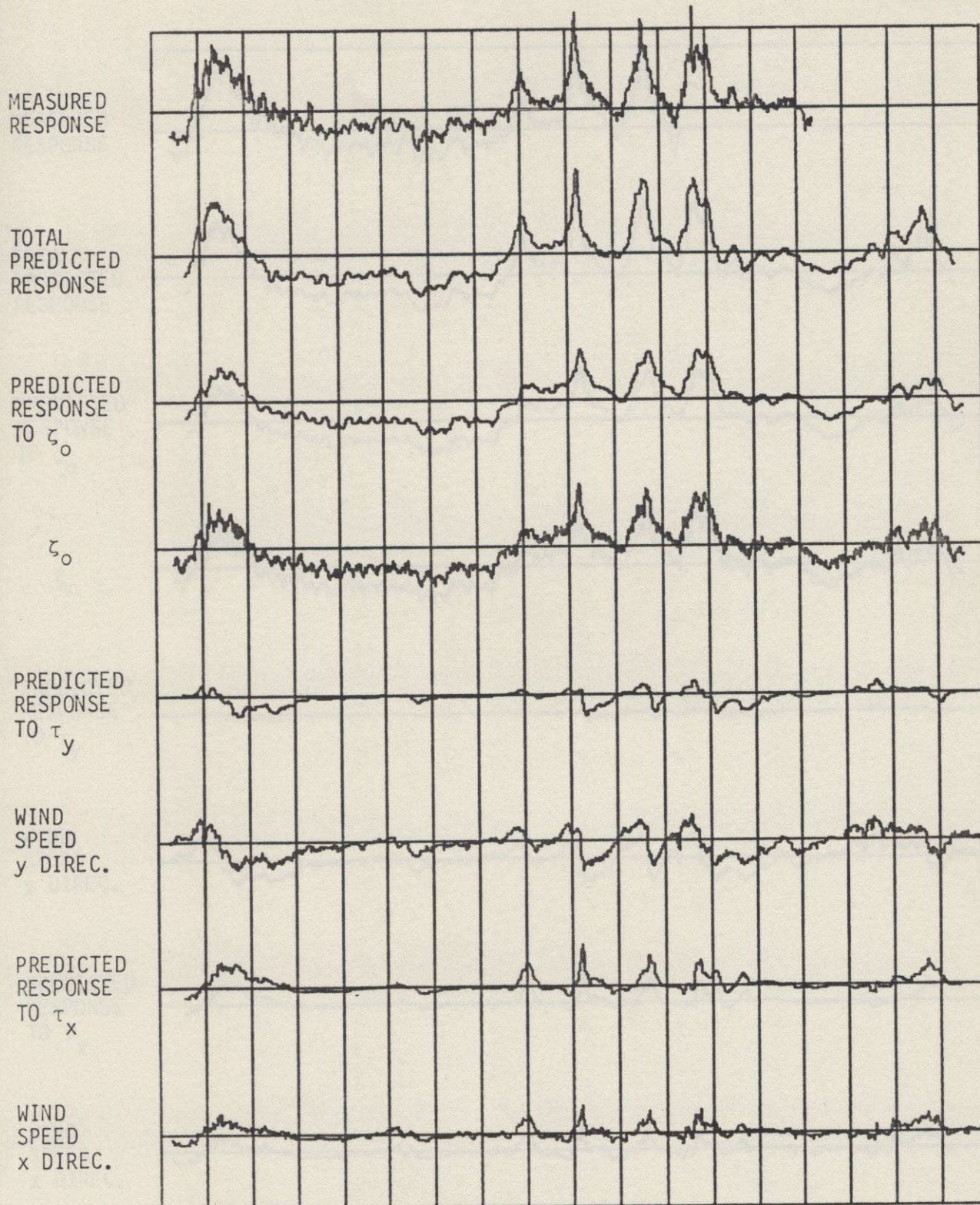


FIGURE 6-9

STATION 14

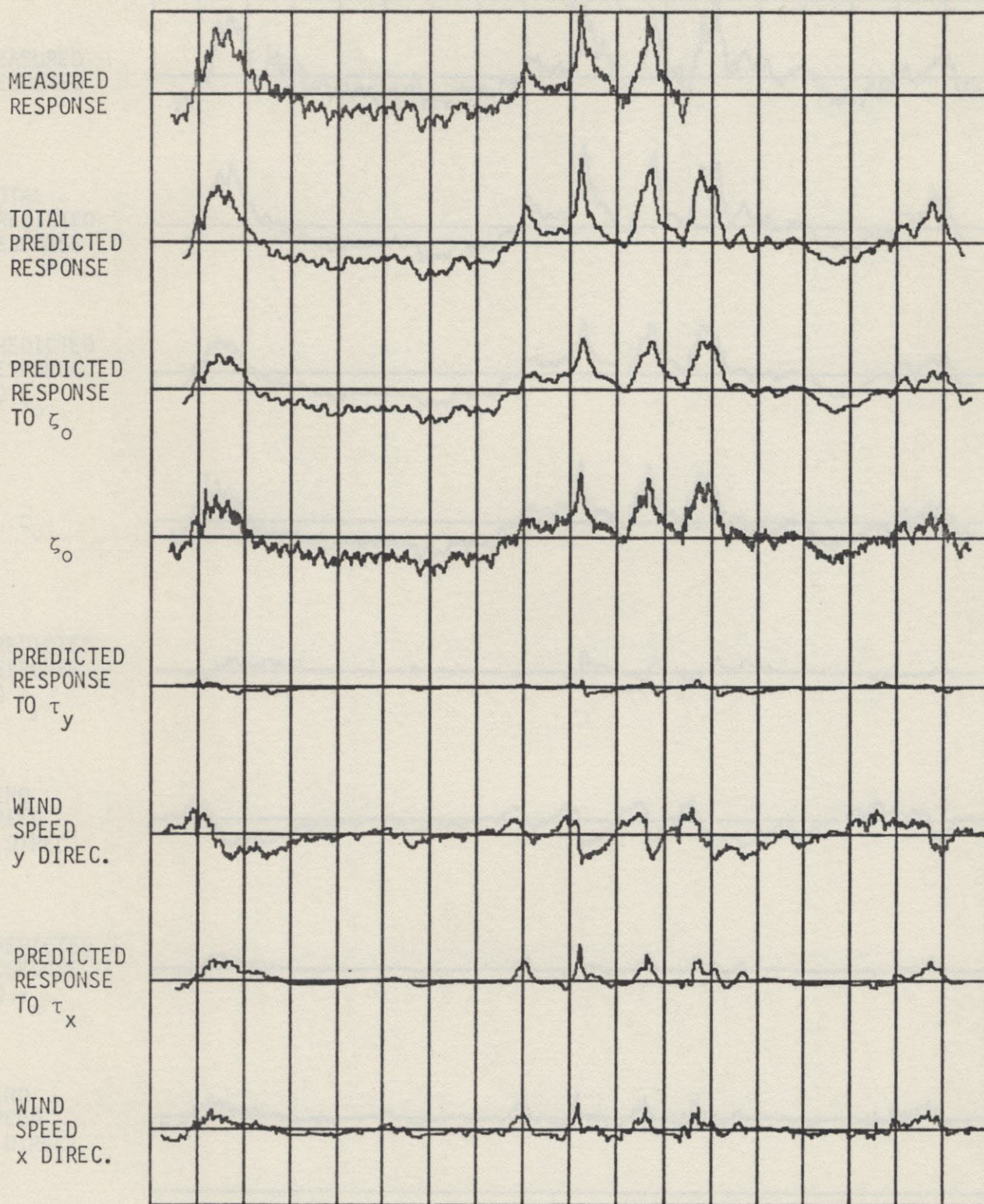


FIGURE 6-10

STATION 17

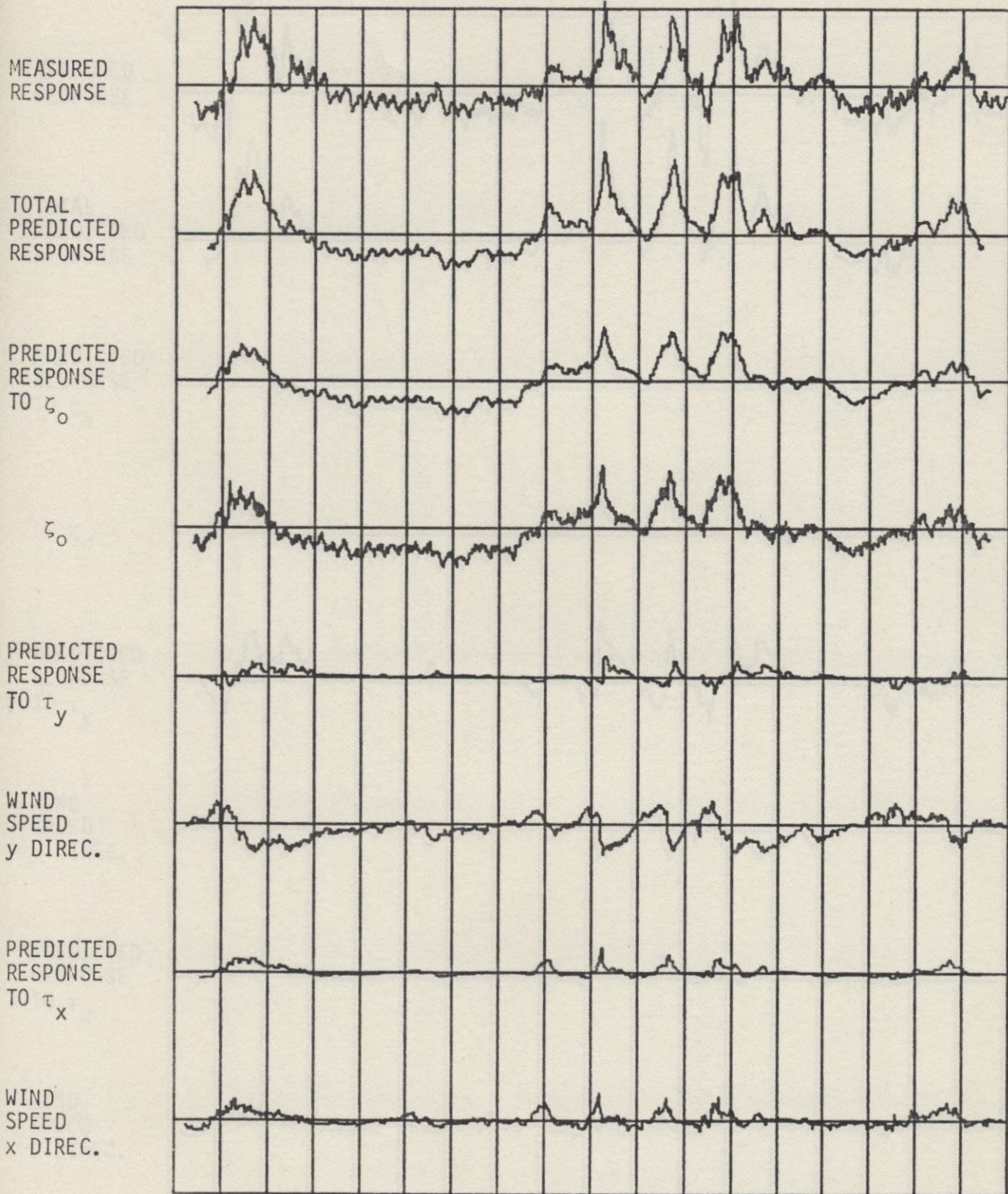


FIGURE 6-11

STATION 19

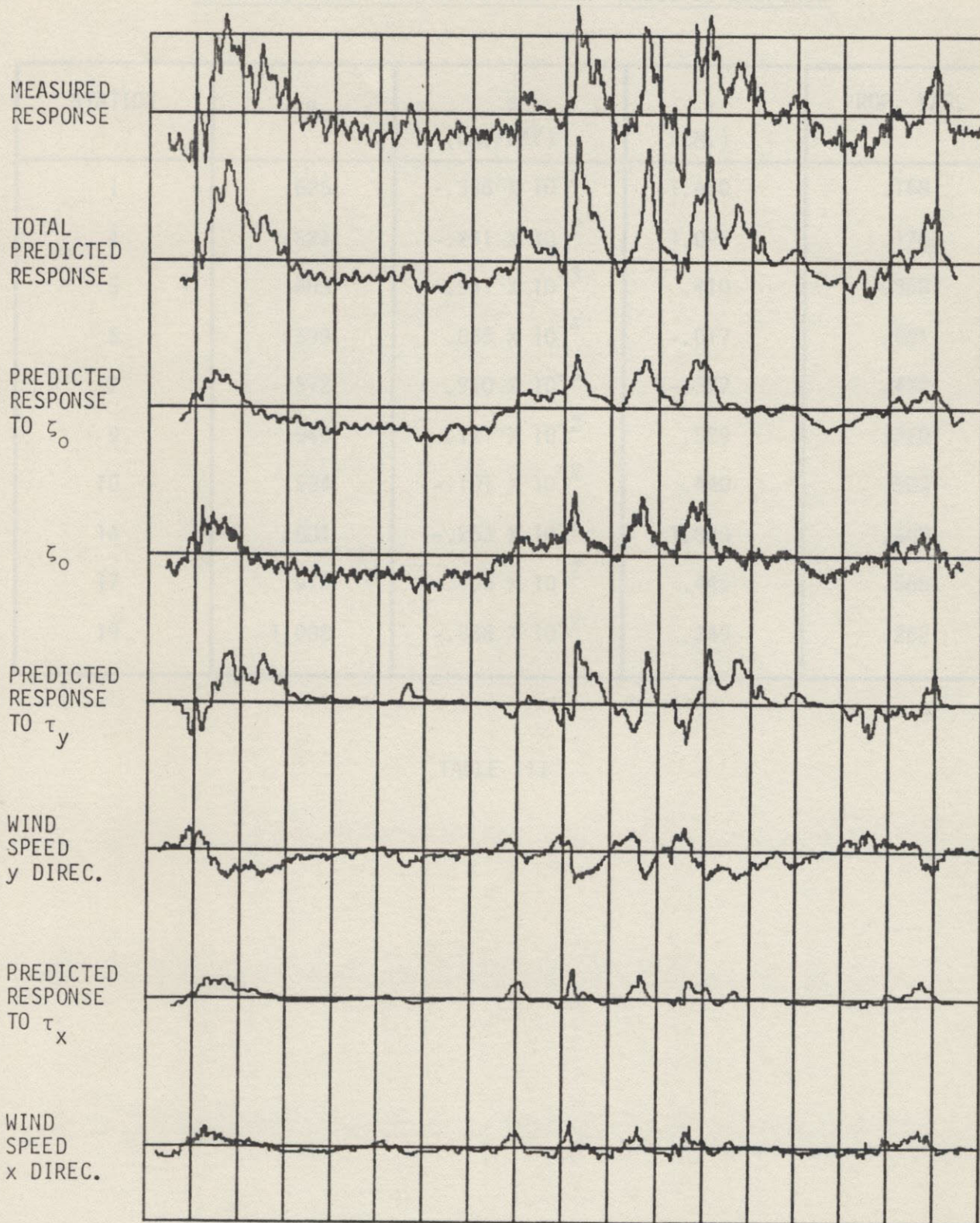


FIGURE 6-12

LEAST SQUARES FIT PARAMETERS FOR PREDICTED RESPONSE

STATION	α	β (CM./DAY)	γ (CM.)	PROP. VAR.
1	.625	$-.336 \times 10^{-2}$	1.450	.168
4	.621	$-.251 \times 10^{-2}$	1.095	.170
5	.603	$-.941 \times 10^{-3}$.410	.362
6	.599	$.655 \times 10^{-4}$	-.017	.261
7	.572	$.910 \times 10^{-3}$	-.377	.431
9	.540	$-.121 \times 10^{-2}$.529	.360
10	.534	$-.101 \times 10^{-2}$.440	.539
14	.801	$-.253 \times 10^{-2}$	1.080	.408
17	.975	$-.105 \times 10^{-2}$.445	.565
19	1.008	$-.866 \times 10^{-2}$.349	.262

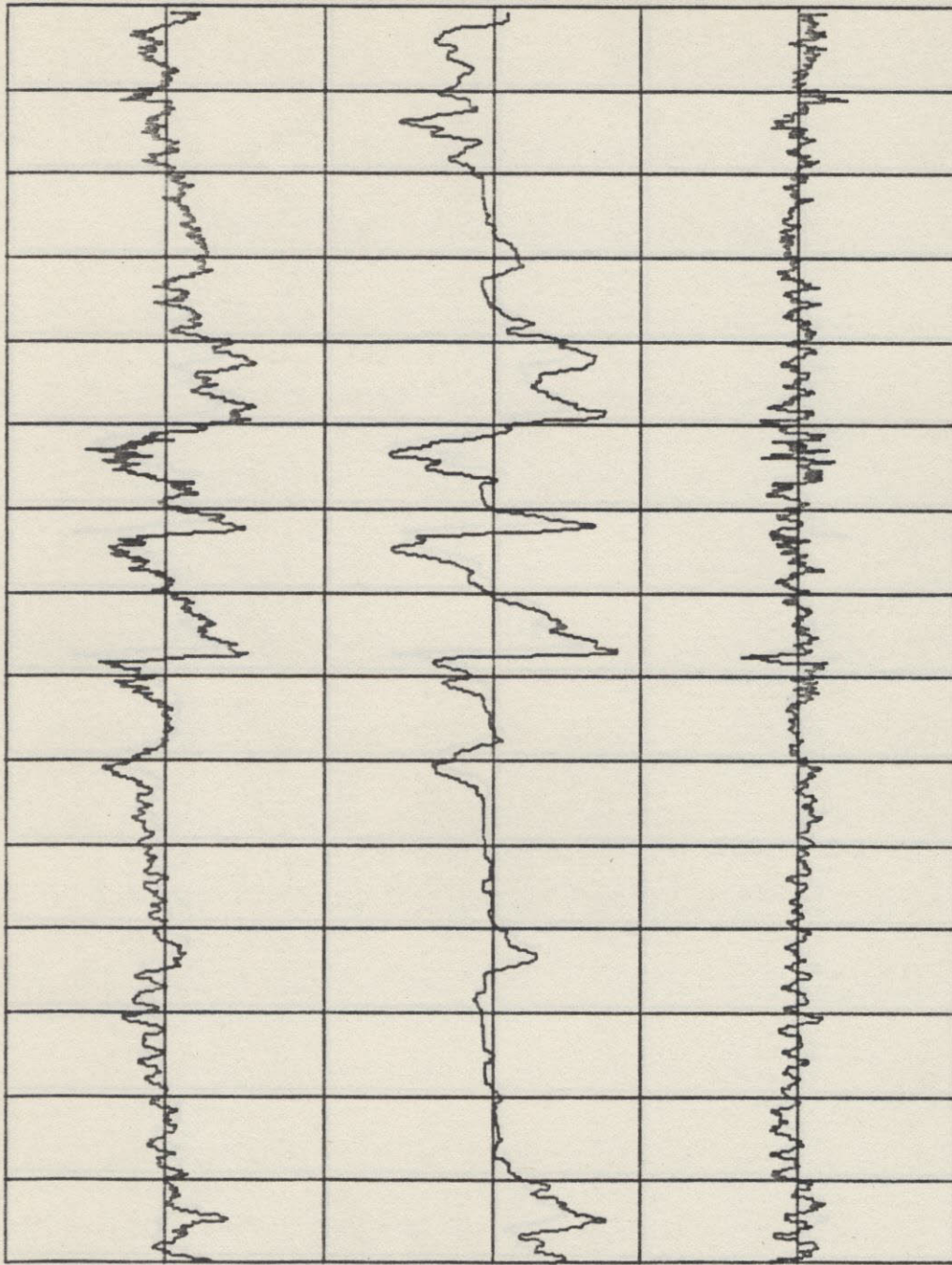
TABLE III

FIGURES 6-13 TO 6-22

Measured elevation minus predicted elevation due to entrance forcing; predicted elevation due to wind alone; and difference between measured elevation due to wind and best fit of predicted elevation due to wind.

Elevations are scaled from -36cm to +36cm.
Vertical lines are drawn at 2-day intervals.

STATION 1



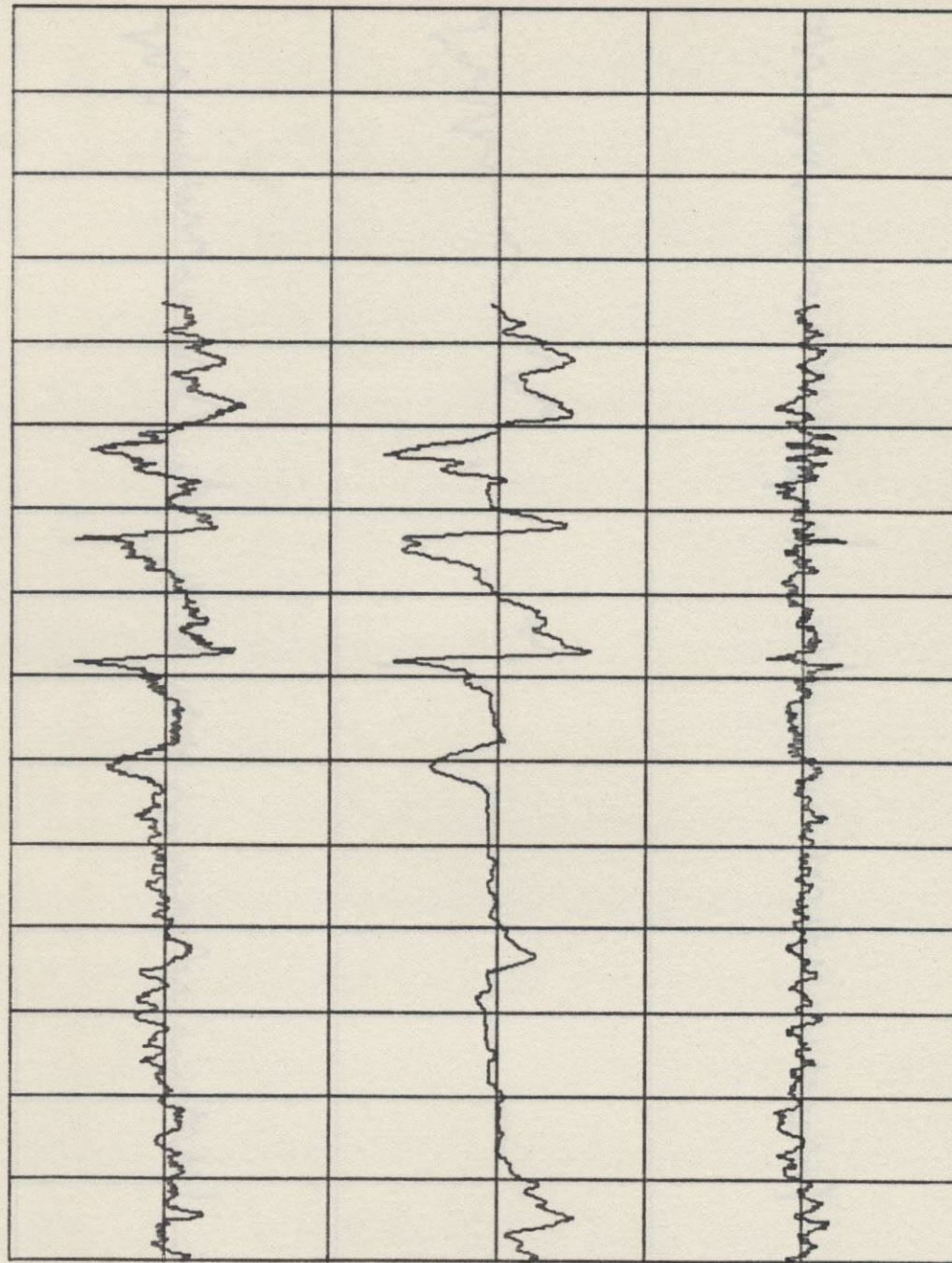
(A) MEAS. ELEV.
MINUS EFFECT
OF ζ_0

(B) PREDICTED
ELEVATION
DUE TO WIND

(A) - BEST
FIT VERSION
OF (B)

FIGURE 6-13

STATION 4



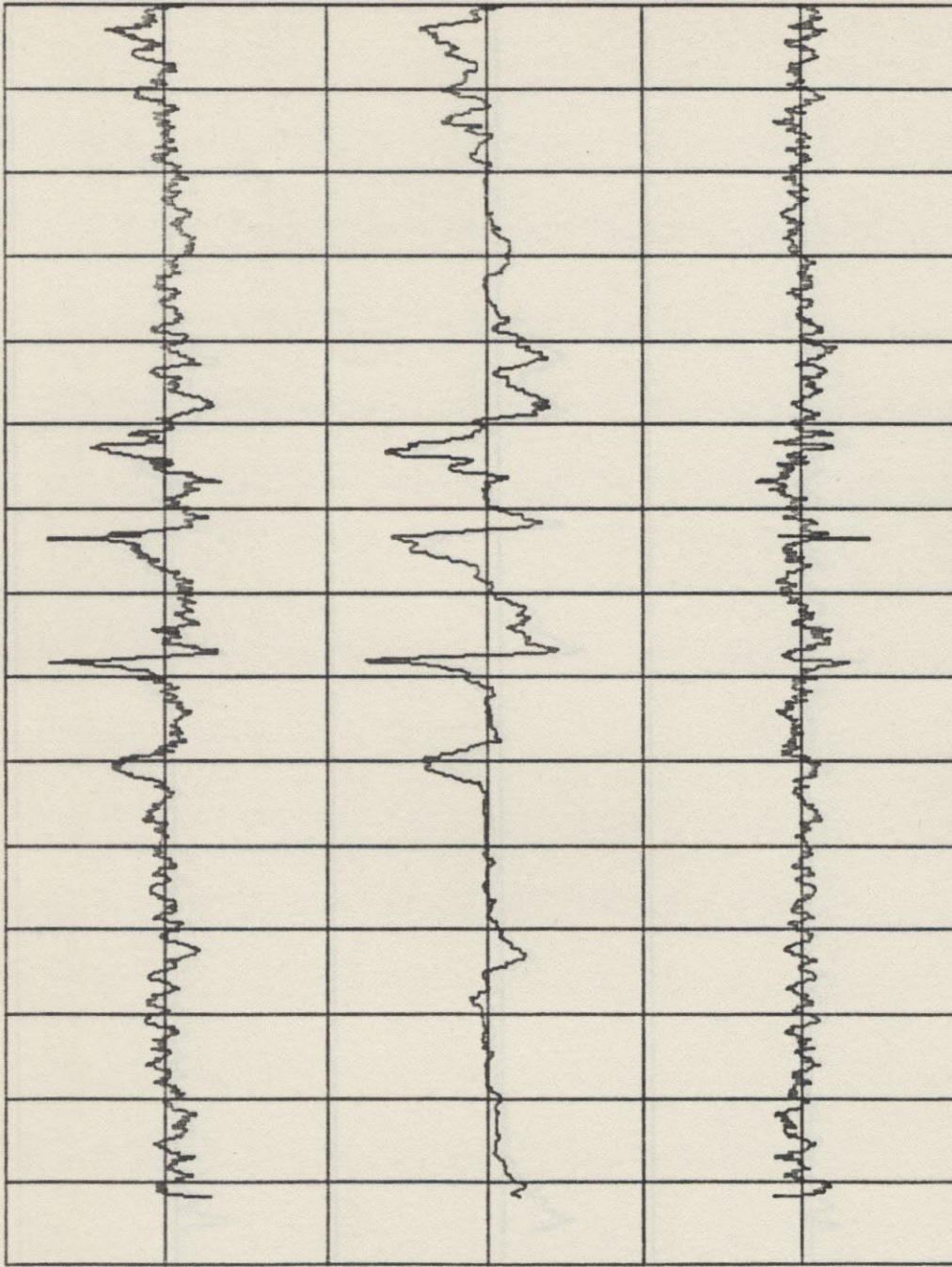
(A) MEAS. ELEV.
MINUS EFFECT
OF z_0

(B) PREDICTED
ELEVATION
DUE TO WIND

(A) - BEST
FIT VERSION
OF (B)

FIGURE 6-14

STATION 5



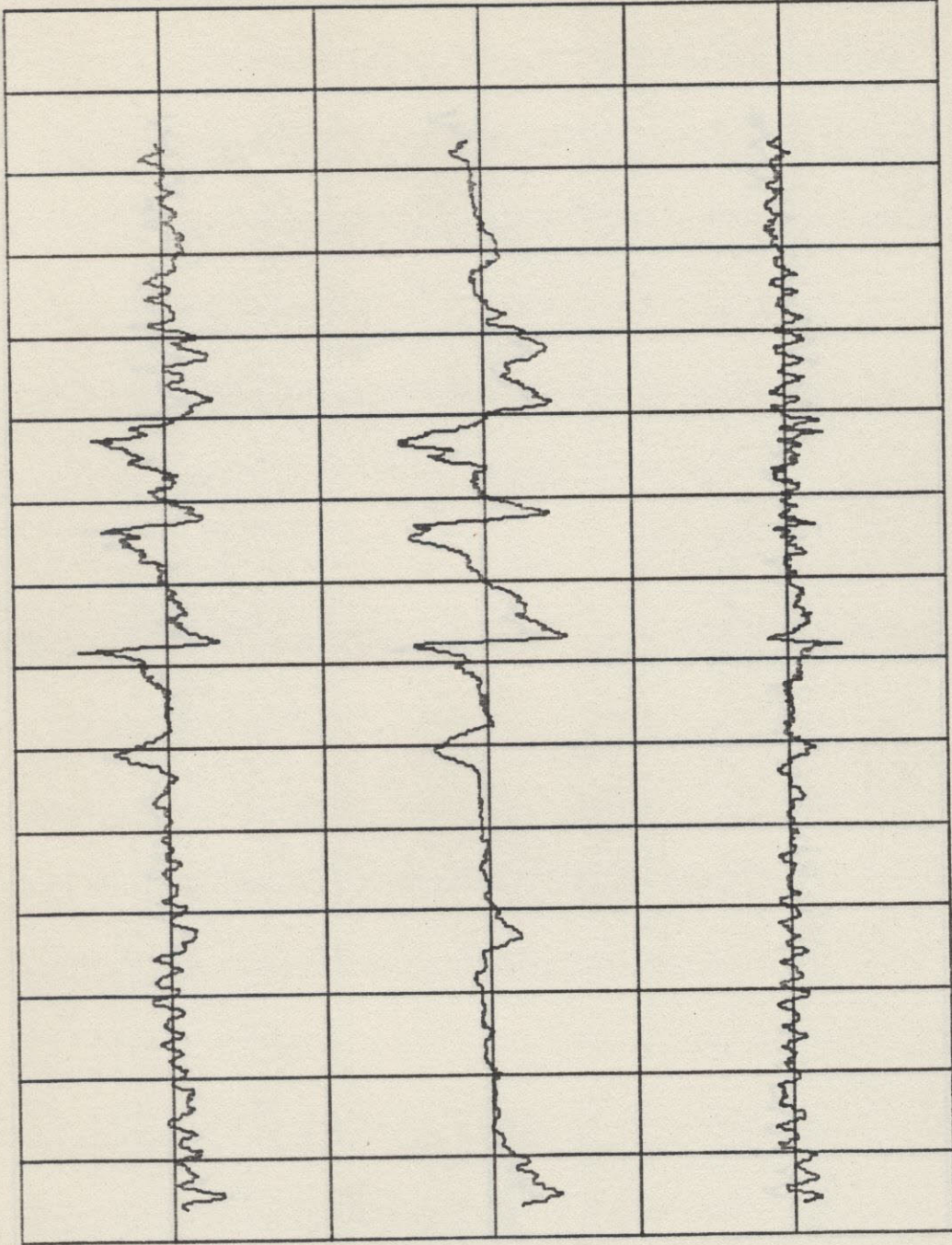
(A) MEAS. ELEV.
MINUS EFFECT
OF z_0

(B) PREDICTED
ELEVATION
DUE TO WIND

(A) - BEST
FIT VERSION
OF (B)

FIGURE 6-15

STATION 6



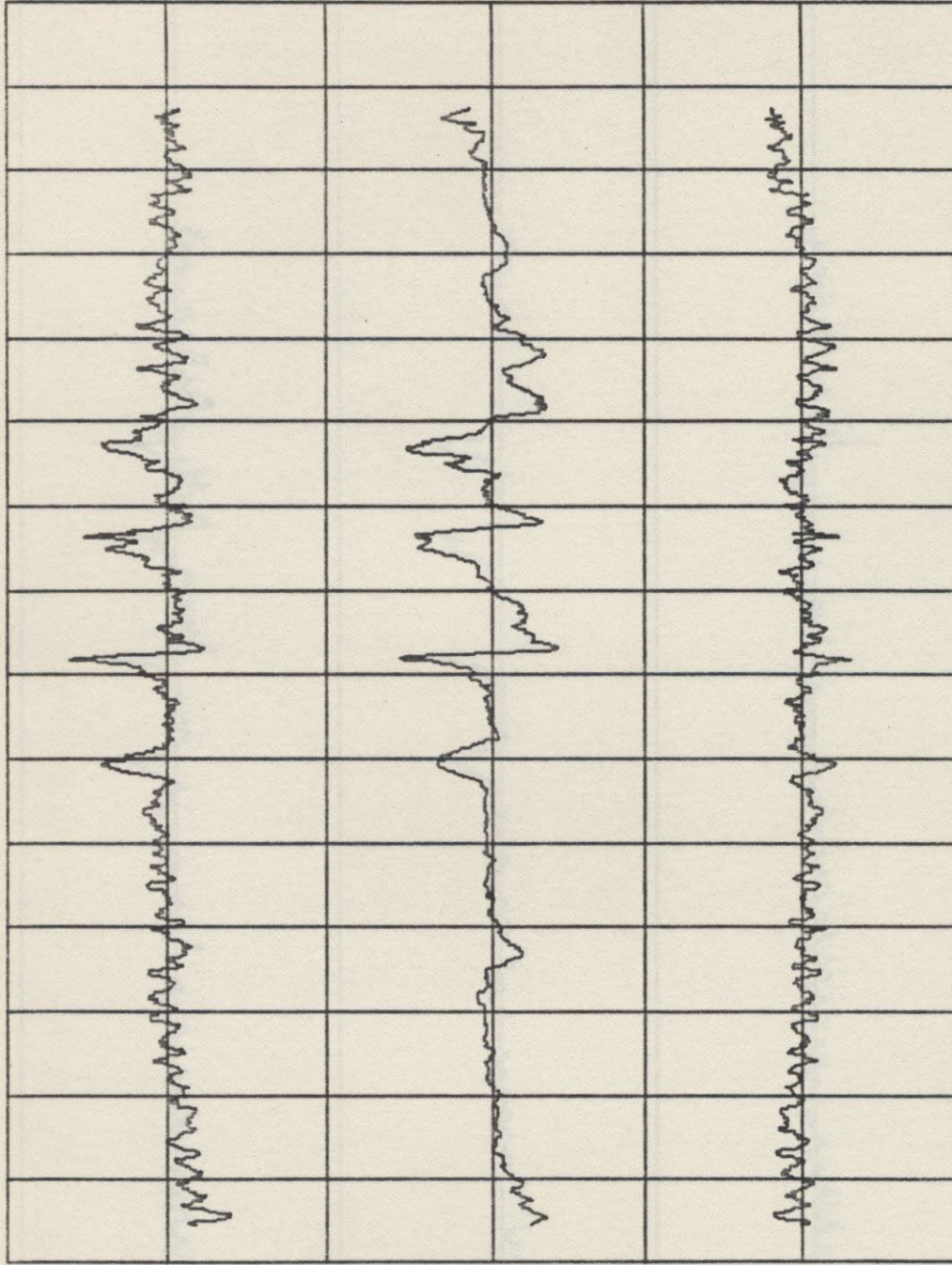
(A) MEAS. ELEV.
MINUS EFFECT
OF ζ_0

(B) PREDICTED
ELEVATION
DUE TO WIND

(A) - BEST
FIT VERSION
OF (B)

FIGURE 6-16

STATION 7



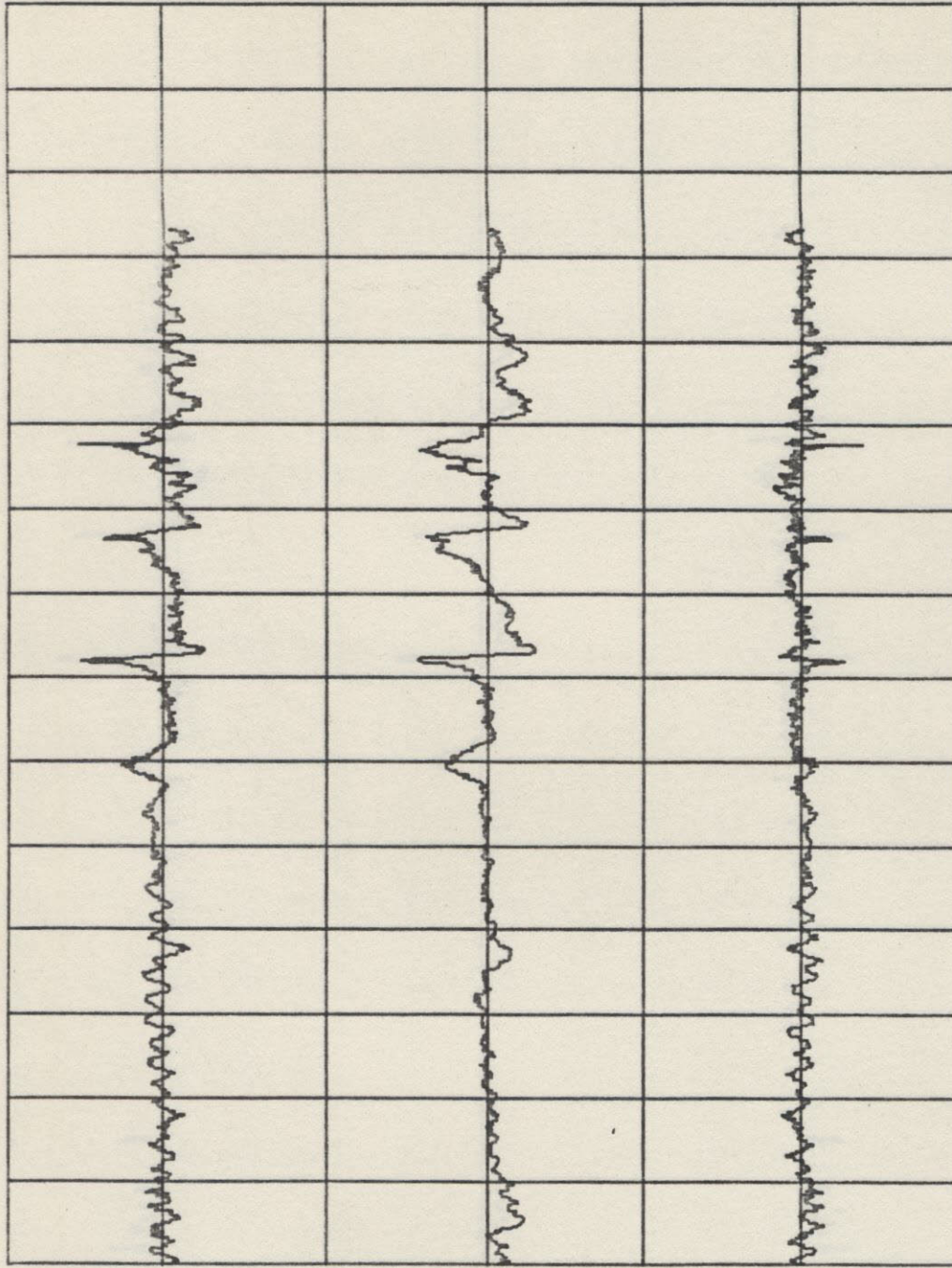
(A) MEAS. ELEV.
MINUS EFFECT
OF z_0

(B) PREDICTED
ELEVATION
DUE TO WIND

(A) - BEST
FIT VERSION
OF (B)

FIGURE 6-17

STATION 9



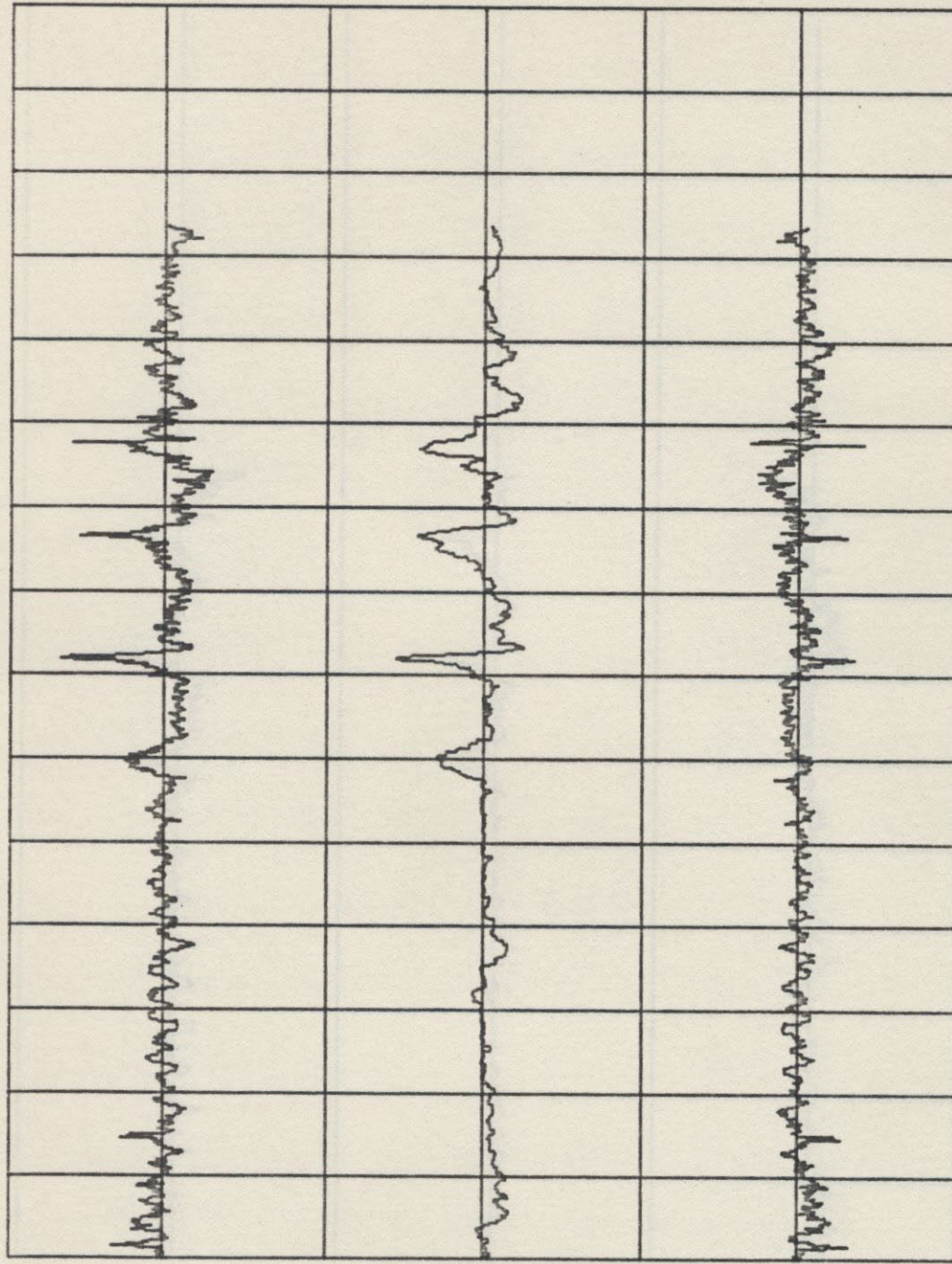
(A) MEAS. ELEV.
MINUS EFFECT
OF z_0

(B) PREDICTED
ELEVATION
DUE TO WIND

(A) - BEST
FIT VERSION
OF (B)

FIGURE 6-18

STATION 10



(A) MEAS. ELEV.
MINUS EFFECT
OF z_0

(B) PREDICTED
ELEVATION
DUE TO WIND

(A) - BEST
FIT VERSION
OF (B)

FIGURE 6-19

STATION 14

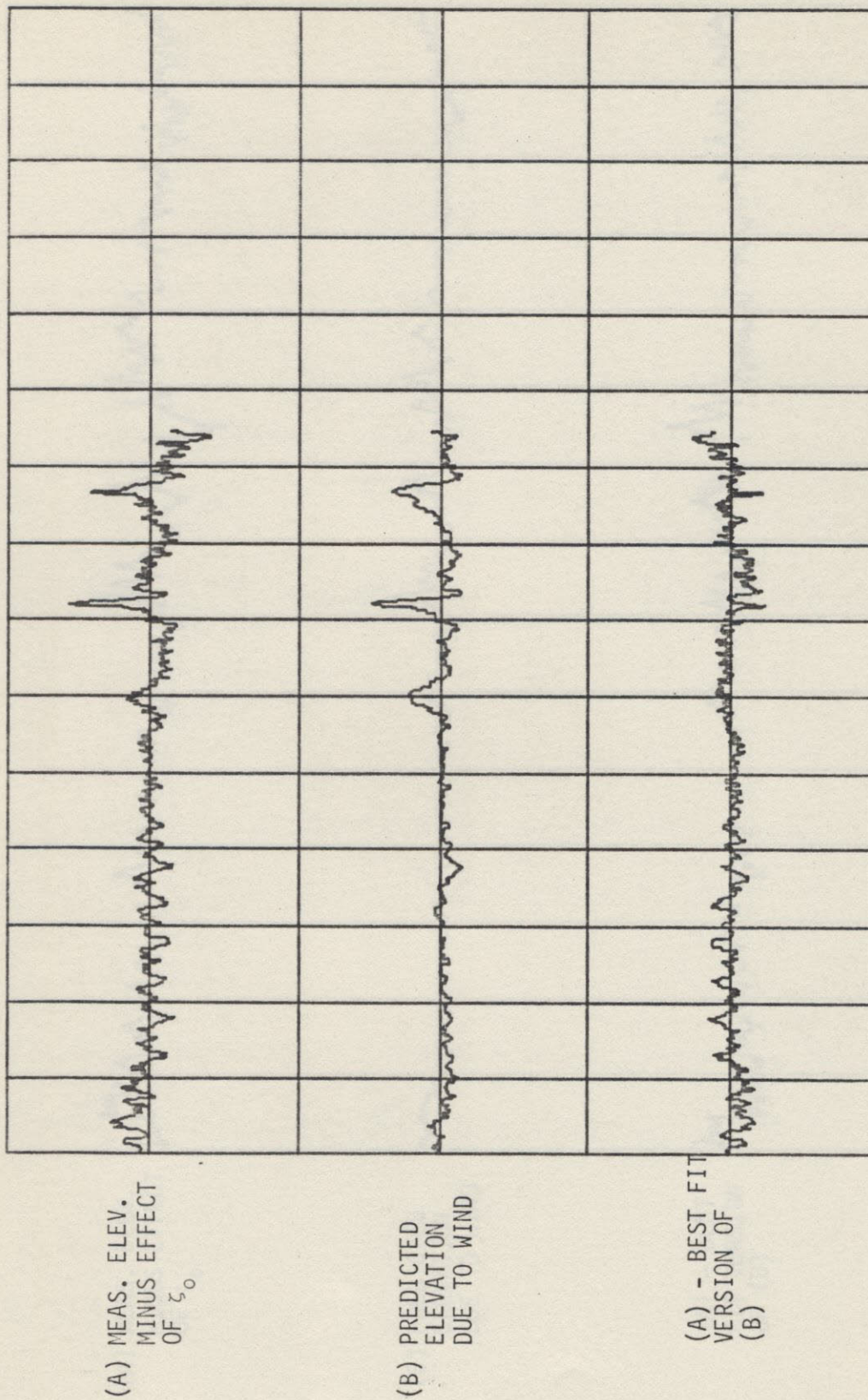
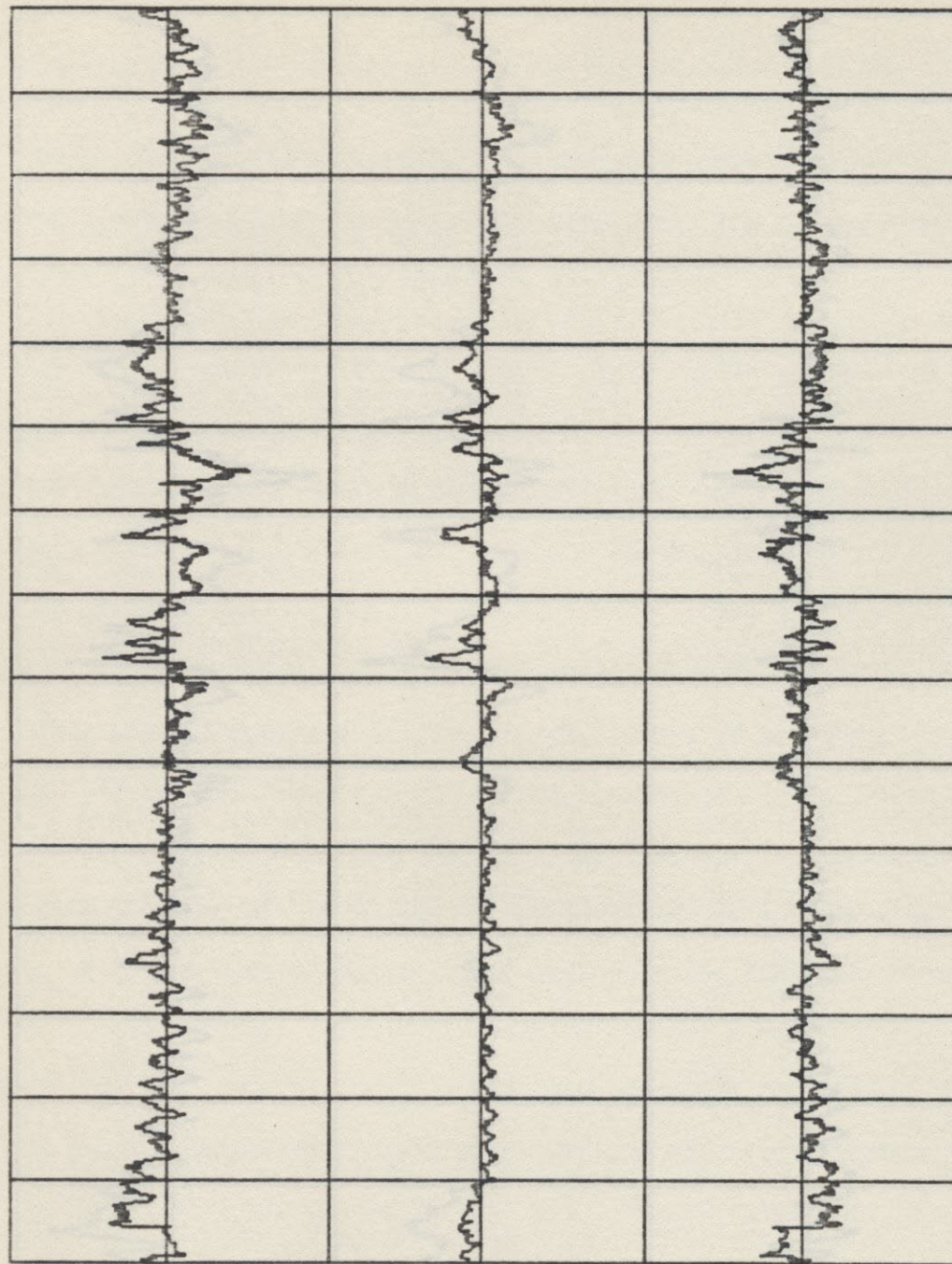


FIGURE 6-20

STATION 17



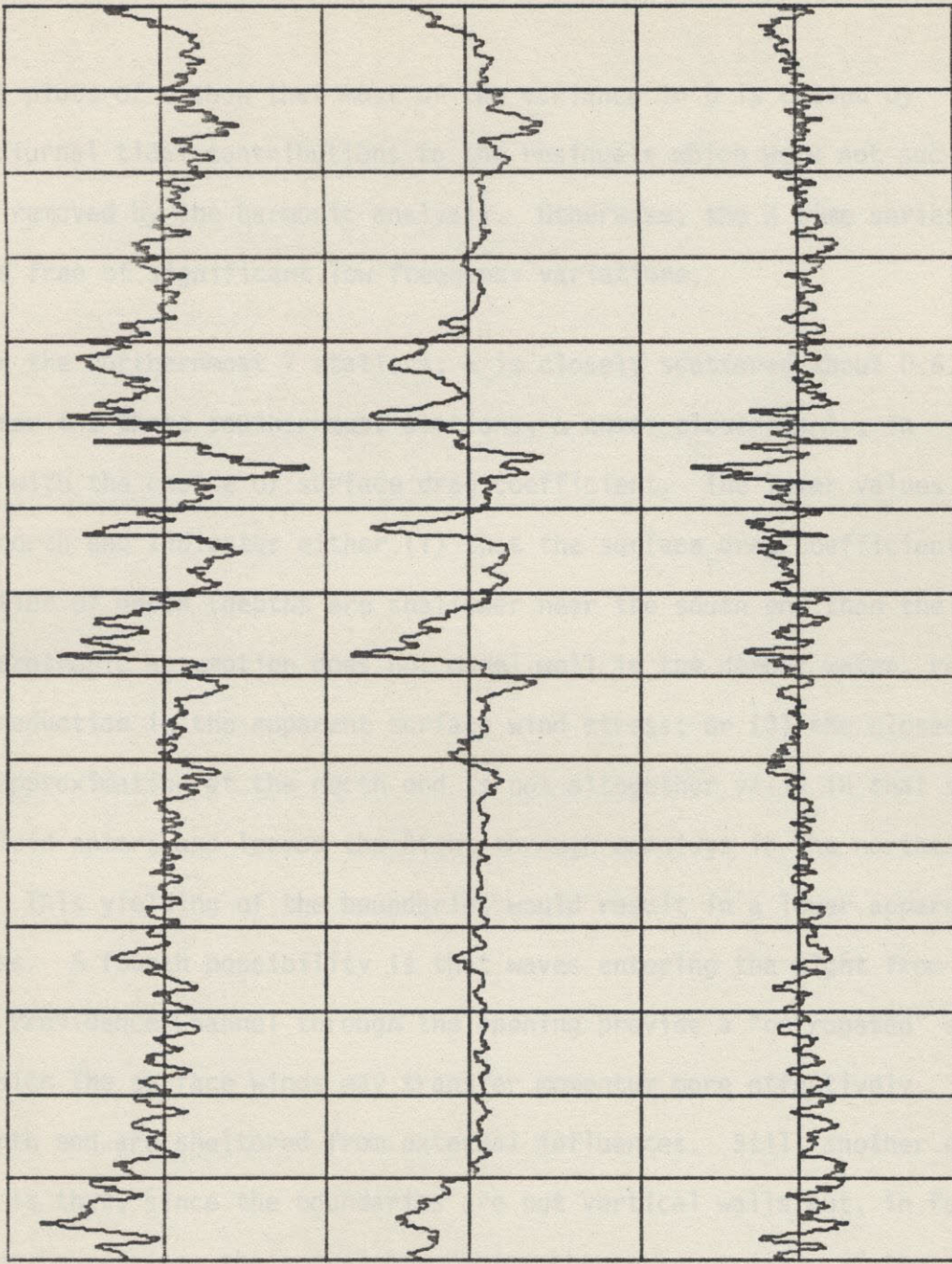
(A) MEAS. ELEV.
MINUS EFFECT
OF z_0

(B) PREDICTED
ELEVATION
DUE TO WIND

(A) - BEST
FIT VERSION
OF (B)

FIGURE 6-21

STATION 19



(A) MEAS. ELEV.
MINUS EFFECT
OF z_0

(B) PREDICTED
ELEVATION
DUE TO WIND

(A) - BEST
FIT VERSION
OF (B)

FIGURE 6-22

The plots of δ show that most of the variance in B is caused by the semi-diurnal tidal contributions to the residuals which were not successfully removed by the harmonic analysis. Otherwise, the δ time series seem to be free of significant low frequency variations.

For the northernmost 7 stations, α is closely scattered about 0.6. However, for the three southernmost stations, α comes closer to 1., in agreement with the choice of surface drag coefficient. The lower values of α at the north end indicates either (1) that the surface drag coefficient may be a function of depth (depths are shallower near the south end than the north); (2) the barotropic assumption does not model well in the deeper water, resulting in a reduction in the apparent surface wind stress; or (3) the closed boundary approximation at the north end is not altogether valid in that some outside fluid enters and leaves the Bight through openings in the northern boundary. This yielding of the boundaries would result in a lower apparent wind stress. A fourth possibility is that waves entering the Bight from the Northwest Providence Channel through the opening provide a "corrugated" surface through which the surface winds may transfer momentum more effectively. Waters in the north end are sheltered from external influences. Still another explanation is that, since the boundaries are not vertical walls but, in fact, are sloping boundaries, the actual boundaries change appreciably if the surface elevations change sufficiently. Accordingly, it should be noted that, in Figure 6-13, the over-predictions occur during strong winds and periods of large displacement in elevation.

SECTION 7

COMPARISON OF METHODS

In the present section the normal mode technique is compared with the time stepping method at the admittance function level. Three admittance functions are defined: $H_{\zeta_0}(\vec{x}, \omega)$, $H_{\tau_x}(\vec{x}, \omega)$, and $H_{\tau_y}(\vec{x}, \omega)$, the transforms of the impulse response functions, $K_{\zeta_0}(\vec{x}, t)$, $K_{\tau_x}(\vec{x}, t)$, and $K_{\tau_y}(\vec{x}, t)$. Partition $\zeta(\vec{x}, t)$, so that,

$$\zeta(\vec{x}, t) = \zeta_{\zeta_0}(\vec{x}, t) + \zeta_{\tau_x}(\vec{x}, t) + \zeta_{\tau_y}(\vec{x}, t) \quad , \quad (7-1)$$

where the three terms on the right are the responses to the three types of forcing. Expressions for these three terms were derived in Section 5 (see Eq.'s (5-8) and (5-9)).

Taking the transforms of Eq.'s (5-8) and (5-9) and using the definitions of the admittance functions above, we get:

$$\zeta_{\zeta_0}(\vec{x}, \omega) = 2\pi H_{\zeta_0}(\vec{x}, \omega) \zeta_0(\omega) \quad , \quad (7-2)$$

$$\zeta_{\tau_x}(\vec{x}, \omega) = 2\pi H_{\tau_x}(\vec{x}, \omega) \tau_x(\omega) \quad , \quad (7-3)$$

$$\zeta_{\tau_y}(\vec{x}, \omega) = 2\pi H_{\tau_y}(\vec{x}, \omega) \tau_y(\omega) \quad . \quad (7-4)$$

On substituting Eq.'s (7-2), (7-3), and (7-4) in Eq. (7-1) and comparing with the Green's theorem, Eq. (3-32), we can relate the admittance function to the normal modes. (For purposes of the comparison, the admittance function, when calculated from normal modes, will be superscripted with a "G".)

$$H_{\zeta_0}^G(\vec{x}, \omega) = \frac{ig}{2\pi} \sum_{n=-\infty}^{\infty} \frac{\zeta_n(\vec{x})}{\omega_n - \omega} \int_B dx' h\tilde{u}_n, \quad (7-5)$$

$$H_{\tau_x}^G(\vec{x}, \omega) = \frac{ig}{2\pi} \sum_{n=-\infty}^{\infty} \frac{\zeta_n(\vec{x})}{\omega_n - \omega} \int_S d^2x' \tilde{u}_n, \quad (7-6)$$

$$H_{\tau_y}^G(\vec{x}, \omega) = \frac{ig}{2\pi} \sum_{n=-\infty}^{\infty} \frac{\zeta_n(\vec{x})}{\omega_n - \omega} \int_S d^2x' \tilde{v}_n. \quad (7-7)$$

$H_{\zeta_0}^G(\vec{x}, \omega)$ is shown in Figure 7-1 for 10 stations. The spectrum for the northernmost stations cuts off at about 20 cycles/day (1.2 hrs.), whereas the frequency cutoff for the central stations is at 36 to 40 cycles/day (36 minutes). 40 cycles is close to the upper limit in frequency which can be supported by the lattice. $H_{\zeta_0}^G(\vec{x}, \omega)$ is plotted in Figure 7-2 for 10 stations. As expected, due to the incomplete collection of zero frequency modes, disagreement is largest at near-zero frequencies and, due to truncation errors, at frequencies above 14 cycles/day. There appears to be a tapering off of the amplitudes of the higher frequencies for the more remote observation stations. Figures 7-3 and 7-4 provide a comparison between $H_{\tau_x}(\vec{x}, \omega)$ and $H_{\tau_x}^G(\vec{x}, \omega)$, and Figures 7-5 and 7-6 compare $H_{\tau_x}(\vec{x}, \omega)$ with $H_{\tau_y}^G(\vec{x}, \omega)$. Since the high frequency cutoff for $H_{\tau_x}(\vec{x}, \omega)$ and $H_{\tau_y}(\vec{x}, \omega)$ is lower than for $H_{\zeta_0}(\vec{x}, \omega)$, the normal modes in Figures 7-4 and 7-6 do a fairly good job of duplicating Figures 7-3 and 7-5.

STATION
NO.

$$\text{Re} \left\{ H_{\zeta_0}(\vec{x}, \omega) \right\}$$

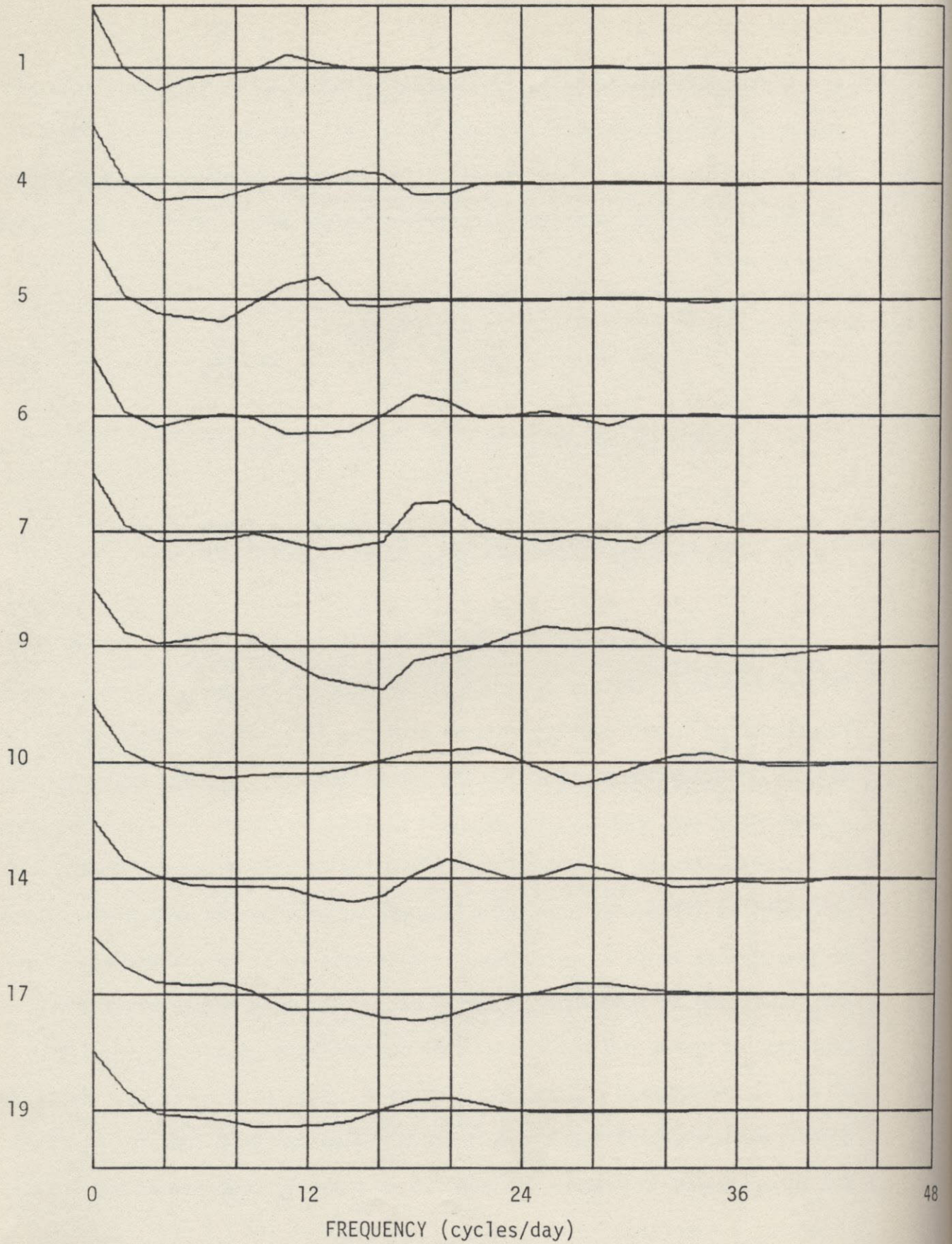


FIGURE 7-1A

STATION
NO.

$$\text{Re} \left\{ H_{\zeta_0}^G(\vec{x}, \omega) \right\}$$

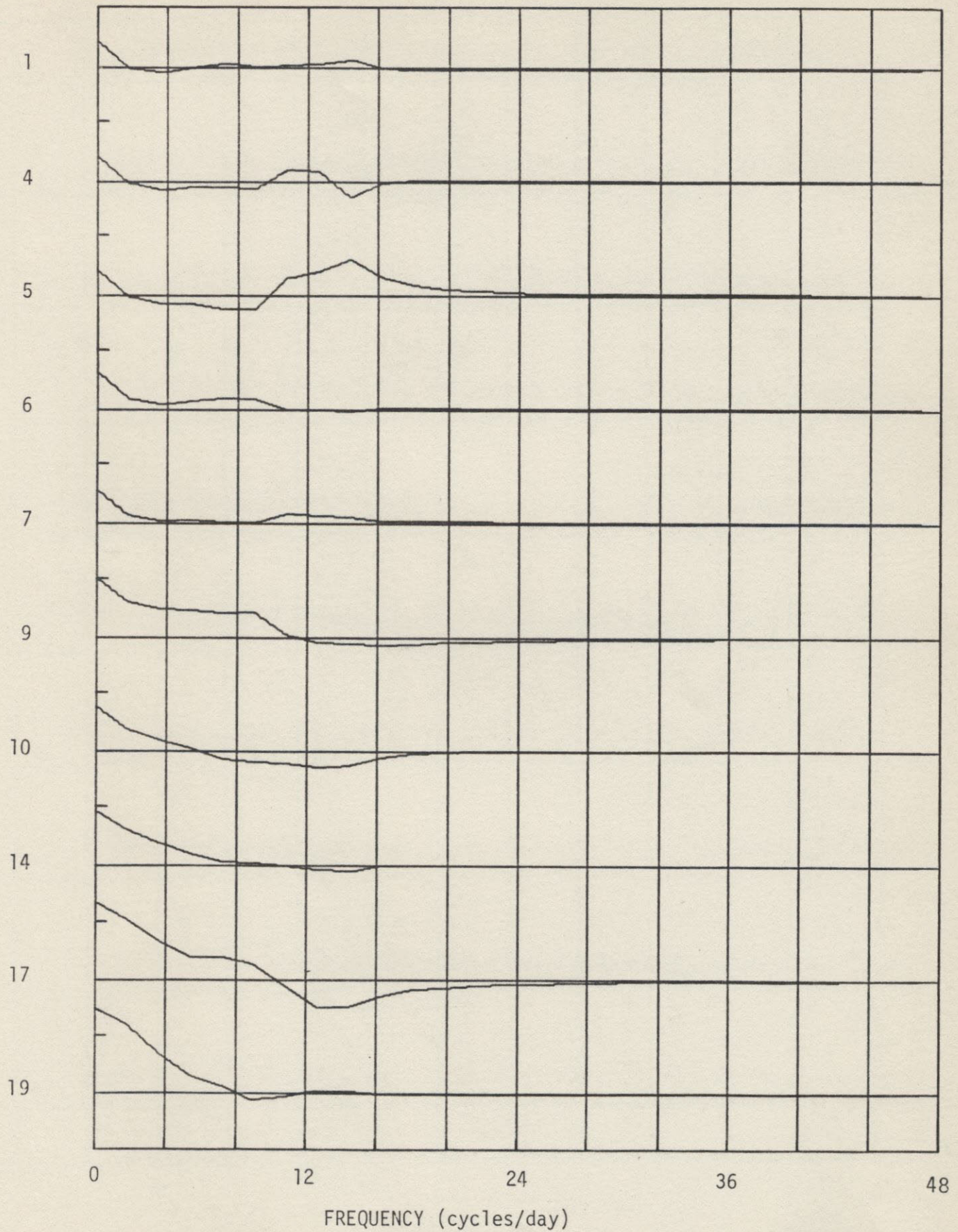


FIGURE 7-2A

STATION
NO.

$$\text{Im} \left\{ H_{\zeta_0}(\vec{x}, \omega) \right\}$$

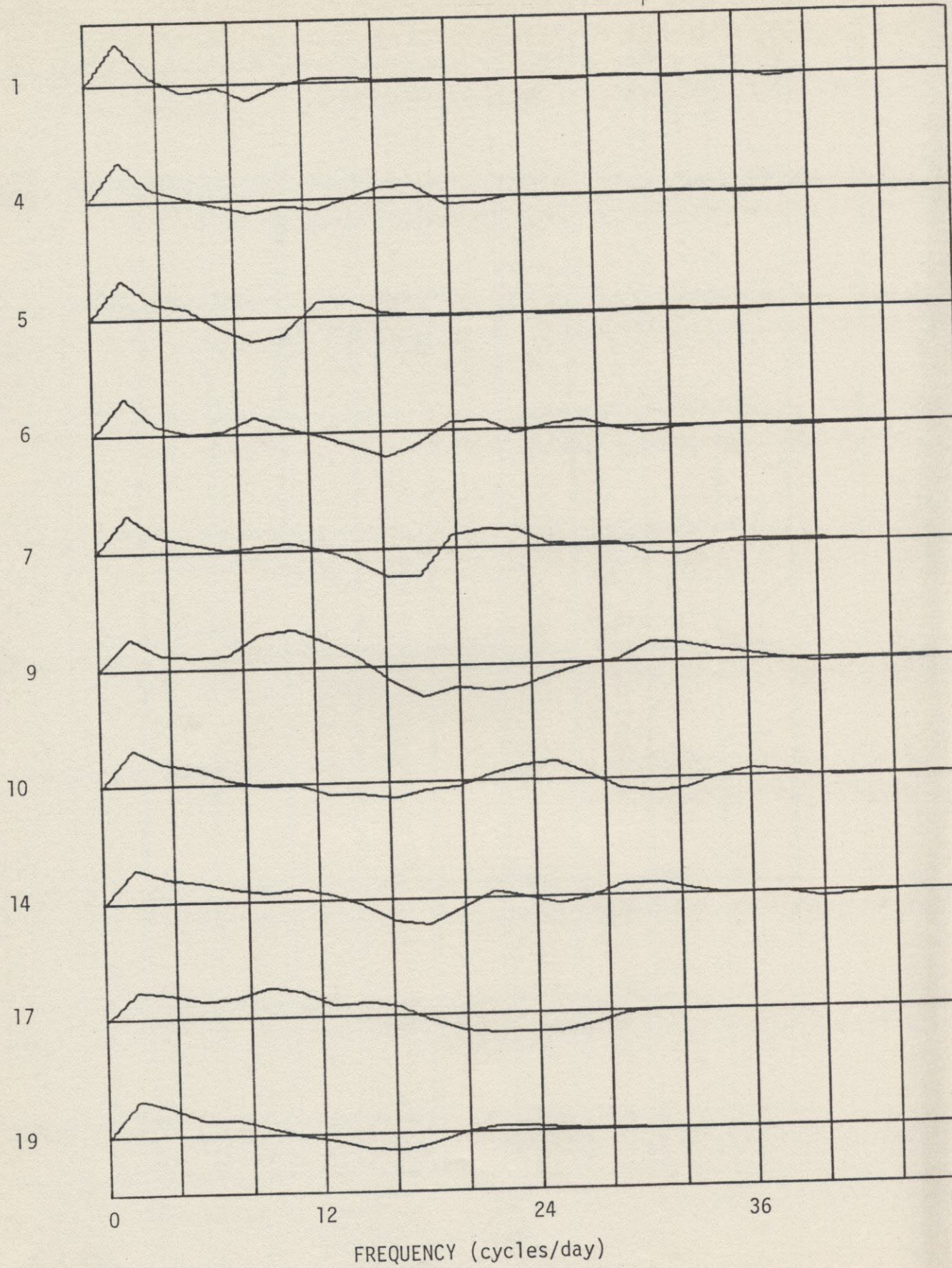


FIGURE 7-1B

STATION
NO.

$$\text{Im} \left\{ H_{\zeta_0}^G(\vec{x}, \omega) \right\}$$

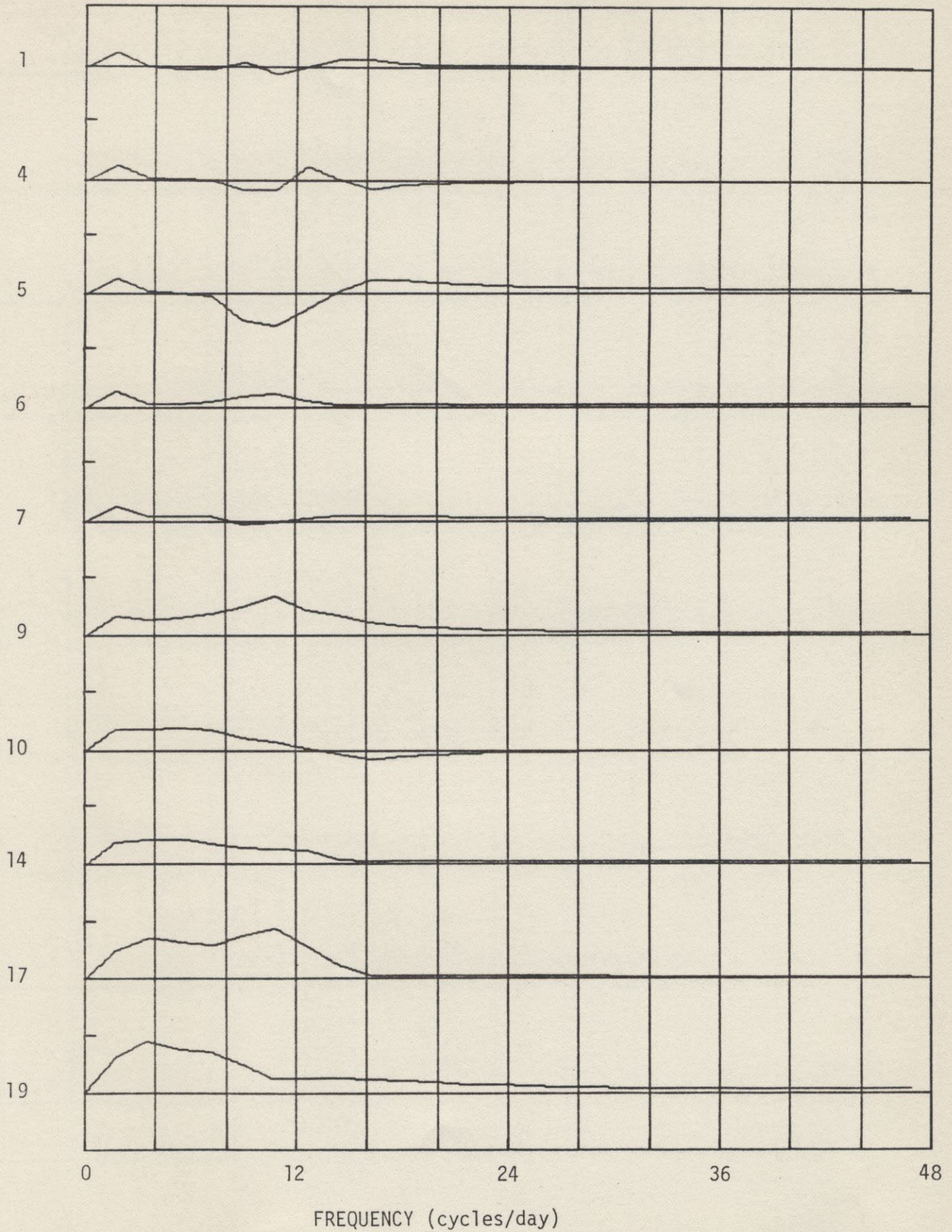
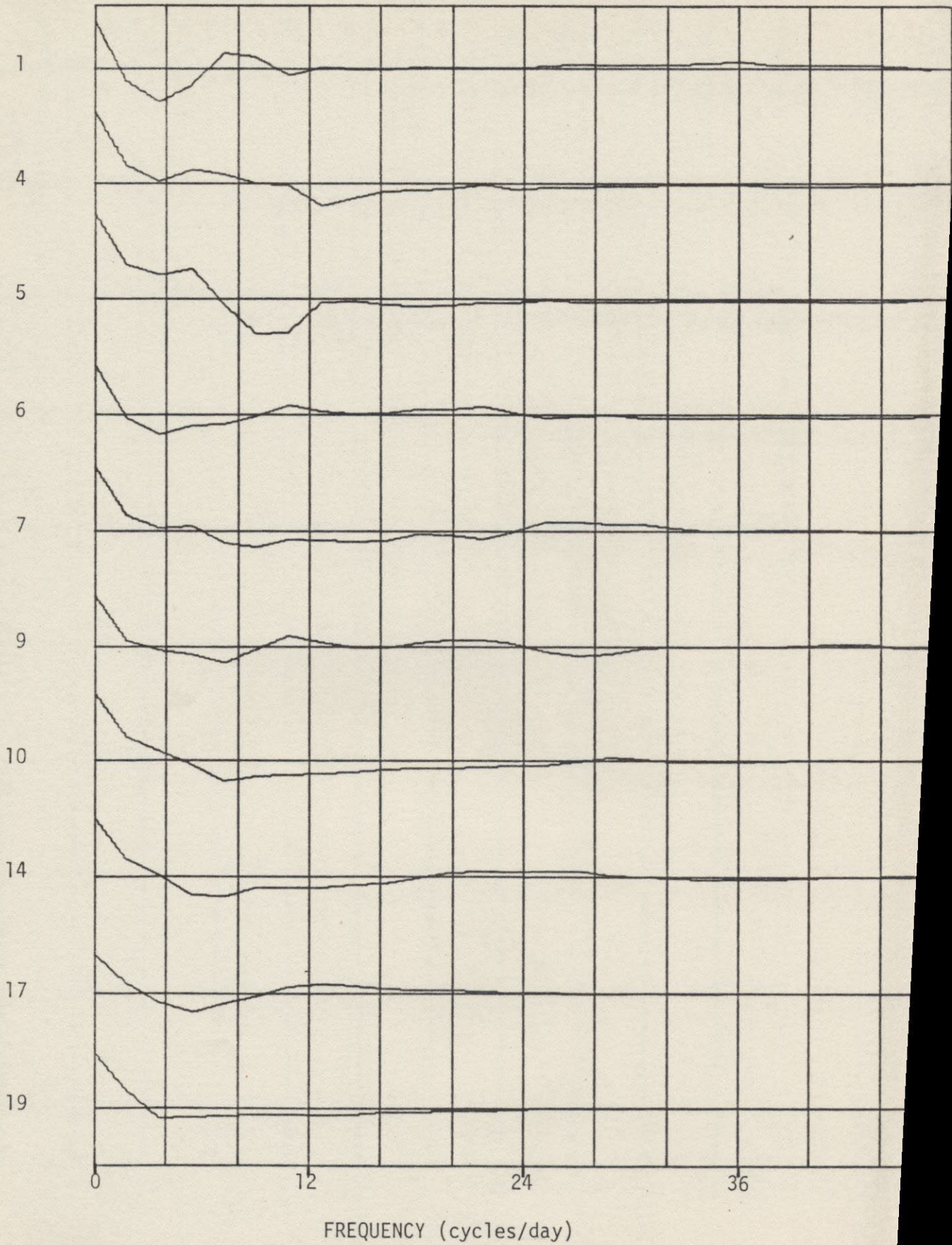


FIGURE 7-2B

STATION
NO.

$$\text{Re} \left\{ H_{\tau_x}(\vec{x}, \omega) \right\}$$



FREQUENCY (cycles/day)

FIGURE 7-3A

STATION
NO.

$$\text{Re} \left\{ H_{\tau_x}^G(\vec{x}, \omega) \right\}$$

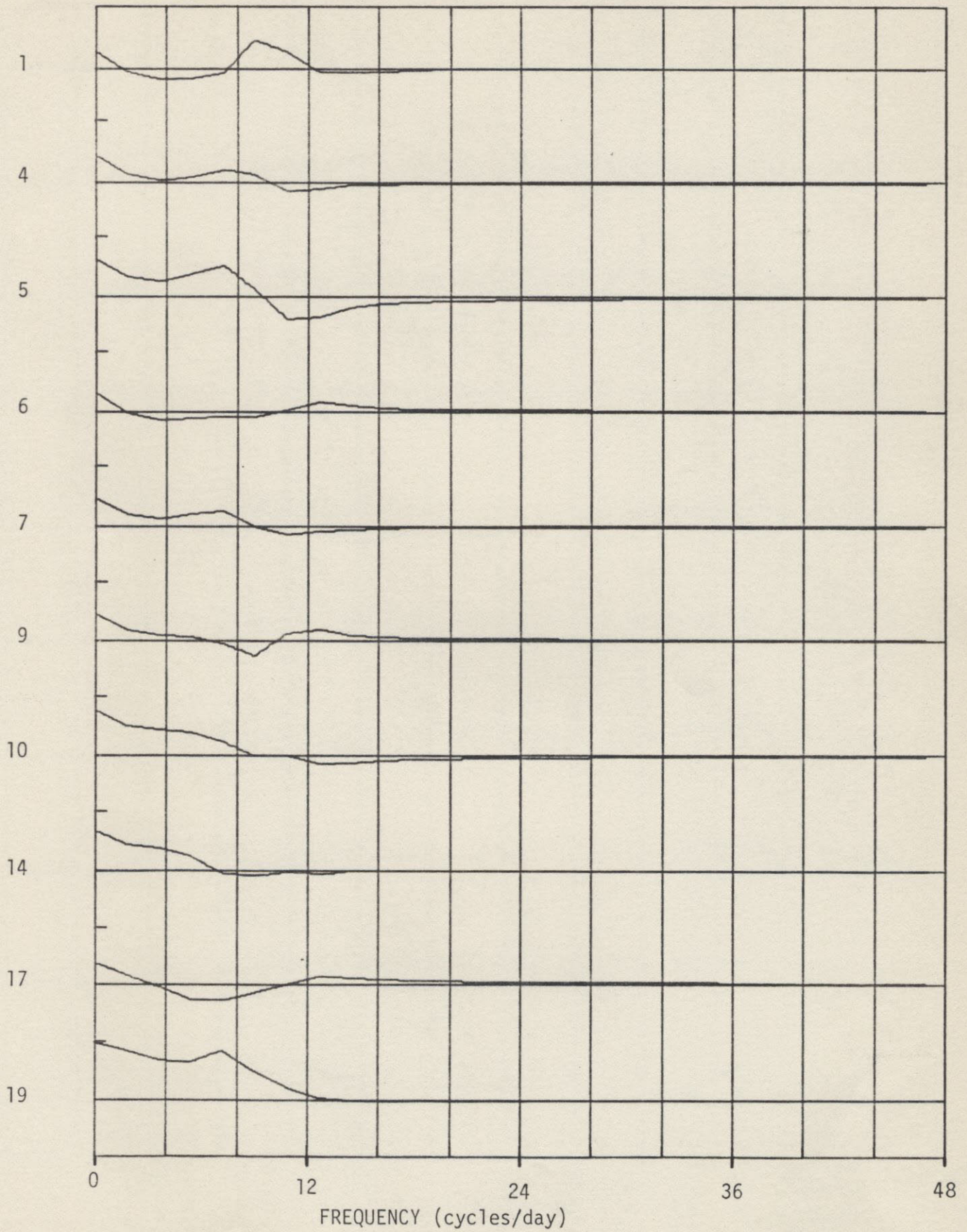


FIGURE 7-4A

STATION
NO.

$$\text{Im} \left\{ H_{\tau_X}(\vec{x}, \omega) \right\}$$

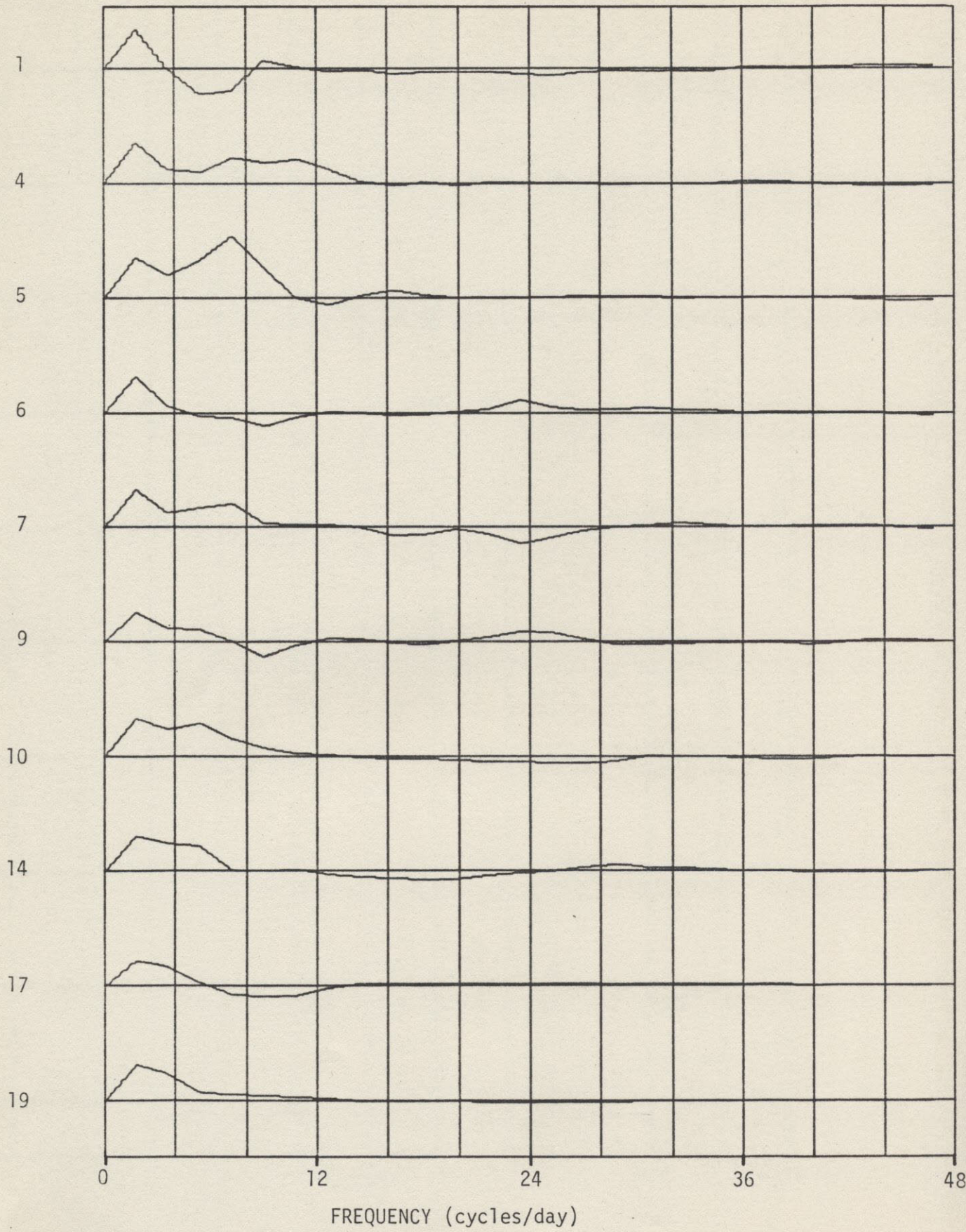


FIGURE 7-3B

STATION
NO.

$$\text{Im} \left\{ H_{\tau_x}^G(\vec{x}, \omega) \right\}$$

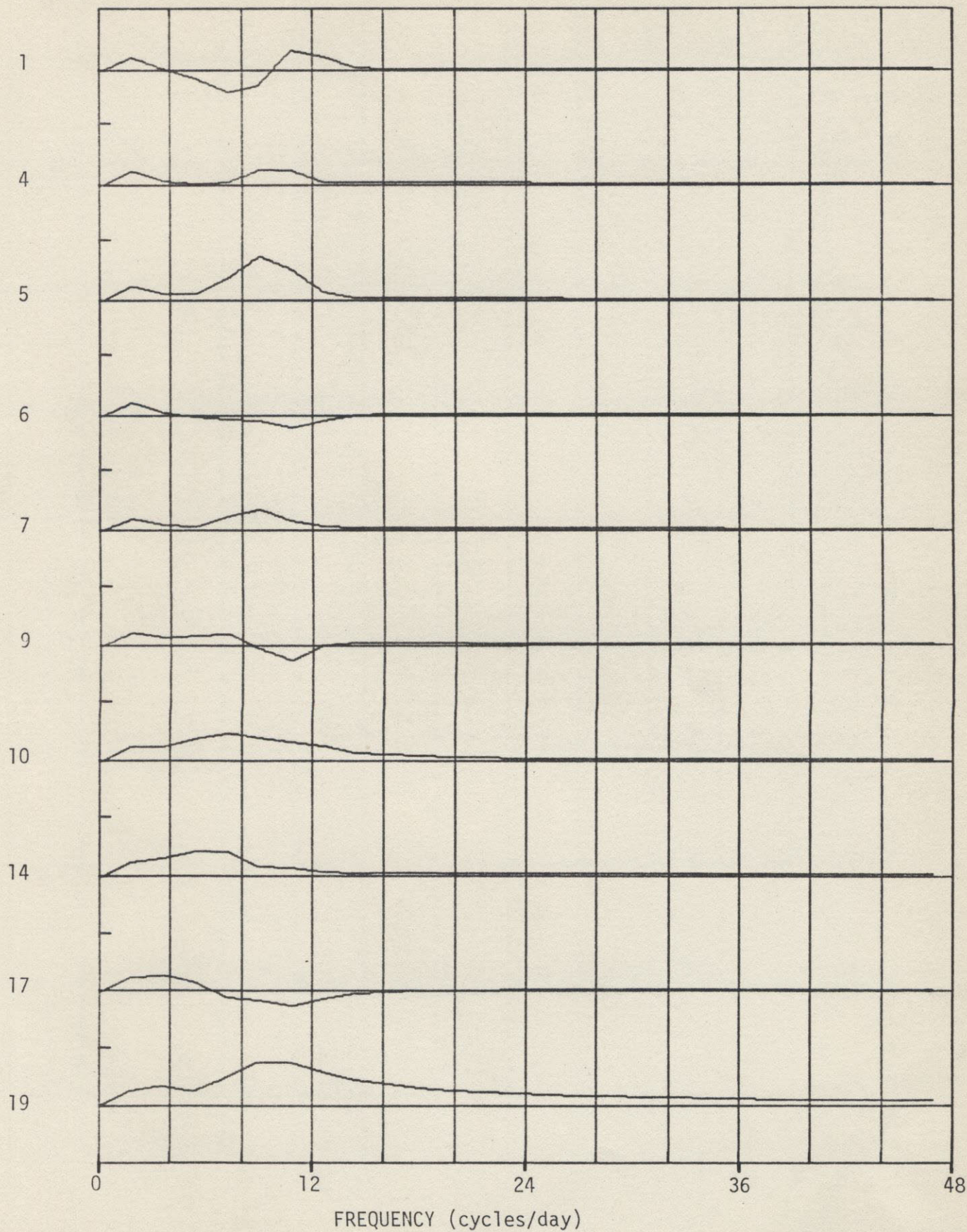


FIGURE 7-4B

STATION
NO.

$$\text{Re} \left\{ H_{\tau_y}(\vec{x}, \omega) \right\}$$

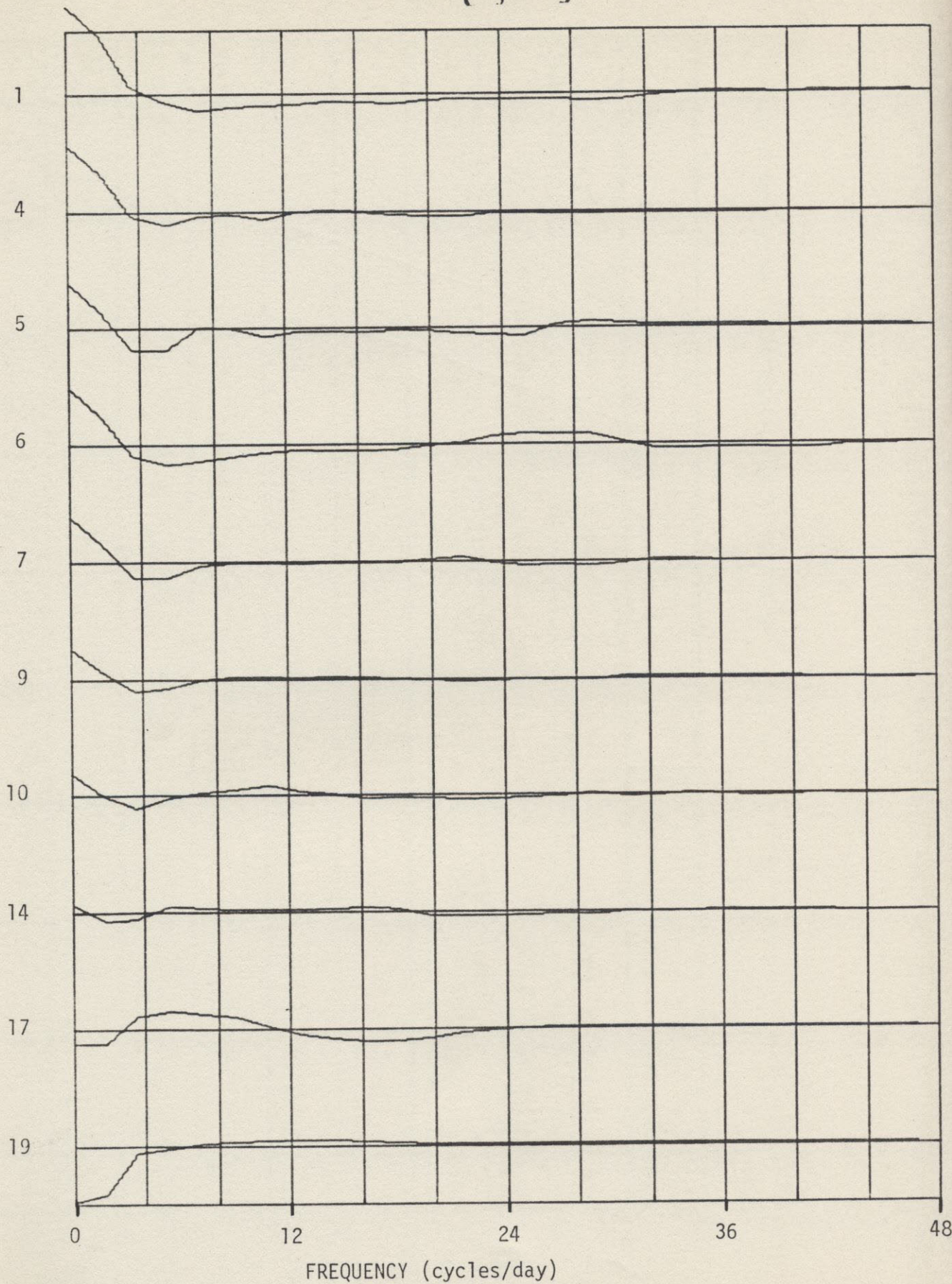
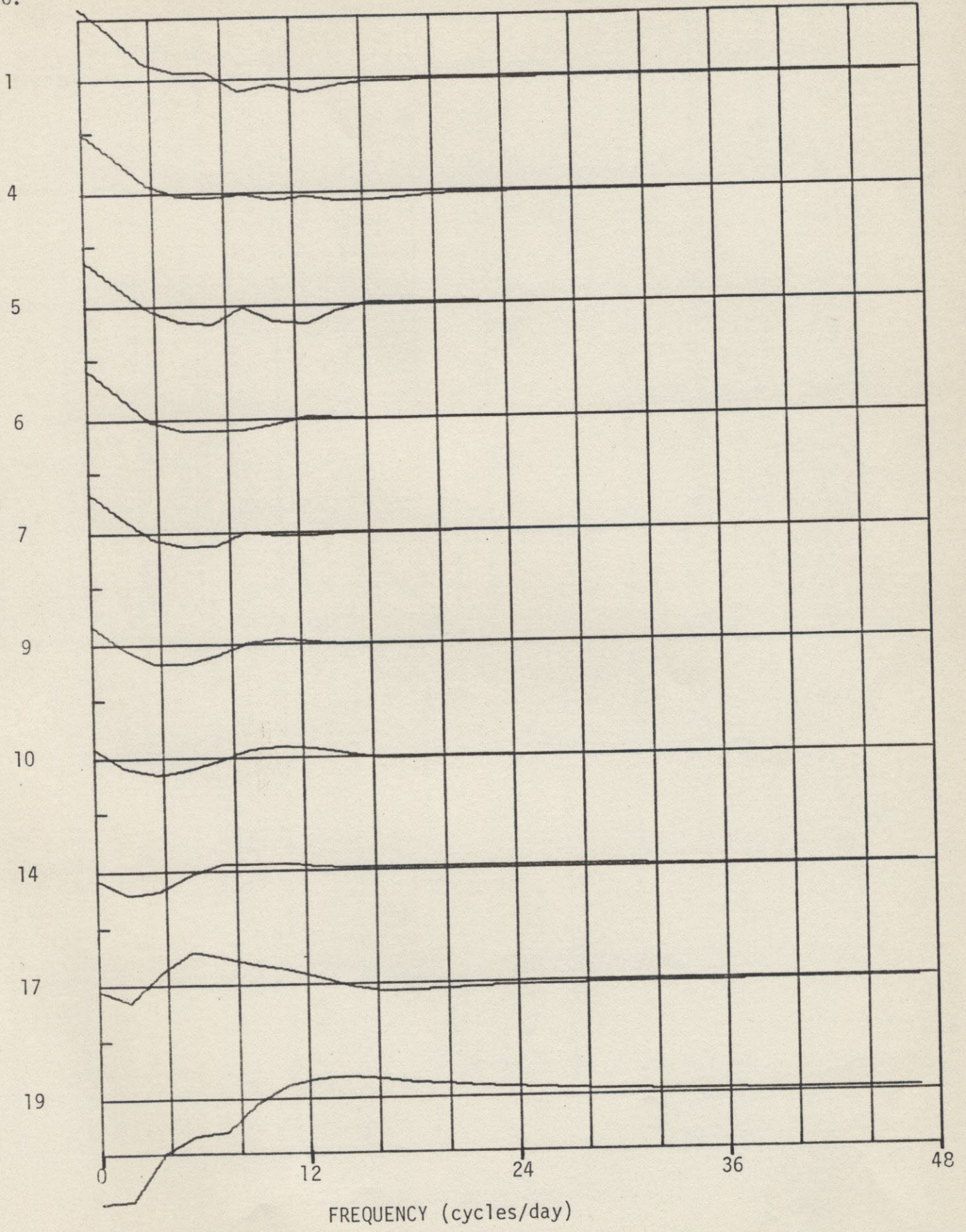


FIGURE 7-5A

STATION
NO.

$$\text{Re} \left\{ H_{\tau_y}^G(\vec{x}, \omega) \right\}$$



FREQUENCY (cycles/day)

FIGURE 7-6A

STATION
NO.

$$\text{Im} \left\{ H_{\tau_y}(\vec{x}, \omega) \right\}$$

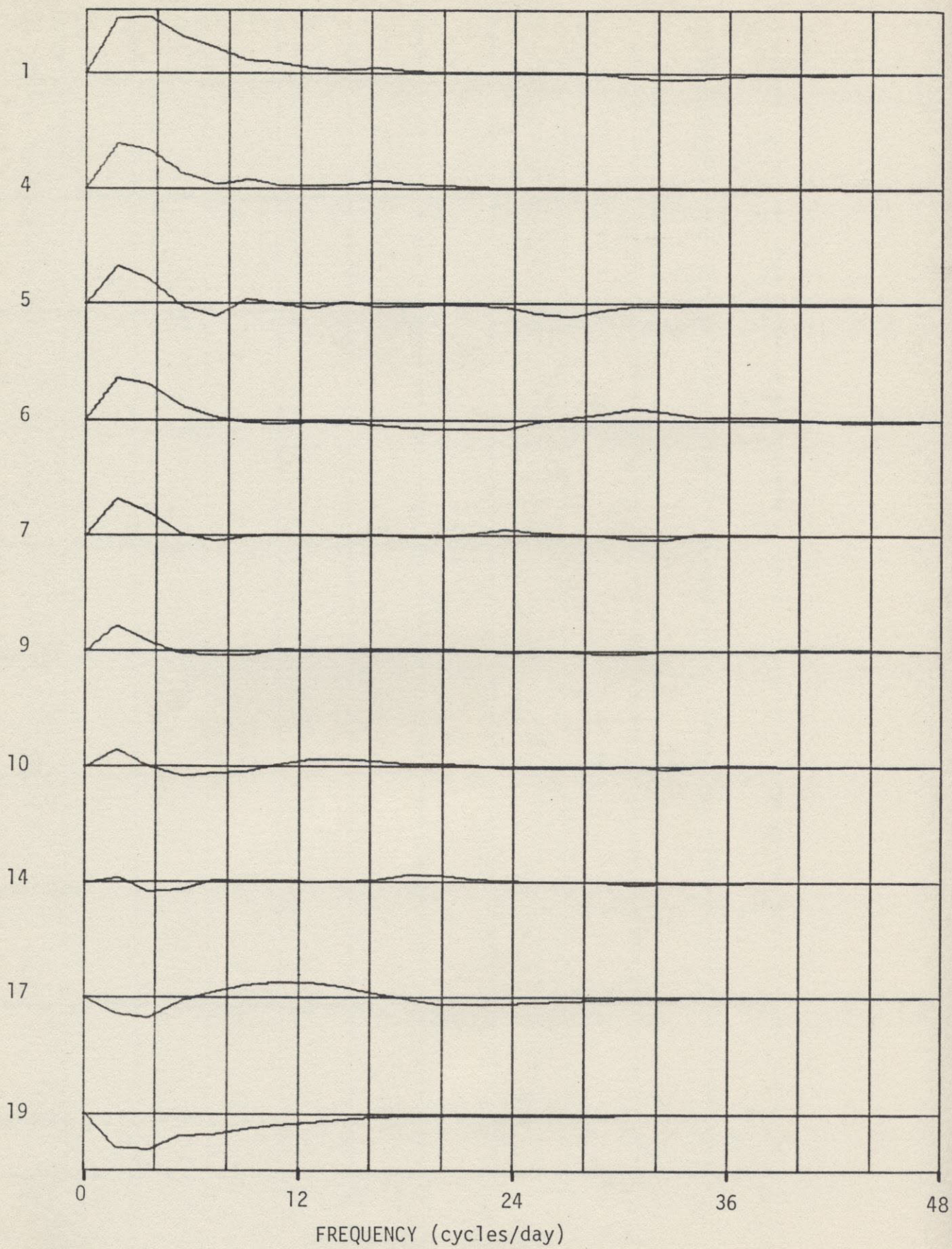


FIGURE 7-5B

STATION
NO.

$$\text{Im} \left\{ H_{\tau_y}^G(\vec{x}, \omega) \right\}$$

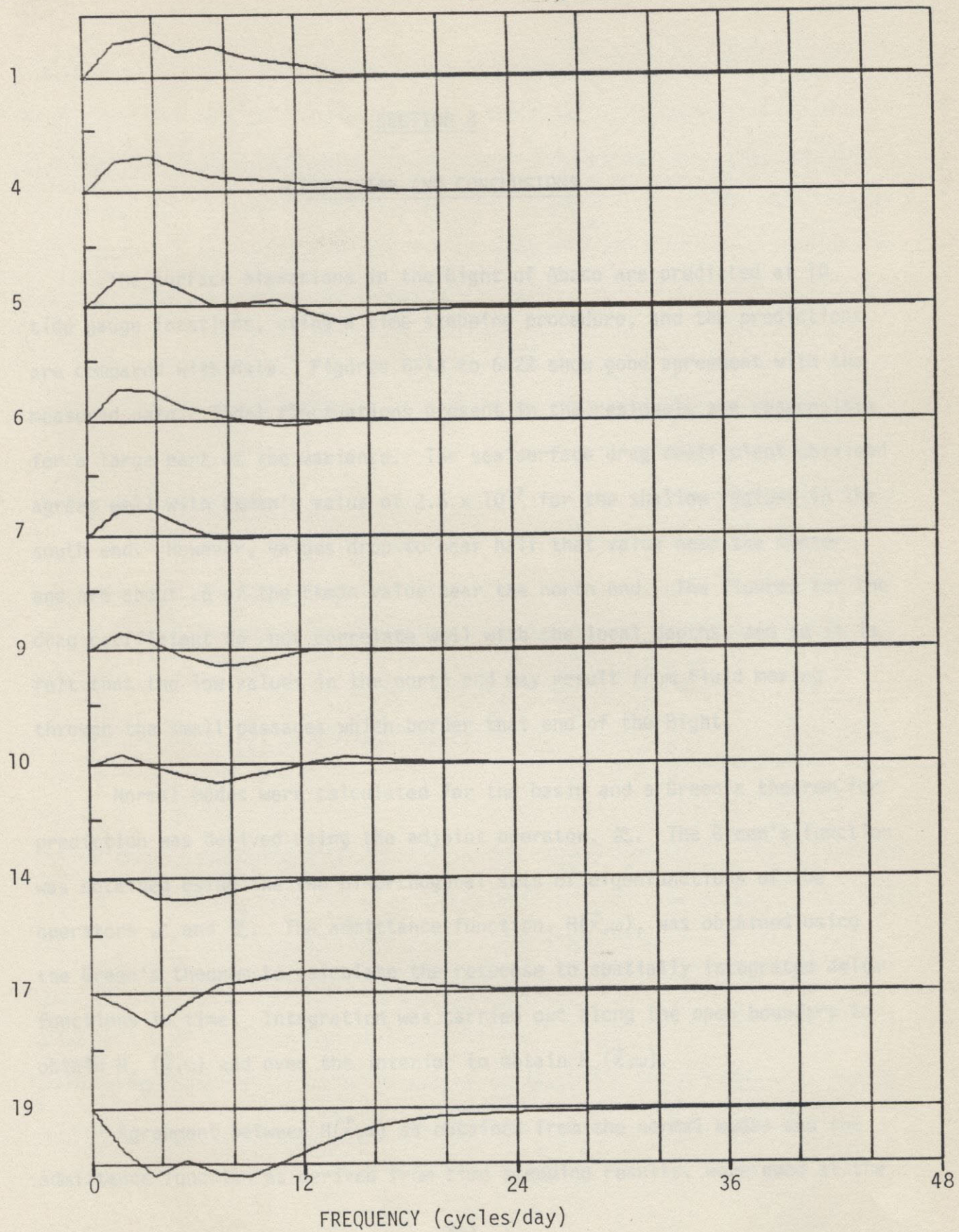


FIGURE 7-6B

SECTION 8

DISCUSSION AND CONCLUSIONS

The surface elevations in the Bight of Abaco are predicted at 10 tide gauge locations, using a time stepping procedure, and the predictions are compared with data. Figures 6-13 to 6-22 show good agreement with the measured data. Tidal fluctuations present in the residuals are responsible for a large part of the variance. The sea surface drag coefficient obtained agrees well with Ekman's value of 2.6×10^{-3} for the shallow regions in the south end. However, values drop to near half that value near the center and are about .6 of the Ekman value near the north end. The figures for the drag coefficient do not correlate well with the local depths, and so it is felt that the low values in the north end may result from fluid moving through the small passages which border that end of the Bight.

Normal modes were calculated for the basin and a Green's theorem for prediction was derived using the adjoint operator, \mathcal{L} . The Green's function was obtained using the two bi-orthogonal sets of eigenfunctions of the operators \mathcal{L} and $\tilde{\mathcal{L}}$. The admittance function, $H(\vec{x}, \omega)$, was obtained using the Green's theorem to calculate the response to spatially integrated delta functions in time. Integration was carried out along the open boundary to obtain $H_{\zeta_0}(\vec{x}, \omega)$ and over the interior to obtain $H_{\tau}(\vec{x}, \omega)$.

Agreement between $H(\vec{x}, \omega)$ as obtained from the normal modes and the admittance function as derived from time stepping results, were good at the

low frequency end of the spectrum for all stations. However, due to the high frequency content of the admittance functions at stations near the opening, the Green's functions did poorly at frequencies above the truncation frequency of about 17 cycles/day. As Figure 7-1 shows, the high frequency tail appearing at stations 9, 10, and 14, close by the opening, disappears at the more remote stations, 1, 4, and 5.

Since the amplitude of the signals present at the remote stations appears to be low pass filtered, it may be hypothesized that any localized disturbance in a shallow basin has its high frequencies attenuated as it moves away from the source region. In order to test this hypothesis, consider an infinite sea excited by an impulse at a point in space, i.e., let the forcing be of the form, $\delta(t)\delta(r)$, in a polar coordinate system. The solution in the frequency domain is the Green's function to the two dimensional wave equation:

$$\zeta(r,\omega) = i\pi H_0^{(1)}(kr) \quad (8-1)$$

Here k is a function of ω and R' , the friction coefficient (see Eq. C-6). All of the ω dependence of ζ resides in the argument of $H_0^{(1)}$. On a spectral plot of $\zeta(r,\omega)$, changing the observation point, r , has the effect of rescaling the frequency axis. Hence, if ζ experiences a cutoff at $\omega = \omega_c$ for $r = D_1$, then at $r = D_2$ the cutoff frequency, ω_c , will take on a different value. In particular, if for a branch of the function, $k = k(R',\omega)$, k is a monotonic increasing function of ω , the effect of increasing r is to lower the cutoff frequency, ω_c . Hence, it is not unreasonable that as one moves away from the source of an impulsive excitation the energy becomes concentrated at

lower frequencies. Since $k(\omega)$, as expressed by Eq. (C-6), is a complex function of ω and is not a simple monotonic function, which direction the scaling of ω takes cannot be determined immediately. Furthermore, the real problem does not involve a constant depth, infinite ocean, but a semi-enclosed basin of variable depth. The basic result that the observed spectrum is a function of the observation point will still hold for the Bight geometry, however. Hence, it is reasonable that stations 1, 4, and 5 in the Bight observe an attenuation of the higher frequencies in relation to observations at stations 9, 10, and 14. That this will be true, in general, for any remote station in any semi-enclosed basin cannot be determined without more extensive analysis.

A disagreement in $H(x,\omega)$ exists for all stations at zero frequency. Theoretically, as shown for the case of a circular basin in Section 4, there exist an infinity of normal modes at zero frequency -- one mode for each $\pm\omega_n$ pair of non-zero frequency modes. Since only 5 of these modes were found, and there exist 10 such modes corresponding to the 10 underdamped modes at non-zero frequency, we have an incomplete picture of the response at $\omega = 0$.

Studies, described in Section 4, of the dependence of the damping factor, ω_j , on R , the drag coefficient, demonstrated some similarities with the zero frequency modes of the constant depth, circular basin, but failed to lead to any systematic method for cataloging these modes. Therefore, further work is necessary if the normal mode method is to be effective for solving the rotating, frictional basin.

An overall goal of this study and that of Snyder et al., (1979) was to determine if a combined model of the tides and the wind set-up in an enclosed basin could be formulated to explain the observed elevations. In particular, this study was intended to test the linearization of the bottom drag term through use of the time-independent tidal coupling factor, $\lambda(\vec{x})$.

The predicted elevations, using the meteorological model described in Section 2, agreed well with observed elevations. Both responses appeared to be quasi-static. It remains a moot question whether this agreement was a result of the particular tidal coupling model used or whether any model, especially one with no tidal coupling at all, would have performed just as well. Since all of the tidal influence is felt through the friction coefficient, $\lambda(\vec{x})$, varying this parameter would test the sensitivity of the model to tidal influence.

As was observed in Section 5, the steady state solution, or quasi-static response, involves a system of gyres and steady currents. Hence, friction must be important at zero frequency to provide an energy sink for the surface wind stress. Hence, in the quasi-static limit, the model for wind set-up should be sensitive to the parameterization of the tides.

APPENDIX A

STATIONARITY OF THE RAYLEIGH RATIO FOR
NON-SELF-ADJOINT OPERATORS

Let \mathcal{L} be a non-self-adjoint operator, and let $\tilde{\mathcal{L}}$ be its adjoint.

Then,

$$\mathcal{L} \psi_n = \omega_n \psi_n \quad (\text{A-1})$$

and

$$\tilde{\mathcal{L}} \tilde{\psi}_n = \omega_n^* \tilde{\psi}_n \quad (\text{A-2})$$

(ψ_n and $\tilde{\psi}_n$ are bi-orthogonal, normalized eigenvectors of \mathcal{L} and $\tilde{\mathcal{L}}$.)

$$\text{Let } \phi_n = \psi_n + \epsilon \chi \quad (\text{A-3})$$

and

$$\tilde{\phi}_n = \tilde{\psi}_n + \epsilon \eta \quad (\text{A-4})$$

where χ and η are arbitrary functions satisfying the same boundary conditions as ψ_n and $\tilde{\psi}_n$. We want to show that the ratio,

$$\frac{\langle \tilde{\psi}_n, \mathcal{L} \psi_n \rangle}{\langle \tilde{\psi}_n, \psi_n \rangle} = \omega_n \quad (\text{A-5})$$

is stationary with respect to variations in $\tilde{\psi}_n$ and/or ψ_n . That is,

$$\frac{\partial}{\partial \epsilon} \left\{ \frac{\langle \phi_n, \tilde{\mathcal{L}} \tilde{\phi}_n \rangle}{\langle \phi_n, \tilde{\phi}_n \rangle} \right\} \Bigg|_{\epsilon=0} = 0 \quad (\text{A-6})$$

We have,

$$\tilde{\mathcal{L}} \tilde{\phi}_n = \omega_n^* \tilde{\psi}_n + \epsilon \tilde{\mathcal{L}} \eta \quad .$$

Thus,

$$\langle \phi_n, \tilde{\mathcal{L}}\tilde{\phi}_n \rangle = \omega_n^* + \varepsilon \{ \langle \chi, \tilde{\mathcal{L}}\tilde{\psi}_n \rangle + \langle \psi_n, \mathcal{L}\eta \rangle \} + \varepsilon^2 \langle \chi, \tilde{\mathcal{L}}\eta \rangle . \quad (\text{A-7})$$

Similarly,

$$\langle \phi_n, \tilde{\phi}_n \rangle = 1 + \varepsilon \{ \langle \psi_n, \eta \rangle + \langle \tilde{\psi}_n, \chi \rangle \} + \varepsilon^2 \langle \eta, \chi \rangle . \quad (\text{A-8})$$

It is known, *a priori*, that the terms, quadratic in ε , will not survive the derivative operation, and they will now be dropped.

$$\frac{\partial}{\partial \varepsilon} \left\{ \frac{\langle \phi_n, \tilde{\mathcal{L}}\tilde{\phi}_n \rangle}{\langle \phi_n, \tilde{\phi}_n \rangle} \right\} = \frac{\partial}{\partial \varepsilon} \frac{\omega_n^* + \varepsilon \{ \langle \chi, \tilde{\mathcal{L}}\tilde{\psi}_n \rangle + \langle \psi_n, \mathcal{L}\eta \rangle \}}{1 + \varepsilon \{ \langle \psi_n, \eta \rangle + \langle \chi, \tilde{\psi}_n \rangle \}} . \quad (\text{A-9})$$

Using the relation,

$$\langle \psi_n, \mathcal{L}\eta \rangle - \langle \mathcal{L}\psi_n, \eta \rangle = 0 ,$$

(η satisfies boundary conditions, adjoint to those satisfied by $\tilde{\psi}_n$.)

$$\begin{aligned} \langle \chi, \tilde{\mathcal{L}}\tilde{\psi}_n \rangle + \langle \psi_n, \mathcal{L}\eta \rangle &= \langle \chi, \tilde{\mathcal{L}}\tilde{\psi}_n \rangle + \langle \mathcal{L}\psi_n, \eta \rangle \\ &= \omega_n^* \{ \langle \chi, \tilde{\psi}_n \rangle + \langle \psi_n, \eta \rangle \} . \end{aligned} \quad (\text{A-10})$$

Eq. (A-9) becomes:

$$\frac{\partial}{\partial \varepsilon} \omega_n^* \frac{\{1 + \varepsilon(\langle \chi, \tilde{\psi}_n \rangle + \langle \psi_n, \eta \rangle)\}}{\{1 + \varepsilon(\langle \psi_n, \eta \rangle + \langle \chi, \tilde{\psi}_n \rangle)\}} = \frac{\partial \omega_n^*}{\partial \varepsilon} = 0 . \quad (\text{A-11})$$

APPENDIX B

EIGENVALUES OF THE ADJOINT OPERATOR

$$\text{If} \quad (\mathcal{L} - \sigma_n)\psi_n = 0 \quad (\text{B-1})$$

$$\text{and} \quad (\tilde{\mathcal{L}} - \omega)\tilde{\psi}_n = 0, \quad (\text{B-2})$$

how is ω related to σ_n ?

Right dot multiply Eq. (B-1) by $\tilde{\psi}_n$, left dot multiply Eq. (B-2) by ψ_n , and subtract Eq. (B-2) from Eq. (B-1).

$$\langle \mathcal{L}\psi_n, \tilde{\psi}_n \rangle - \sigma_n^* \langle \psi_n, \tilde{\psi}_n \rangle - \langle \psi_n, \tilde{\mathcal{L}}\tilde{\psi}_n \rangle + \omega \langle \psi_n, \tilde{\psi}_n \rangle = 0.$$

$$\text{But} \quad \langle \mathcal{L}\psi, \tilde{\psi} \rangle - \langle \psi, \tilde{\mathcal{L}}\tilde{\psi} \rangle = 0$$

from the definition of \mathcal{L} . $\tilde{\psi}$ satisfies boundary conditions adjoint to those satisfied by ψ .

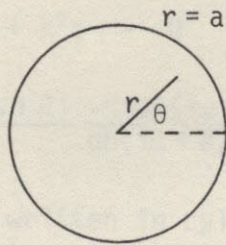
$$\text{Therefore,} \quad \sigma_n^* \langle \psi, \tilde{\psi} \rangle = \omega \langle \psi, \tilde{\psi} \rangle,$$

$$\text{or} \quad \omega = \sigma_n^*.$$

Hence, the eigenvalues of $\tilde{\mathcal{L}}$ are complex conjugates of the eigenvalues of \mathcal{L} .

APPENDIX C

CIRCULAR BASIN OF CONSTANT DEPTH WITH FRICTION



The equations of motion in rectangular coordinates for oscillatory motion are:

$$i\omega u - fv + uR = -g\zeta_x \quad (C-1)$$

$$i\omega v + fu + vR = -g\zeta_y \quad (C-2)$$

$$u_x + v_y = -\frac{i\omega\zeta}{h} \quad (C-3)$$

Then,
$$i\omega u_x - fv_x + u_x R = -g\zeta_{xx}$$

and,
$$i\omega v_y + fu_y + v_y R = -g\zeta_{yy}$$

Adding and substituting from Eq. (C-3),

$$\zeta\omega^2 + f(u_y - v_x)h - i\omega R\zeta = -gh\nabla^2\zeta \quad (C-4)$$

Derive the vorticity equation:

$$i\omega u_y - fv_y + u_y R = -g\zeta_{xy}$$

$$i\omega v_x + fu_x + v_x R = -g\zeta_{xy}$$

Subtracting and substituting from Eq. (C-3),

$$f(u_y - v_x) = -\frac{\omega f^2 \zeta}{h(i\omega + R)} \quad (C-5)$$

Substitute Eq. (C-5) into Eq. (C-4)

$$\nabla^2 \zeta + K^2 \zeta = 0 \quad (C-6)$$

where
$$K^2 = \frac{\omega^2(i\omega + R) - i\omega R(i\omega + R) - i\omega f^2}{gh(i\omega + R)}$$

Eq.'s (C-1) and (C-2) can be written in cylindrical coordinates:

$$i\omega V_r - fV_\theta + RV_r = -g \frac{\partial \zeta}{\partial r} \quad (C-7)$$

$$i\omega V_\theta + fV_r + RV_\theta = -\frac{g}{r} \frac{\partial \zeta}{\partial \theta} \quad (C-8)$$

Find the boundary condition on ζ for a solid boundary at $r=a$. Eliminating V_θ from (C-7) and (C-8):

$$V_r = \frac{1}{f^2 + (i\omega + R)^2} \left[-g(i\omega + R) \frac{\partial \zeta}{\partial r} - \frac{fg}{r} \frac{\partial \zeta}{\partial \theta} \right]$$

Since $V_r = 0$ @ $r=a$,

$$(i\omega + R) \frac{\partial \zeta}{\partial r} = -\frac{f}{r} \frac{\partial \zeta}{\partial \theta} \quad (C-9)$$

Since

$$\zeta = A J_n(Kr) e^{in\theta} e^{i\omega t} \quad (C-10)$$

is a solution to Eq. (C-6), the boundary condition becomes:

$$i\omega + R = -\frac{inf}{Ka} \frac{J_n(Ka)}{J'_n(Ka)}$$

or

$$\omega = iR - \frac{nf}{Ka} \frac{J_n(Ka)}{J'_n(Ka)} \quad (C-11)$$

BIBLIOGRAPHY

- Cartwright, D.E., 1968. "A Unified Analysis of Tides and Surges Round North and East Britain." Phil. Trans. Roy. Soc. London, Ser. A, 263, 1-55.
- Courant, R. and D. Hilbert, 1962. Methods of Mathematical Physics, Vol. II. John Wiley and Sons, p. 453.
- Ekman, V.W., 1928. "Eddy Viscosity and Skin Friction in the Dynamics of Winds and Ocean Currents." Mem. Roy. Soc., 2, No. 20 (London).
- Garrett, C.J.R. and D. Greenberg, 1977. "Predicting Changes in the Tidal Regime: The Open Boundary Problem." J. Phys. Ocean., 7, 171-181.
- Hansen, Walter, 1956. "Theorie zur Errichtung des Wasserstandes und der Stromungen in Raandmeeren nebst Anwendungen." Tellus, 8, 287-300.
- Imasato, Norihisa and Yukio Oonishi, 1975. "Study on the Currents in Lake Biwa." J. of Ocean. Soc. of Japan, 31, 53-60.
- Jackson, W.D., 1962. Classical Electrodynamics. Wiley, 641 p.
- Lamb, Horace, 1932. Hydrodynamics. Dover Publications, 738 p.
- Lauwerier, H., 1960. "The North Sea Problem. IV. Free Oscillations of a Rotating Rectangular Sea." K. Akad. Wes. Proc. A., 63, 339-354.
- Leendertse, J.J., 1967. "Aspects of a Computational Model for Long-Period Water-Wave Computation." Memo RM-5294-PR, The Rand Corporation, Santa Monica, Calif., 165 p.
- Miles, J.W., 1971. "Resonant Response of Harbours: An Equivalent Circuit Analysis." J. Fluid Mech., 46, 241-265.

- Morse, P.M. and H. Feshbach, 1953. Methods of Theoretical Physics. McGraw-Hill, 1939 p.
- Pekeris, C.L. and Y. Accad, 1969. "The K2 Tide in Oceans Bounded by Meridians and Parallels." Proc. Roy. Soc. London, A, 278, 110-128.
- Platzman, G.W., 1958. "A Numerical Computation of the Surge of 26 June, 1954, on Lake Michigan." Geophysica, 6, 407-438.
- Platzman, G.W. and D.B. Rao, 1965. "The Free Oscillations of Lake Erie." Studies on Oceanography, University of Tokyo Press, 359-382.
- Platzman, G.W., 1972. "Two Dimensional Free Oscillations in Natural Basins." J. Phys. Ocean., 2, 117-138.
- Rao, D.B., 1966. "Free Gravitational Oscillations in Rotating Rectangular Basins." J. Fluid Mech., 25, 523-555.
- Sielecki, A., 1968. "An Energy-Conserving Difference Scheme for the Storm Surge Equations." Mon. Wea. Rev., 96, 150-156.
- Snyder, R.L., M. Sidjabat, and J. Filloux, 1979. "A Study of Tides, Setup, and Bottom Friction in a Shallow Semi-Enclosed Basin: Part II." J. Phys. Ocean., 9, 170-188.
- Steen, R.G., 1972. "Calculation of Normal Modes of Oscillation in Rotating Basins Using Inverse Iteration." M.S. Thesis, Univ. of Chicago.
- Welander, P., 1961. "Numerical Prediction of Storm Surges." Advances in Geophysics, 8, 315-379.